BEARING WORLD

www.bearingworld.org

Journal

Volume 7_2022

Editors: G. Poll _ B. Pinnekamp _ C. Kunze

FVA sharing drive innovation

VDMA Verlag

Imprint

Bearing World Journal
Volume 7, December 2022

Published by:
Forschungsvereinigung Antriebstechnik e.V. (FVA)
Lyoner Straße 18
60528 Frankfurt am Main
Germany
www.fva-net.de

Online-ISSN 2566-4794

Volume 7_2022

Dear reader,

Globalization increasingly requires more and more international networking between research and development engineers. In response to this, the German Research Association for Drive Technology (FVA) launched the first Bearing World conference in 2016. With that inaugural meeting, the FVA initiated a very fruitful international dialogue in which researchers and developers from universities and bearing manufacturers came together with users and experts from the industry.

The Bearing World Journal, which is published annually, serves to foster exchange between international experts during non-conference years by featuring peer-reviewed, high-quality scientific papers on rolling element bearings as well as plain bearings. As an international expert platform for publishing cutting-edge research findings, the journal intends to contribute to technological progress in the field of bearings.

We are now starting to prepare the 2024 edition of Bearing World Journal and are looking forward to new contributions from the scientific and industrial communities. We would like to thank all authors for their fascinating contributions to Bearing World Journal No. 8.

_ **Prof. Dr.-Ing. Gerhard Poll,** Initiator, Head of international Scientific Board
_ **Dr.-Ing. Burkhard Pinnekamp,** President of the FVA Management Board
_ **Christian Kunze,** Editor-in-chief

Please send the paper you intend to publish in the next issue of the Bearing World Journal via e-mail as Word document to FVA (**submission@bearingworld.org**).
In addition please attach a PDF document.

Bearing World Scientific Board

Contents

Assessment of the Wear Behavior of Journal Bearings within a Planetary Gear Stage of a Wind Turbine Transmission

Dr.-Ing. Dirk Jaitner[1], M.Sc. Benjamin Schmelzle[2], Dr.-Ing. Rainer Fiereder[3]

[1] *AST, AVL Deutschland GmbH, Dirk.Jaitner@avl.com*
[2] *AST, AVL Deutschland GmbH, Benjamin.Schmelzle@avl.com*
[3] *AST, AVL Deutschland GmbH, Rainer.Fiereder@avl.com*

Abstract– Hydrodynamic journal bearings are a key component in heavy duty transmissions, which can be found in wind turbines and geared aircraft turbofans. In these applications journal bearings are exposed to harsh load conditions characterized by high loads and small sliding speeds e.g., during startup or emergency stop, which leads to an increased proportion of operations in mixed and boundary lubricated conditions. The numerical evaluation of their reliability, durability and economy, but also their friction power loss and wear are of high importance. In this work a method for the prediction of wear in such applications is presented. For this, an FE-based 3D multibody simulation is carried out considering all relevant effects of the bearings and the gearing as well as the components flexibility including their nonlinear interactions. The journal bearings are represented with a detailed elasto-hydrodynamic (EHD) bearing model, which considers temperature and pressure dependent fluid properties, cavitation caused by partial filling of the lubricated bearing gap, transient energy transport due to conduction and convection, thermal expansion, structural deformation, and hydrodynamic as well as asperity friction caused by the direct contact of the bearing structures. From wear simulation of different operating points, a worn in profile is calculated iteratively also considering the current state of surface roughness. During each wear simulation iteration, the wear profile is superposed to the initial bearing contour and the three-dimensional multibody simulation is re-peatedly conducted till a steady state or maximum wear depth is reached. This numerical framework calculates wear under realistic working conditions based on simulation data that is iteratively calculated. The presented method is applied to a planet gear bearing in a planetary gear stage of a wind turbine gearbox.

Keywords – Windturbine, Modelling and Simulation Technology, Wear Analysis, Hydrodynamic journal bearing

1. Introduction

Hydrodynamic journal bearings are a key component in wind turbine planetary transmissions often used for the planet gear bearings. The wind turbine transmission connects the rotor and generator of a wind turbine driveline to reduce the generators high design demands which are present in the design of direct drives. These fundamental designs and their pros and cons are discussed in [1]. One major drawback of geared wind turbine transmissions is that the transmission is responsible for up to 20 percent of the wind turbine downtime [2, 3]. The main reason for this is wear related damage of the bearings caused by fundamental problems in the tribological system and its design [4, 5]. This is due to undesired wear related damages of the bearings caused by fundamental problems in the tribological system and its design [4, 5]. Until the downtime occurs, undesired high wear continuously damages the bearing which reduces the overall performance of the wind turbine and increases the economic losses. This is not always the case because desired running in wear effects in controlled ranges can improve the initial manufactured bearing contour and reduce the maximum pressures in the bearings [4]. Furthermore, the trend towards power density increases and lightweight design leads to higher specific loads at for this application typically low sliding speeds. This leads to an increase in bearing friction with higher asperity contact share and wear. The material removal due to wear directly changes the shape and surface roughness of the bearing and influences its performance and lifetime. Wear is a complex mechanism which must be understood fundamentally to be able to predict the location of its occurrence and continuous progress.

Therefore, it is necessary to investigate and analyze the design concept of a bearing in detail regarding its influence on the initiation and progress of wear. This can be done with a dynamic multibody simulation (MBS) with flexible structures, the gear contacts and the planet gear journal bearings represented by detailed elasto-hydrodynamic (EHD) bearing model. This slider bearing model must consider temperature and pressure dependent fluid properties, cavitation caused by partial filling of the lubricated bearing gap, transient energy transport due to conduction and convection, thermal expansion, structural deformation and hydrodynamic as well as asperity friction caused by the direct contact of the bearing structures.

For a comprehensive wear simulation at different operating points the shape of the worn in profile has to be updated as well as the current state of surface roughness iteratively. During each wear simulation iteration, the wear profile is superposed to the initial bearing contour and the three-dimensional multibody simulation must repeatedly be conducted till a steady state or maximum wear depth is reached. The numerical framework presented in this paper calculates friction and wear under realistic working conditions based on iteratively calculated simulation data. The presented

method is applied to a planet gear bearing in a planetary gear stage of a wind turbine gearbox.

2. Theory of EHD Bearing Simulation Model

The gear stage of a wind turbine transmission and the wear behavior of its radial slider bearings are simulated in the present paper with the software AVL EXCITE™ [6]. In this simulation tool the real gear stage is investigated in a detailed multibody simulation (MBS) model with flexible bodies [7], which consist of condensed three-dimensional finite element structures, the gear joints for the gears in contact [8] and EHD joints [7] for the radial slider bearings. The wear simulation methodology as described in [9], considers a local mixed-hydrodynamic friction coefficient on the hydrodynamic grid level. To predict friction and wear inside the EHD bearing, this coefficient is evaluated considering viscosity, asperity pressure and local roughness parameters.

2.1. Averaged Reynolds Equation for Rough Surfaces

To calculate the pressure in the fluid film of non-linear hydrodynamic radial slider bearing contacts the Reynolds equation must be solved. The equation is extended by the so-called flow factors according to Patir and Cheng [10] to consider the surface roughness effects on the pressure and shear flow.

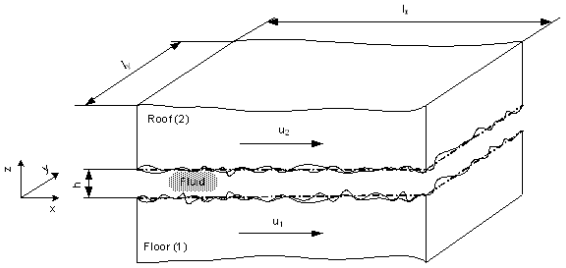

Figure 1: Lubrication Domain for Micro-Bearing Analysis

These factors can be derived from statistical surface roughness parameters or calculated for three dimensional measured rough surfaces with AVL Microslide [11]. The Reynolds equation is solved using the finite volume method considering temperature and pressure dependent fluid properties, cavitation caused by partial filling of the lubricated bearing gap, transient energy transport due to conduction and convection, thermal expansion and pressure related mechanical deformation of the surrounding structures.

$$\frac{\partial}{\partial x}\left(\phi_x^p \frac{h^3}{12\eta}\frac{\partial \bar{p}}{\partial x}\right)+\frac{\partial}{\partial y}\left(\phi_y^p \frac{h^3}{12\eta}\frac{\partial \bar{p}}{\partial y}\right) = \frac{U_1+U_2}{2}\frac{\partial \bar{h}}{\partial x} + \frac{U_1-U_2}{2}\sigma\frac{\partial \phi_x^S}{\partial x}+\frac{\partial \bar{h}}{\partial t} \qquad \textit{(Eq. 1)}$$

To predict the hydrodynamic share of the frictional losses due to viscous shear in the thin lubricant film the hydrodynamic shear stress for rough surfaces must be determined [12]

$$\tau = -\phi_x^P \frac{h}{2}\frac{\partial p}{\partial x} + \eta\frac{U_2-U_1}{h}[\phi^* - \phi_x^{S*}] \qquad \textit{(Eq. 2)}$$

2.2. Dry Contact in the Regime of Mixed Friction

In the regime of mixed friction asperity contact pressure appears locally when the roughness peaks of the surfaces get in direct contact since the fluid film cannot separate them anymore. This phenomenon occurs increasingly for harsh load conditions or small sliding speeds. According to Greenwood and Tripp [13, 14] the contact pressure is calculated as the load share of the asperities under the general assumption that the summit heights have a Gaussian distribution with the relationship [12]

$$p_c = \frac{16\sqrt{2}}{15}\pi(\zeta\beta\sigma)^2\sqrt{\frac{\sigma}{\beta}}E'AF_{5/2}(\lambda) \qquad \textit{(Eq. 3)}$$

The statistical function $F_{5/2}$ is evaluated with [12].

$$F_{5/2}(\lambda) = \begin{cases} 4.4086\cdot 10^{-5}(4-\lambda)^{6.804}, & \lambda < 4 \\ 0, & \lambda \geq 4 \end{cases} \qquad \textit{(Eq. 4)}$$

The mean asperity shear stress needs to be determined according to Coulomb's friction law to calculate the frictional losses for the asperity contact share as [12].

$$\tau_c = \mu_c \cdot p_c \qquad \textit{(Eq. 5)}$$

With the generic friction model described in [12] the friction coefficient μ_c is divided into an abrasive, an adhesive and a micro hydrodynamic term. In this model the dependency of surface roughness, the local dynamic viscosity as well as the asperity pressure on the friction coefficient is considered.

$$\mu_c = \underbrace{\mu_{abr}}_{\text{Abrasive}} + \underbrace{\mu_{adh}\cdot a^{-\sqrt{b\cdot L_N}}}_{\text{Adhesive}} + \underbrace{c\cdot r_c\cdot L_N\cdot\left[1-a^{-\sqrt{b\cdot L_N}}\right]}_{\text{Microhydrodynamic}} \qquad \textit{(Eq. 6)}$$

With the lubrication number evaluated as [12]

$$L_N = \frac{\eta|\Delta U|}{p_c L_s} \qquad \textit{(Eq. 7)}$$

2.3. Wear Model

The wear progress is simulated using Archard's model [15]. In this model, wear is only caused by asperity pressure and not by hydrodynamic pressure. Therefore, the wear load is calculated as

$$\bar{W}_L = \frac{1}{T}\int_t^{t+T} p_c\cdot\Delta U\cdot dt \qquad \textit{(Eq. 8)}$$

The probability of abrasive wear is modeled with the constant Archard Wear Factor k. It dependents on the lubricant and contact material properties. With this factor and the hardness value H the wear depth can be determined as [15].

(Eq. 9) $$h_v = \frac{k}{H}\overline{W}_L T_{acc}$$

3. Planetary Gear Stage Simulation Model

For the calculation of wear in the journal bearings of a planetary gear stage with three planet gears an MBS/EHD simulation model is set up in the software AVL EXCITE™ and can be seen in Figure 2. All bodies are modeled as flexible structures which are represented as condensed three-dimensional finite element structures. Each planet gear is supported by a radial slider bearing which is modeled as a double sided EHD contact with flexible planet gear and bearing on the pin side. For these contacts,

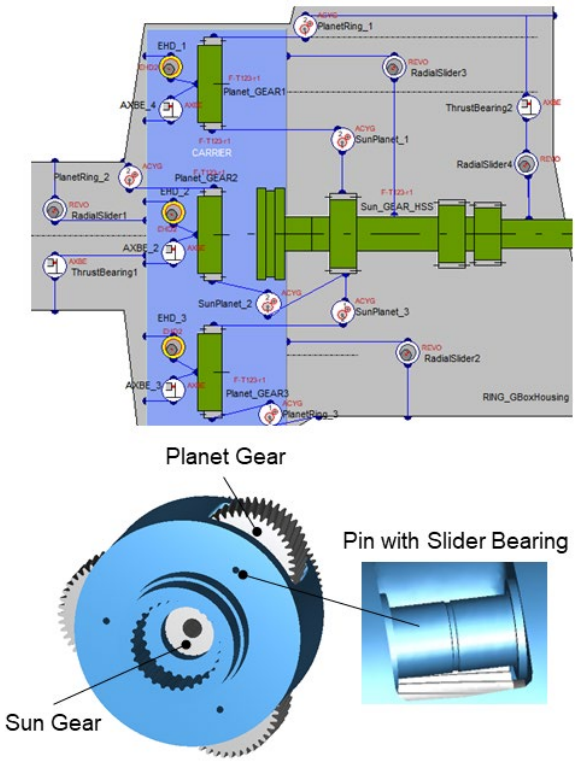

Figure 2: MBS/EHD model setup in 2D view (top) and three-dimensional model without housing and ring gear (bottom)

the progress of wear is calculated iteratively. After each iteration, a worn bearing profile is superposed to the initial bearing contour and the next wear calculation starts with the worn profile applied to the bearing surface. The gear contacts between the sun gear and the three planet gears as well as the three planet gears and the outer ring gear are modeled with the advanced cylindrical gear joint. The elasticity of the gear flanks in contact is hereby fully considered.

Table 1: Gear mesh load at tooth flanks for the nominal load.

Parameter	Sun Gear	Ring Gear
Radial Force	107.232 kN	-107.232 kN
Tangential Force	-288.913 kN	-288.913 kN
Axial Force	-40.604 kN	40.604 kN

The gear mesh loads shown in Table 1 correspond to the nominal load case at 100% relative input torque. The bearing force and moment given in Table 2 changes linearly with the input torque. For example, the mesh forces given in Table 1 result, considering the given helix angle of 8° in Table 2, in a bearing force of 577.826 kN and a bearing moment of 22.962 kNm.

The input data for the EHD bearing model of the planet gear slider bearings can be found in Table 2.

Table 2: Planet gear slider bearing, gear and lubricant parameters.

Parameter	Value
Bearing	
Nominal Bearing Diameter	220 mm
Bearing Width	370 mm
Radial Clearance	80 µm
Lube Oil Supply Pressure	0.3 MPa
Lube Oil Operating Temperature	75 °C
Nominal Rotational Speed	28.215 rpm
Nominal Bearing Load	577.826 kN
Nominal Bearing Moment	22.962 kNm
Planet Gear	
Theo. Pitch Circle Diameter	565.503 mm
Helix Angle	8°
Lubricant Properties	
Lubricant	ISO VG 32
Lubricant Kinematic Viscosity @40 °C	32 mm²/s

Table 3 contains the surface parameters used for the planet gear slider bearings for the input of the wear simulation. Sequential wear simulations are performed with different input torques by scaling the nominal input torque with 50%, 80%, 100% and 170%. For each of the load cases the wear accumulation time is 10 hours. The load cases were simulated sequentially from the lowest to the highest torque until a steady state or maximum wear depth is reached, see Figure 6.

Table 3: Bearing surface parameters for the planet gear slider bearings.

Parameter	Bearing on Pin	Planet
Summit Roughness (r.m.s)	0.3 µm	0.3 µm
Mean Summit Height	0.4 µm	0.4 µm
Young's Modulus	75000 N/mm²	210 000 N/mm²
Poisson's Ratio	0.32	0.3
Surface Roughness (r.m.s)	0.5 µm	0.5 µm
Roughness Orientation	30	30
Hardness	833 N/mm²	4800 N/mm²

In each iteration the worn bearing shell profile is calculated and superposed to the given initial manufactured bearing profile before the next iteration is performed.

4. Results and Discussion

A common measure to influence the pressure distribution and accordingly the wear behavior in radial slider bearings is applying a specific profile over the axial bearing width. In this study an initial bearing profile, referred as Base in Figure 3 and Figure 6, is investigated with the descripted methodology.

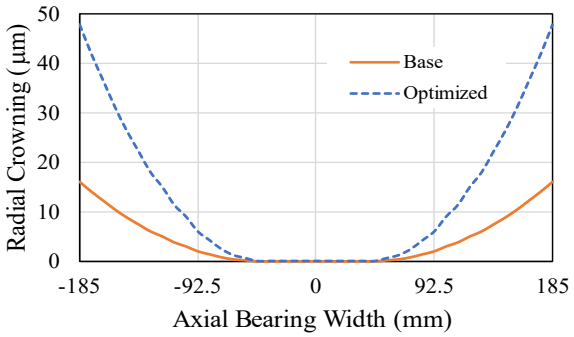

Figure 3: Bearing profile shapes

For the initial bearing profile design, the resulting accumulated wear depth after each of the different input torque load cases are presented in Figure 4. The applied load over time (10 h until 40 h) is presented in Figure 6. Because of the increase in input torque considerably more wear occurs for each load case. Therefore, the increase in wear is highest for the nominal torque (100% of nominal input torque) and the overload case (170% of nominal input torque). Since a significant amount of wear depth is already reached after the first 40 hours the simulation is stopped. The resulting pressure distributions and the worn profiles for each load case are analyzed and used to define a new profile. Herein the effect of the new profile on the meshing forces must be considered since there is a strong interaction of bearing behavior and gear contacts due to the alignment of the planet allowed by the bearing clearance. Hence, the reduction of maximum pressure, a flat distribution of pressure for the reduction of undesired wear and good contact pattern in the gear contacts are the main objectives for the optimization. In Figure 3 the resulting, optimized bearing profile shape, meeting all objectives for the investigated load cases, is shown. This bearing profile shape reduces the wear load and the resulting wear significantly, see Figure 5.

In Figure 6 the different load cases and the wear volume for both simulated bearing profile designs are illustrated over time. For the input torques of 50%, 80% and 100% of the nominal input torque the steady state is reached at the beginning of the simulation. This conclusion can be drawn since the increase in wear volume

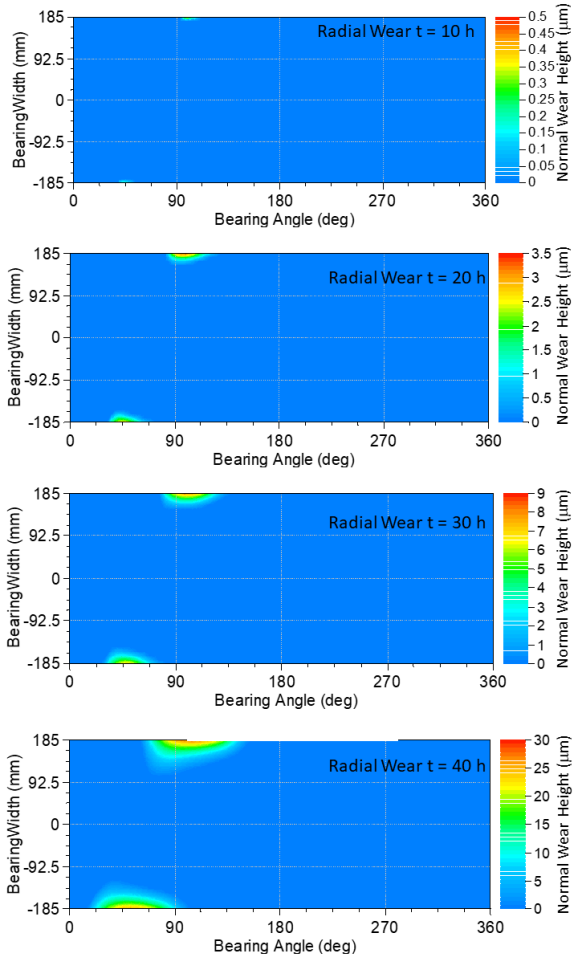

Figure 4: Slider bearing on pin wear height results for the initial bearing profile design

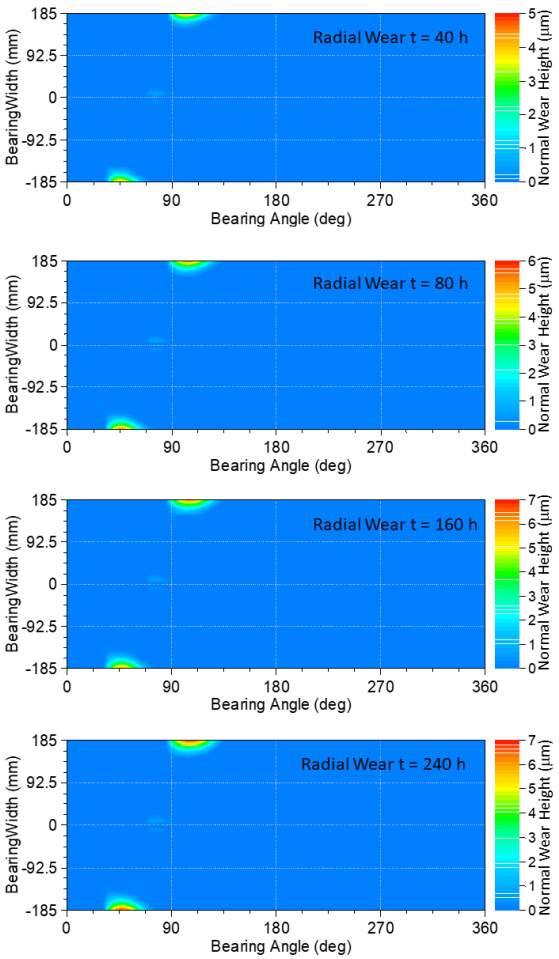

Figure 5: Slider bearing on pin wear height results for the optimized bearing profile design

is neglectable in further iterations. The scaled nominal input torque of 170% increases the wear volume and wear depth until steady state is reached for the wear depth at 240 h. Already between an accumulation time of 160 h and 240 h there is only a slight change in wear depth, see Figure 5.

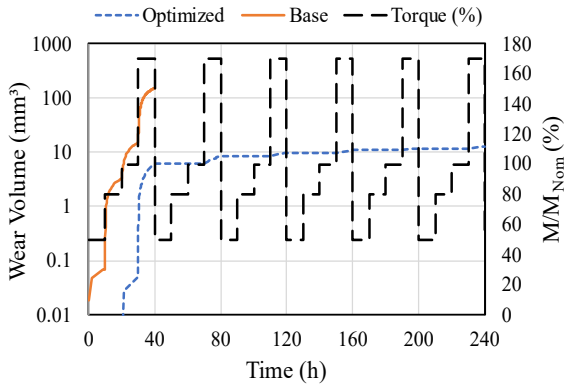

Figure 6: Slider bearing on pin wear volume and loads

The accumulated wear height for the optimized bearing design is presented in Figure 5. Comparing the resulting accumulated wear for the initial and optimized bearing profile design at the time of 40 h in Figure 4 and Figure 5, the wear height and the wear volume are significantly reduced for the optimized bearing profile shape. This can also be seen when comparing the maximum wear depth after 240 h of 7 microns for the optimized profile, see Figure 5, to the 30 microns which have been reached after only 40 h with the initial profile. The wear for the overload case (170% nominal input torque) is significantly decreased compared to the initial bearing profile design. The decrease in wear a longer bearing lifetime. Furthermore, the optimized profile shape is more robust regarding its load dependency of the resulting wear.

5. Conclusions

The method presented in this paper illustrates the investigation of the design concept of a bearing in detail. The influence of the design on the initiation and progress of wear is demonstrated for a planet gear bearing in a planetary gear stage of a wind turbine gearbox. To prevent high wear, ensure a long bearing lifetime and to minimize the downtime of the wind turbine due to bearing failure it is important to investigate the bearings wear behavior with simulation methods already during the design process. Such investigations ensure that the bearings design is optimal regarding the amount of asperity contact friction, wear load and the resulting wear. This results in a bearing that is more robust and shows a nearly load independent wear behavior.

Nomenclature

a, b, c	Constants for the friction model parametrization
A	Apparent contact area
E'	Composite Young's modulus of elasticity
$F_{5/2}$	Statistical function
h	Lubricant film thickness
h_v	Wear depth
H	Material hardness
k	Archard wear factor
L_N	Lubrication number
L_s	Reference length
M	Torque
p	Hydrodynamic pressure in contact
p_c	Asperity contact pressure
r_c	Asperity contact ratio
t, T	Time
T_{acc}	Wear accumulation time
U_1, U_2	Sliding speed of surfaces 1 and 2 in x-direction
ΔU	Difference in sliding speed of surfaces 1 and 2 in x-direction
W_l	Wear load
x	Direction along the bearing circumference
y	Direction along the bearing width
β	Asperity mean summit radius
η	Lubricant dynamic viscosity
ζ	Number of asperities per unit area of contact
τ_c	Asperity shear stress
λ	Dimensionless clearance height
μ_c	Friction coefficient
μ_{abr}	Abrasive friction coefficient
μ_{adh}	Adhesive friction coefficient
σ	Surface roughness (r.m.s.)
ϕ_i^P	Pressure flow factors in oriented direction
ϕ_i^S	Shear flow factor in oriented direction

References

[1] A. Ragheb, M. Ragheb, Wind turbine gearbox-technologies, Proceedings of the 1st International Nuclear & Renewable Energy Conference (INREC) 2010, Amman, Jordan, 21–24 March 2010, 1-8.

[2] J. Ribrant, L. Bertling, Survey of failures in wind power systems with focus on Swedish wind power plants during 1997–2005, Proceedings of the 2007 IEEE Power Engineering Society General Meeting, Tampa, FL, USA, 24–28 June 2007; pp. 1-8.

[3] P.J. Tavner, J. Xiang, F. Spinato, Reliability analysis for wind turbines, Wind Energy 2007, 10, 1-18.

[4] N. Tazi, E. Chatelet, Y. Bouzidi, Wear Analysis of Wind Turbine Bearings, International Journal of Renewable Energy Research, 2017, 7, 2120-2129.

[5] W. Qiao, D. Lu, A survey on wind turbine condition monitoring and fault diagnosis - Part I: Components and subsystems. IEEE Trans. Ind. Electron. 2015, 62, 6536–6545.

[6] AVL-List GmbH. EXCITE™ Power Unit Theory, Version R2022.1; AVL-List GmbH: Graz, Austria, 2021

[7] G. Offner, Friction power loss simulation of internal combustion engines considering mixed lubricated radial slider, axial slider and piston to liner contacts, Tribology Transactions, 2013, 56, 503–515.

[8] Z. Neusser, M. Sopouch, T. Schaffner, H. Priebsch, Multi-body Dynamics Based Gear Mesh Models for Prediction of Gear Dynamics and Transmission Error, SAE Technical Paper 2010-01-0897, 2010.

[9] S. R. Bewsher, G. Offner, An Iterative Wear Approach Dependent on Temperature, Asperity Pressure and Worn Profiles for EHD Simulation of Powertrain Components", OeTG Symposium, 2021.

[10] N. Patir, H.S. Cheng, Application of average flow model to lubrication between rough sliding surfaces, Journal of Lubrication Technology, 1979, 101, 220–229.

[11] H. Herbst, Theoretical Modeling of the Cylinder Lubrication in Internal Combustion Engines and its Influence on Piston Slap Induced Noise, Friction and Wear. Postdoctoral Thesis, TU Graz, Graz, Austria, 2008.

[12] G. Offner, O. Knaus, A Generic Friction Model for Radial Slider Bearing Simulation Considering Elastic and Plastic Deformation. Lubricants 2015, 3, 522–538.

[13] J.A. Greenwood, J. H. Tripp, The elastic contact of rough spheres, Journal of Applied Mechanics, 1967, 34 (1), pp. 153-159.

[14] J.A. Greenwood, J. H. Tripp, The contact of two nominally flat rough surfaces", Proc. IMechE, 1970-1971, 185, pp. 625-634

[15] J.F. Archard, Contact and rubbing of flat surfaces", Journal of Applied Physics, 1953, 24, 981–988.

Contact Analysis of Wind Turbine Blade Bearings by Means of Finite Element Method and Alternative Slicing Technique

Max Buescher[1], Volker Schneider[2], Ralf Schelenz[1], Georg Jacobs[1], Gerhard Poll[2]

[1] *Center for Wind Power Drives/ RWTH Aachen University/ max.buescher@cwd.rwth-aachen.de*

[2] *Institute of Machine Design and Tribology/ Leibnitz University Hannover/ schneider@imkt.uni-hannover.de*

Abstract– Load capacity design of blade bearings can be performed using high-resolution FE methods and is made much more effective by techniques such as surrogate elements or script-based modeling. The design of blade bearings is complex due to the combined effects of dynamic load cases on an asymmetrical structural elasticity in combination with irregular oscillating patterns of the individual pitch control. To consider fatigue life and hardening depth, knowledge of the local raceway stresses that may occur as a result of these complex blade bearing specific loads is necessary. The simplified design technique must therefore be extended to enable a transfer of the complex global load relationships to the local contact.

This article presents an extension of a rotor star FE model including a blade bearing that offers finely dissolved contacts for a raceway stress analysis of the most critical sectors. For this purpose, solid rolling elements are included alongside surrogate elements in the blade bearing model. Moreover, an analytical slicing technique (AST) suitable for impaired elliptical contacts accompanying the FE model is used and compared with the results. In conclusion, considering a truncation factor, the AST model shows good agreement with the extended FE model by comparing their contact pressure and pointing out characteristic deviations at the raceway edge.

Keywords – wind turbine blade bearing, four-point contact, simplified finite elements, slicing technique, truncated elliptical contact

1. Introduction

Currently, no method to estimate the service life of blade bearings, such as dynamic load ratings according to ISO 16281 [1] has been acknowledged [2]. At least, it has become established practice to design against the permissible pressure according to ISO 76 [3], [4], which requires a calculation of the raceway contacts. For the complex load situation, a FEM simulation must be performed, which includes a structural rotor star model with an integrated blade bearing to calculate the blade root loads.

Many publications show the necessity to consider the elasticity of the entire blade-hub joint structure [5]-[13]. However, it has long been assumed that the computational effort of such a comprehensive modeling approach is too high [6]. Due to the importance of a safe blade bearing design, a lot of research activity was invested, which enabled such a rotor star model including the blade bearing. Besides the increase in computational performance, the complexity of several hundred rolling element contacts can be represented by simplified surrogate elements, according to Daidé and Kania [5], [6]. With this technique, it is possible to efficiently determine the load distribution as magnitude and effective angle.

During the structural rotor star simulation, the raceway pressure can be analyzed, using further suitable models. One possibility to calculate the contact state much more efficiently than using the finite element method is the Hertzian theory [14]. However, if truncation occurs, or if the pressure distribution needs to be calculated under the influence of surface spalling, an applicable calculation variant is the Alternative Slicing Technique (AST), according to Teutsch [15] or Reusner [16]. These methods are based on a simplified half-space model [17] and were modified with the approaches presented by Houpert [18], [19].

To investigate the raceway pressure distribution at any arbitrary circumferential position, by taking the elasticity of the rotor star into account, this contribution presents an extended blade bearing FE model that combines simplified elements with solid rolling elements. The combination is achieved by iteratively adjusting the spring stiffness of the simplified elements. Thus, critically loaded raceway sectors can be evaluated directly from the FE model, but also analytically. Finally, the results of the extended rotor star FE model are compared with the AST model results.

2. Methodology

For the safe design of blade bearings, it is necessary to dimension them in advance to accommodate different load situations. To do this, FEM simulations can be used. However, these are very complex, and to make them more efficient and less computationally time-consuming, there are several approaches to simplify the complex relationships. The following sections explain the basics and models that can be used to modify a FEM model. Furthermore, the benefit of slice models in interaction with a FEM simulation is explained.

3. Contact Load Modeling

Load distributions Q_j and contact angles β_{def} of four-point contact bearings frequently used as a blade bearing are calculated via measuring the axial

ΔZ and radial ΔR displacement of the centers of curvature during a FEM simulation. Thereby, the deformation of the rolling element cutting plane in each circumferential sector is described according to equation 1.

$$\beta_{def} = tan^{-1}\left(\frac{\Delta Z}{\Delta R}\right) \qquad (Eq.\ 1)$$

For an ideal sphere, the contact forces always point to the rolling element center. Figure 1 shows that for a four-point contact geometry the centers of curvature of the raceways lie on the extension of the resulting contact lines and thus enclose the rolling element in two gothic arcs.

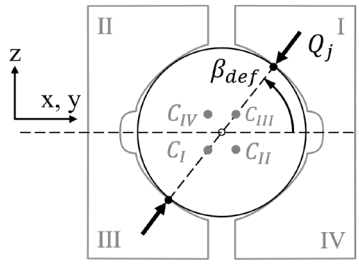

Figure 1: Four-point contact bearing geometry

Combined with the Hertzian theory, simplified surrogate elements are the state-of-the-art modeling technique to enhance the efficiency of the calculation. With surrogate elements, solid-body modeling is replaced by coupling two centers of curvature with a nonlinear compression spring.

Figure 2 shows the centers of curvature used as support points to couple opposing rigid shell elements [5]. During further development of modern FE software, distributing coupling elements (Figure 3) are available in addition to rigid shell elements which allow the simulation to be carried out more effectively and stable.

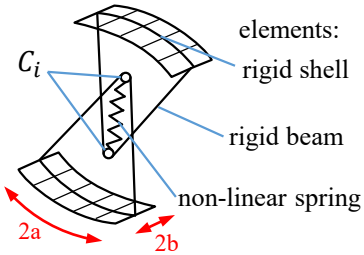

Figure 2: Rigid shell elements [13]

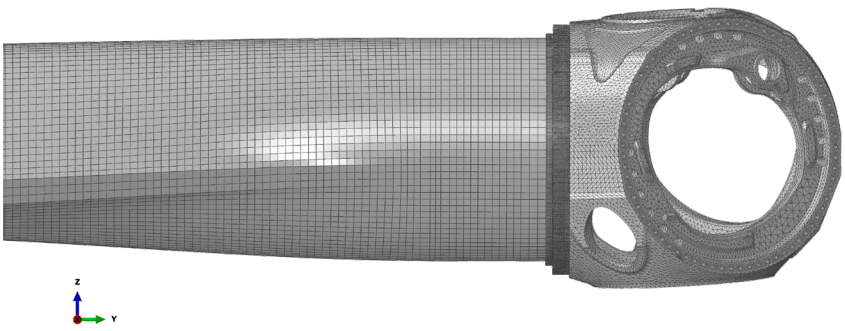

Figure 5: Graphic representation of the 1/3 rotor star FE model

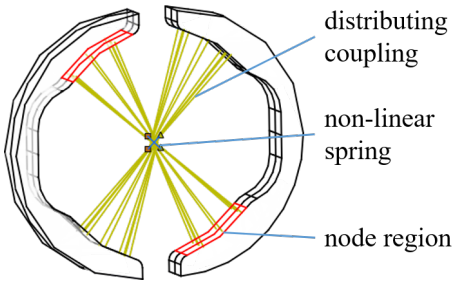

Figure 3: Distributing coupling elements

The difference between both modeling techniques is that shell elements represent a rigid indenter with just a single curvature profile against an elastic raceway contour, whereas using couplings in the FEM software different functions, such as rigid kinematic, continuum, and structural distribution can be adjusted to introduce the load from each node. However, both substitution techniques cannot adequately describe the load-dependent, nonlinear change of the contact surfaces. This fuzziness is amplified by the blade bearing-specific strongly varying contact load distribution.

Figure 4 shows the nodal force distribution of opposing raceways of a solid rolling element. In significant difference to surrogate modeling techniques, the raceway pressure distribution can be calculated considering impaired and changing contacts.

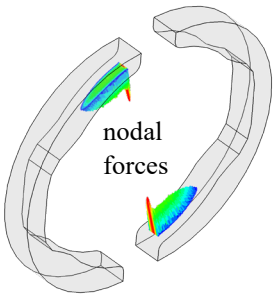

Figure 4: Nodal load distribution of a FE solid contact simulation

4. Rotor Star Finite Element Model

The presented FE model incorporates the influence of connected bodies. Figure 5 shows the one-third rotor star model, consisting of a rotor blade connected to the inner blade bearing ring with bolts through a stiffening ring.

Table 1: WT, Model information

Wind turbine	
Performance class	3 MW
Approx. blade length	60 m
Hub height	85 m
Four-point contact bearing, double rows	
FE model	
1/3 rotor star ~9 million elements	
Loads acting at blade chords	
Spring & full rolling elements	

The outer bearing ring is also connected to the hub by a bolted connection. Due to the wind loads acting on all rotor blades, the loads in the stroke are superimposed, which is considered negligible for this article. In the simulation, the loads are imposed on the rotor blade after previously calculating the wind loads using the NREL Aerodyn v.17 code.

4.1. FE Model Extension

Figure 6 shows a representation of a blade bearing with two integrated rolling elements as part of the extended rotor star FE model (*FEM 1)*. Since simplified surrogate elements are only suitable for fully supported contacts [5], but situations with truncated contact ellipses must also be investigated, rolling elements with a locally fine discretization are integrated at these critical contacts. Due to the fine contact zone mesh of the rolling elements, the total element number of the rotor star model increases from ~1 m. to ~9 m. elements for two integrated rolling elements, although a strict partitioning strategy was used to reduce the element number. By pitching the rotor blades in the dynamic wind field, the critically loaded sector (dashed lines) shifts with the composition of the wind loads and the position of the components involved in the load transfer. Therefore, a pre-simulation is required to identify the load distribution apex (critical sector).

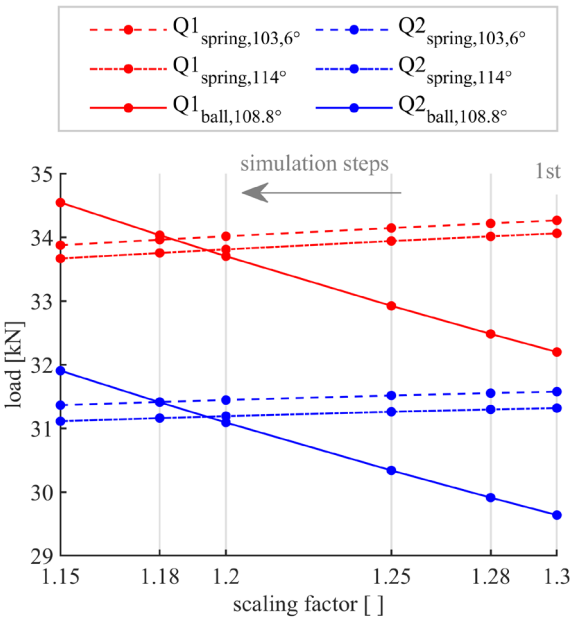

Figure 7: Adjustment of spring element stiffness to solid rolling elements

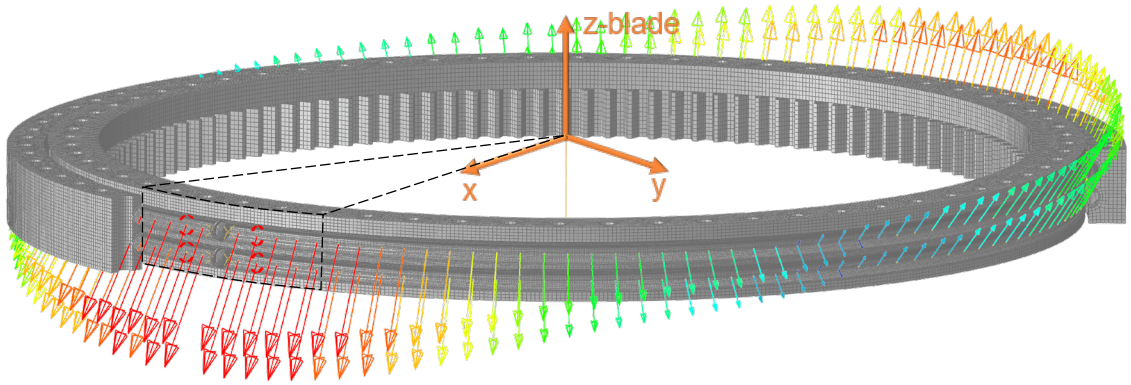

Figure 6: Step cut through the exemplarily loaded blade bearing of the FE model with integrated rolling elements (FEM 1)

4.2. Rolling Element Integration

To combine surrogate elements alongside solid rolling elements in the same FE model, an iterative stiffness adjustment of the non-linear spring elements is required. The objective of the iteration is to match the load distributions of the extended model (FEM 1) with the model that consists entirely of simplified surrogate elements (FEM 2).

Figure 7 shows that the iteration starts with scaling of an already known stiffness curve by 30%, to subsequently decrease it step wisely until the load distributions match. By lowering the stiffness of the spring elements, the load on the solid rolling elements increases disproportionately stronger. As a result of the adjustment, an approximate match of the load was achieved at an increased spring stiffness of 18 %. The unscaled reference stiffness curve next to the curve determined in this way is shown in Figure 8.

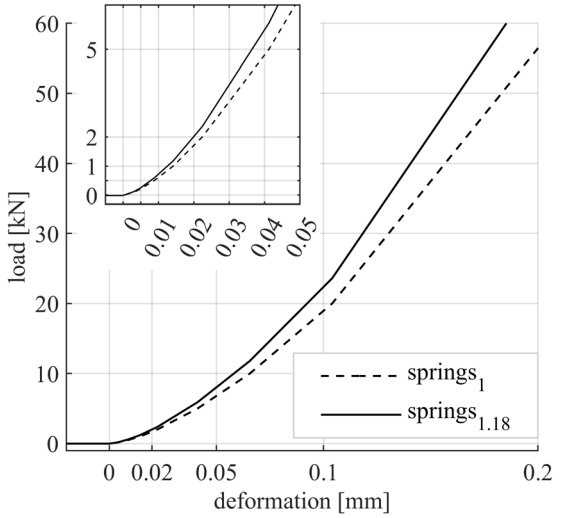

Figure 8: Used non-linear spring stiffness curve, scaling factor 1.18

For a more accurate result, the value of the determined curve is slightly lower, because the solid rolling elements at the apex of the load zone (critical sector) transfer higher loads compared to the directly neighboring elements. As long as the rolling element stiffness does not match the stiffness of these adjacent spring elements there is a mutual influence, thus using the subsequent spring elements increases the convergence.

Figure 9 shows the comparison of the load distribution between FEM 1 and FEM 2 of a load case in which the edge pressure is initially greater than the Hertzian contact pressure on the raceway. Thereby, the contact surfaces of simplified elements outside of the critical sector are subjected to lower loads and not noticeably truncated. The results yield a close agreement with a relative deviation of less than 1 % of the maximum value. The scaled stiffness of the replacement elements also shows the same agreement for other blade root loads.

The selected load case (Table 3) is a condition in which a locally limited critical sector with truncation occurs at the load zone apex. Thereby, the blade root loads correspond to the composition of the wind loads acting as forces on the chords of the airfoil. These loads have been scaled by assuming a normal wind turbulence distribution according to DIN EN 61400 [21] to produce a typical blade bearing load distribution for the analysis.

4.3. Contact State Variables

With the help of FEM simulation, it is possible to determine the load distribution in the blade bearing. Usually, a model with simplified surrogate elements (FEM 2) is used providing these values to an accompanying analytical model. This can be used to obtain the contact variables, such as the semi-axis lengths a, b, the pressure distribution p_j, and the deflection δ_j. Generally, the Hertzian theory provides good results even if not all conditions are strictly fulfilled. In case

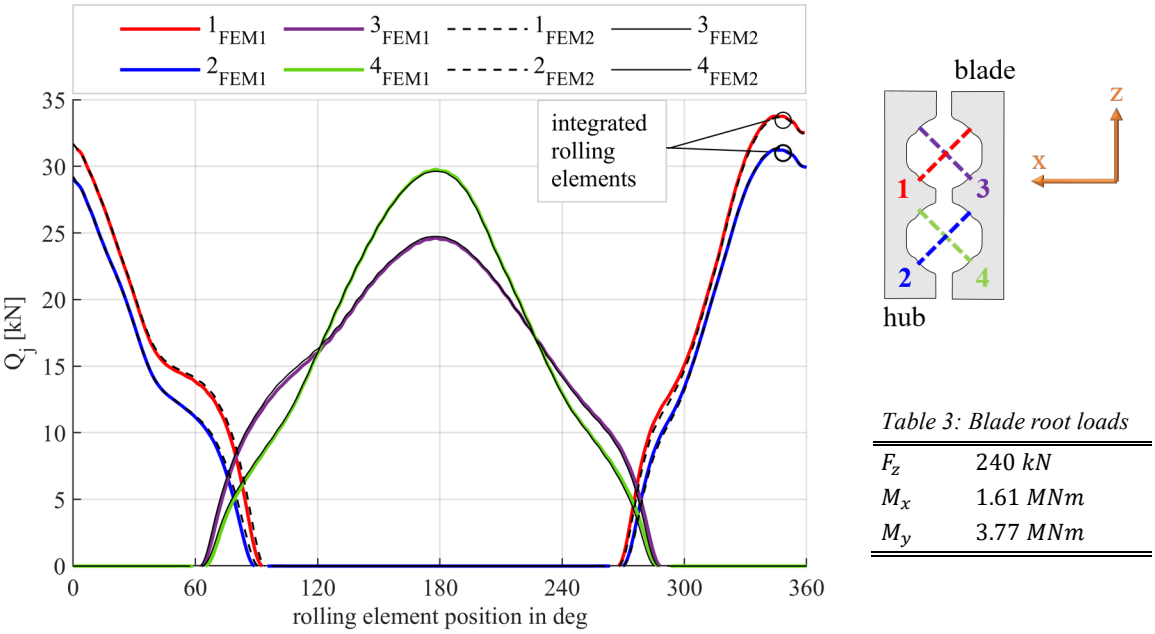

Table 3: Blade root loads

F_z	240 kN
M_x	1.61 MNm
M_y	3.77 MNm

Figure 9: Load distribution comparison
FEM1: 1/3 rotor star model with simplified elements and integrated rolling elements
FEM2: 1/3 rotor star model with simplified elements

No preload and no clearance were assumed in the bearing modeling. These values would affect the results significantly. The corresponding bearing specifications are given in Table 2.

Table 2: Blade bearing specifications

d_m	2.4 m	bearing diameter
d_B	45 mm	ball diameter
d_R	46.8 mm	raceway diameter
β_0	45 °	contact angle undeformed
E	210 GPa	young's modulus
ν	0.3	poisson's ratio

the elliptical contact surface is not fully developed, the results do not agree anymore, which is addressed in the following discussion.

Figure 10 shows a comparison of the contact angle variations between the inner and outer ring of the two rolling elements integrated into FEM 1 (see Figure 9, contact lines 1, 2). It shows that the contact point on the hub side performs a stronger migration. As mentioned above, the contact angle shifts depending on the centers of curvature in the rolling element cutting plane. The variation is obtained by counting the contact nodal forces and is used to provide a resulting rolling element load towards the AST model.

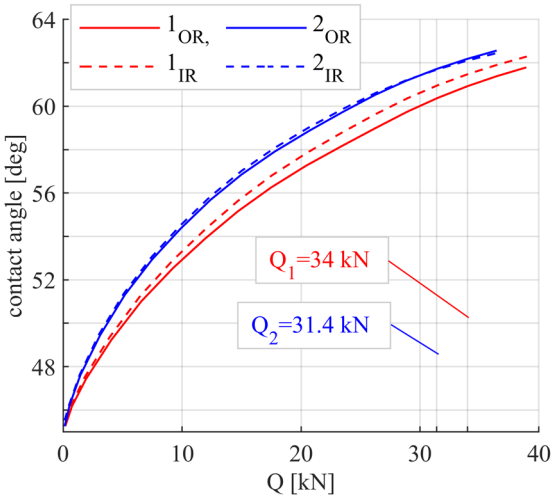

Figure 10: Contact angle variation of integrated rolling elements, FEM 1

The variation of the maximum pressure of the integrated rolling elements of FEM 1 is depicted in Figure 11. If the contact is fully supported the pressure is far below the permitted pressure of 4.2 GPa, according to ISO 76 [3]. However, truncation starts before the bend of the curve in the diagram, since with increasing contact force the pressure maximum initially remains in the center of the ellipse until it is exceeded by the pressure peak that develops at the raceway edge. Due to this behavior, it is recommended to use the combination of contact angle and calculated semi-axis length to examine truncation.

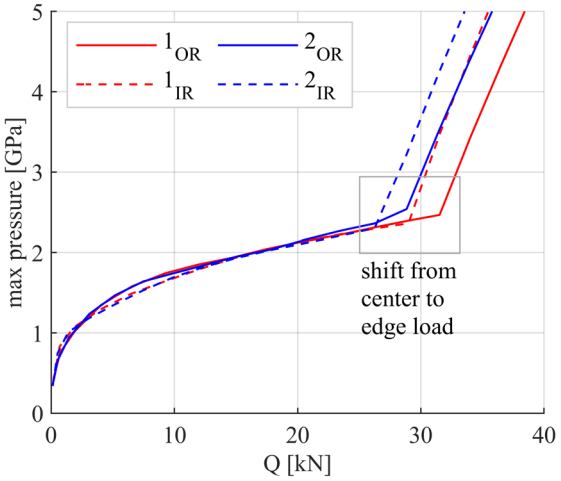

Figure 11: Maximum raceway pressure, FEM 1

Moreover, it can be seen in Figure 11 that the shift of the pressure maximum occurs at lower contact loads at the inner ring, which can be explained by a stronger migration of the contact angle. Additionally, the blade root bending moment also acts directly on the inner ring.

Although the design of large slewing bearings aims at avoiding truncation, a safe exclusion seems challenging given their comparatively high elasticity under highly fluctuating wind loads. In the blade bearing design, it is sought to adapt the key parameters of the raceway contour to avoid truncation. The interactions of the key design parameters, such as oscillation ratio, undeformed contact angle, and blade-hub joint stiffness, would require further variations of the FE models and thus exceed the scope of this article. Subsequently, the sensitivity of the osculation ratio excluding further interactions is addressed in the result section 6.6 by the AST model.

5. Slicing Technique for Point Contacts

To obtain the contact state variables a FEM simulation is not always the most efficient way and sometimes it is advisable to use time-efficient analytical methods, with which it is possible to infer the result within a few milliseconds. The pressure distribution within a Hertzian contact can be of particular interest for blade bearing point contacts. In the case of a truncated contact or spalled raceway, increased stresses can occur at the rough edges. Whether these stresses lead to an overload of the material is of particular interest. The method presented had its origin in the design of cylindrical roller bearings [15]-[17] and [20], [22], with them it is possible to calculate the load distribution alongside a line contact by dividing the roller into many narrow slices. Compared with the method from ISO 16281 the methods developed by Teutsch and Reusner additionally takes the influence of a load on adjacent surface areas into account. The presented method is based on Teutsch's approach for line contacts and is extended with the approaches of [18] and [19] to make the approach also suitable for point contacts. It should be noted that a global bearing calculation is still necessary to obtain the needed input such as contact force and contact angle first to use this method. It solely calculates one contact without the interactions between the different rolling elements, which are included in the global calculation, such as the presented numerical approach.

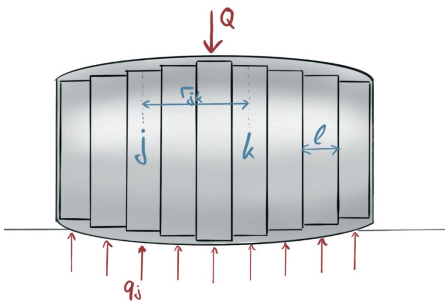

Figure 12: Geometric dependencies between the discs for the AST model

The Alternative Slicing Technique (AST) uses curve fitting factors provided by Houpert [18]. They are named *CA, CB, CD, CP* and *f2* to approximate the greater- and lesser half width a and b, the deflection δ and pressure p. The factors are solely based on the ratio of equivalent radii k

$$k = \frac{R_{y,eq}}{R_{x,eq}} \qquad \textit{(Eq. 2)}$$

Where the equivalent radii of two contacting bodies are defined as follows, while concave curvatures are defined as negative

$$\frac{1}{R_{x,eq}} = \frac{1}{r_{1x}} + \frac{1}{r_{2x}} \qquad \textit{(Eq. 3)}$$

$$\frac{1}{R_{y,eq}} = \frac{1}{r_{1y}} + \frac{1}{r_{2y}} \qquad \textit{(Eq. 4)}$$

To calculate the variables in a deflected contact the dimensionless load W needs to be determined

$$W = \frac{Q}{E' \cdot {R_{x,eq}}^2} \qquad \textit{(Eq. 5)}$$

With this it is possible to calculate the initial deflection

$$\delta = CD \cdot W^{\frac{2}{3}} \cdot R_{x,eq} \qquad \textit{(Eq. 6)}$$

To describe the influence of a load of one slice on the neighboring slices in a simplified way, a geometric dependency matrix is used, which was extended with the approach from [18] to make Teutsch's approach dimensionless. Regarding to the dependencies are described as follows

$$w_{j,k} = \left(\frac{1}{r_{j,k}}\right) \quad when \quad j \neq k \qquad \textit{(Eq. 7)}$$

$$r_{j,k} = abs(k - j) \qquad \textit{(Eq. 8)}$$

$$w_{j,k} = 4 \quad when \quad j = k \qquad \textit{(Eq. 9)}$$

Next, it is necessary to establish the load-deflection dependency s related to the length of one slice.

$$s = \frac{2}{\pi \cdot E'} \cdot \frac{CD}{CP \cdot CB \cdot l_{slice}} \qquad \textit{(Eq. 10)}$$

With matrix w and the number of slices that are in contact n_{eff}, it is possible to calculate the weighted yielding matrix S_w for the inner and outer ring contact.

$$S_w = \frac{n_{eff}}{\sum w_{j,k}} \begin{bmatrix} w_{1,1} & \cdots & w_{1,n} \\ \vdots & \ddots & \vdots \\ w_{n,1} & \cdots & w_{n,n} \end{bmatrix} \qquad \textit{(Eq. 11)}$$

Next the geometrical interference Δ along the roller race contact at each point along the y-axis can be calculated as a function of deflection δ and the distance between the raceway and the rolling element. According to Houpert this results to

$$\Delta_i = \delta - \frac{{y_i}^2}{2 \cdot R_{y,eq}} \qquad \textit{(Eq. 12)}$$

To calculate the individual force of each slice *i* the following equation is established.

$$\{q_i\} = \frac{Coef}{s} \cdot \left[{S_{w,i,j}}^{-1}\right] \cdot \{\Delta_j\} \qquad \textit{(Eq. 13)}$$

The condition must be fulfilled that the sum of the individual forces of each slice corresponds to the total force. This forms the equilibrium, in which the deflection δ must be adjusted iteratively. In his research, Houpert found that the influence of truncated contacts resulted in slight differences compared to his reference calculations. He therefore introduced a correction factor *Coef*. This is dependent on the curvefit-factor f2 (found in [19]) and a geometric value D.

$$Coef = max(1, T^{0,18})$$
$$T = f_2 \cdot \sqrt{D} = f_2 \cdot (\delta_0 \cdot R_{x,eq})/L^2 \qquad \textit{(Eq. 14)}$$

While δ_0 being the contact deformation at the ellipse center and L the effective contact length.

$$0 = \sum q_i - Q \qquad \textit{(Eq. 15)}$$

According to Houpert [19] the resulting pressure at each calculated slice is calculated as follows

$$p = E' \cdot \sqrt{\frac{q_i}{2\pi \cdot E' \cdot R_{x.eq} \cdot l_{slice}}} \qquad \textit{(Eq. 16)}$$

In his research, Houpert also identified differences between the numerically determined pressure peaks at the edges using the CST tool from Timken company and those using the modified AST method. To include this difference in the calculation of the truncated contacts, the load q_i on the first as well as the last loaded slice must be multiplied by 1.25. The obtained results from this method are presented and compared to the FEM method in the next section.

6. Results

The contribution is based on several simulations of a blade bearing in a rotor-hub joint, which initially aims to enable the integration of rolling elements for the local contact stress analysis. For the comparison, an analytical model for point contacts suitable for large slewing bearings was taken up from the literature, which also can analyze impaired contact surfaces. With further simulations, the quality of each model is evaluated by refining the approximation.

The comparisons between FE and AST methods exemplify the magnification of the truncated contact ellipse in section 6.1 and the pressure distribution in section 6.2 of the previously selected critical load case in Table 2. The magnification evaluation is performed for the raceways on the blade row where the highest pressures occur. Since the AST model starts with the approximation of the contact profile into discrete slices, this information must be obtained from the FE model and is described by the degree of truncation, shown in Figure 13 below. Subsequently, the AST model can be adapted to the condition of the FE model

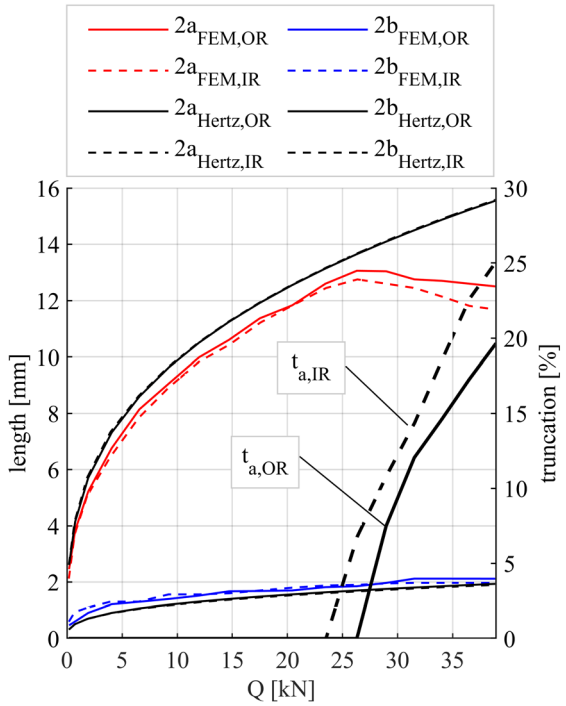

Figure 13: Contact ellipse semi-axis length and truncation FEM 1, blade row 1

by using the information on the rolling element load and the contact angle.

The results of both models can be compared in joint graphs but must be understood in terms of their chosen resolutions. Therefore, in section 6.3 the net density of the FE model and separately in section 6.4 the AST model discretization is described. Since both methods use different techniques to approximate the contact profile, no direct comparison is presented.

Finally, two investigation capabilities with the AST model are exemplarily presented, to show the effects of impaired contacts.

6.1. Truncation factor

In this article, the truncated length is expressed as a proportion of the major semi-axis in the radial direction, described in equation 17.

$$t_{Prof} = \frac{2a_{Hertz} - 2a_{FEM}}{2a_{Hertz}} \qquad \textit{(Eq. 17)}$$

The Hertzian Contact theory represents an ideal case whose conditions are not fully met by the blade bearing geometry. As a consequence, in Figure 13 the Hertzian semi-axis length is generally slightly higher than the semi-axis calculated via FEM 1, causing a deviation of the presented truncation factor.

To identify truncation no contact simulation of the raceways is needed. It is most common to check whether the contact ellipse exceeds the raceway by a simple comparison of the semi-axis length with the raceway width, considering the contact angle, which can also be determined with a surrogate element model such as FEM 2. However, due to the slightly larger Hertzian contact ellipse, this method is more conservative than a FE simulation.

6.2. Pressure Distribution

In the FE model, a surface smoothing filter was deliberately not applied to achieve the most unaltered results possible. For comparison, however, the result points are then represented by a curve fit. As Figure 14 depicts, a close agreement with the FE results is obtained in the comparison of the unimpaired left major semi-axis.

To correspond to the pressure distribution of the slicing model in the comparison, the evaluation of the FE contact pressure distribution was terminated when the maximum value was reached, which results in an immediate pressure drop instead of a sloping curve. Besides consistent differences between the in-

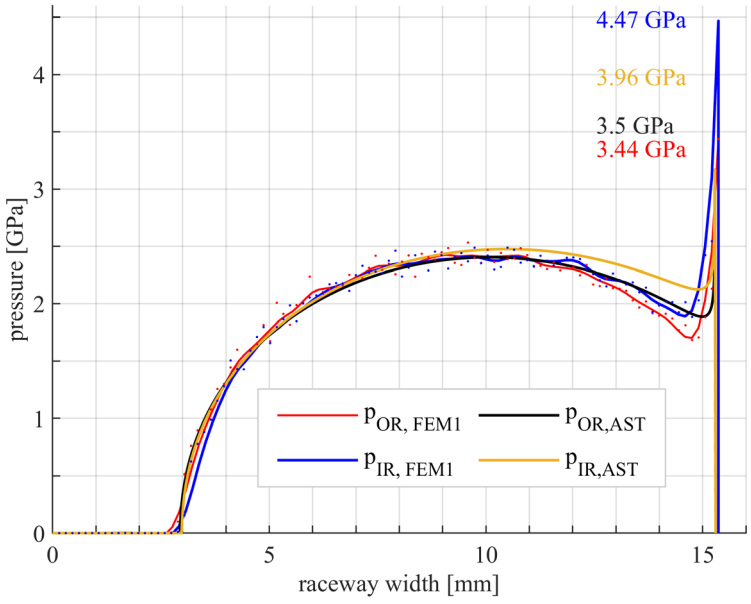

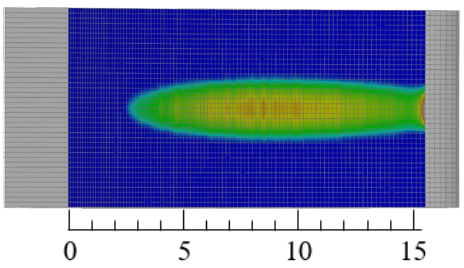

Figure 15: Pressure ellipse, outer ring, blade row t_{prof}=14.6 % Q=34 kN β_{def}=61 deg

Figure 14: Raceway pressure distributions, FEM 1 versus AST, blade row, 1

ner and outer raceways and similar model-specific behavior of the truncated major semi-axis, deviations in the pressure distributions can also be observed at the raceway edge.

The position of the edge pressure peak (~15.36 mm) calculated by the AST model is reasonably close to the FE pressure peak, given by the load-deformation relation of the contact load and angle and the truncation factor. However, the pressure peaks of the FE results are slightly displaced since the pressure peak becomes maximum just behind the edge towards the radius.

The pressure peak also increases earlier in the FE model, which is probably related to a locally larger deformation of the edge zone in the FE model.

Just before the pressure peak occurs in the FE model, the pressure curve drops locally more than in the AST model. One explanation is a stronger effect of the weighted yielding matrix in the AST model on neighboring slices.

At the inner ring, the pressure exceeds the theoretical linear-elastic behavior. The corresponding mesh study shows that the stress peaks only grow weakly with a further increase in the mesh density. As a result, the stress peaks finally converge to higher values.

As explained in section 5, the scaling of the first and last slice according to Houpert improves the results of the pressure peak given by the AST towards the FEM results. Nevertheless, this comparison was intended to show that an approximate estimation of pressure spikes is possible with analytical methods in order to be able to act significantly more time-efficiently. It could be shown that the AST method is able to calculate critical states with sufficient accuracy. With this information, the blade bearing modelling can be adapted without having to rely on computationally intensive methods.

6.3. FEM Net Density

Figure 16 shows mesh study curves of the raceway edge including the values at the radius. The investigation was carried out on the blade-side outer ring. In the process, the element volume was reduced to a lower percentage of the local element volume that was used in FEM 1 to approximate the contact zone. For the fully formed semi-axis, the pressure distributions of both models are almost identical. The results cannot be improved by further mesh refinement.

On the part of the truncated semi-axis, mesh refinement leads to an increasing but converging pressure peak. However, the peak converges slightly above the limit to plasticization.

It can be assumed that for values near the plasticization zone, local deformations tend to form, which then lower the peak. However, this is outside of the material behavior that is assumed for the FE model.

Since convergence can be achieved at the edge, it is reasonable to also specify a value that scales the load peak as a function of the mesh density, because this would allow computing time to be saved without loss of quality.

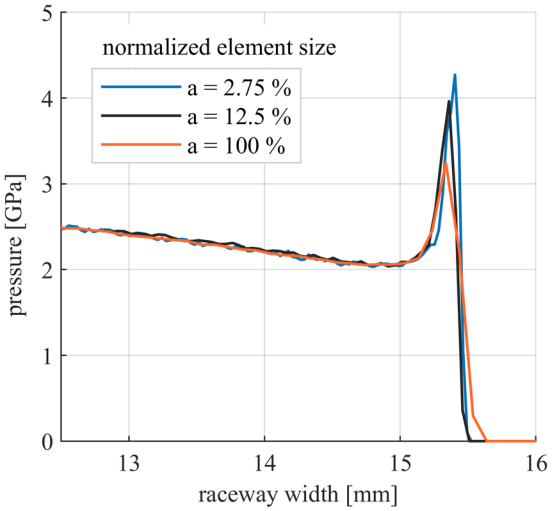

Figure 17: Edge mesh study, FEM 1, blade row, 1

6.4. AST Discretization

Similar to the FEM net density the pressure spike on the truncated contact can be approximated more precisely the finer the discretization is chosen. If the discretization of the slice length is too coarse, it is possible that the point of the highest pressure may be missed. On the contrary, a high discretization serves to represent the pressure as well as possible, but at the cost of computing time.

Compared to bearings such as those used in gearboxes, a high level of discretization is particularly important for the long contacts in blade bearings. Figure 17 shows the maximum pressure of the truncated edge about the slice discretization and plotted against the calculation time. Since the calculation time is highly dependent on the system used, it should only be perceived as a relative change in calculation time. It can be seen that the pressure increases significantly at

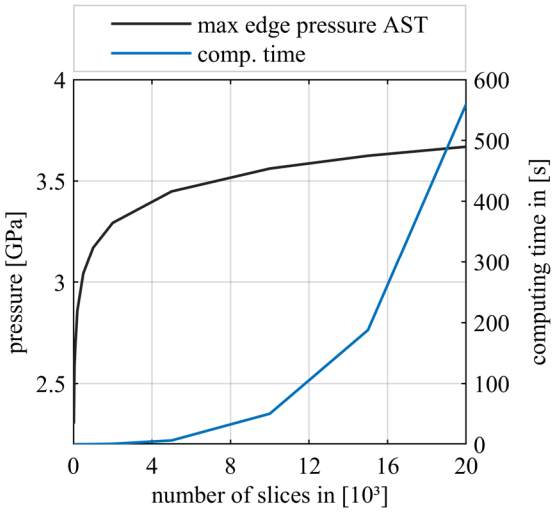

Figure 16: Effect of calculation accuracy on time and pressure convergence of AST model

first and approaches a limit value at higher discretization. In contrast, the computation time increases exponentially with increasing discretization.

In this example, a minimum of 1001 slices are reasonable to obtain proper results, which corresponds to a slice width of 0.015mm. If this slice width would be transferred to a 6008 DGBB at the same pressure, it would only correspond to a slice number of about 151. This should demonstrate that to obtain a similar quality of results, a significantly higher number of slices is required for the dimensions of a blade bearing compared to a 6008 bearing, which of course results in a longer calculation time too. Since truncation occurs only at a few contacts if at all, this method is used only rarely. A high calculation time is therefore acceptable.

6.5. Surface Spalling Edge Pressure

Another benefit is the rapid investigation of the effect of raceway damages on the pressure distribution. Figure 18 shows the difference in pressure distribution on a raceway containing a spalling and an indent compared to an undamaged raceway under the same load conditions. The influences of a raceway shortened by a breakout are visible. On the one hand, the pressure spikes at the edges of the breakout are visible and, on the other hand, there is a significant widening of the contact and an overall higher contact pressure due to the missing part of the raceway within the contact ellipse.

The method thus creates a possibility to investigate the effects of damage on the contact pressure, so that an estimation of the severity becomes possible to decide whether a further operation is permissible.

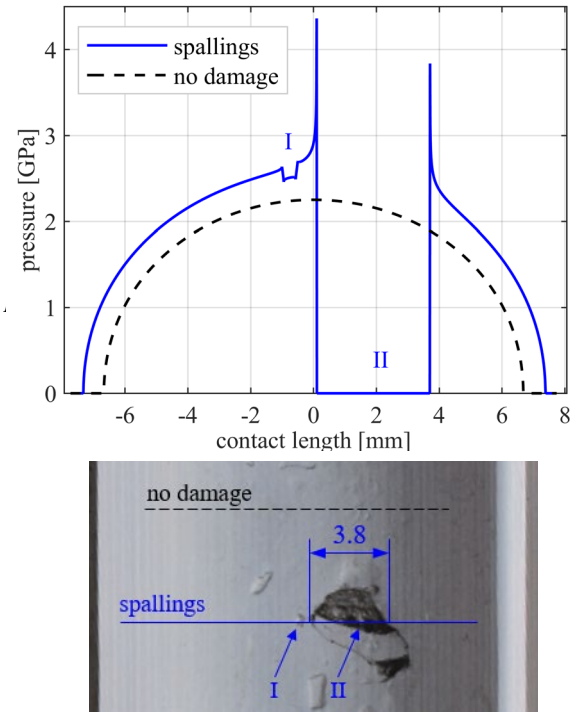

6.6. Osculation

An advantage of the analytical study of truncated contacts is the flexibility to quickly investigate other contact geometries for their suitability without a complex FEM result analysis. Figure 19 shows the same truncated contact on the inner ring from Figure 14, which has an osculation of ~3.85 %. Changing this osculation also results in a change of the contact pressure. With this method, it is therefore also possible to efficiently determine the optimum osculation under any load situation.

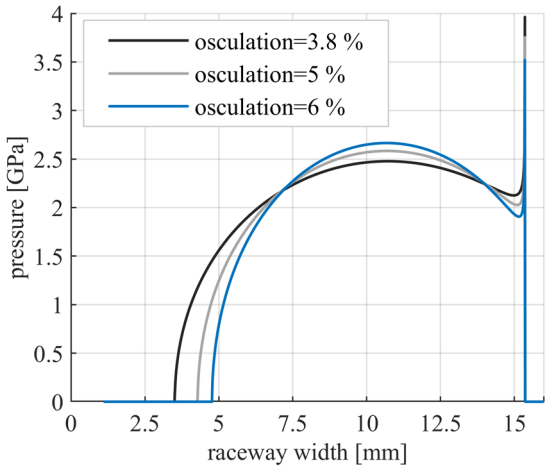

Figure 19: Osculation influence

7. Conclusions and Perspective

With the application of the AST model for a blade bearing, this paper shows an alternative method to the Hertzian Contact theory for local raceway stress analysis, which can also investigate impaired raceways. For this, contact modeling is necessary, otherwise, a surrogate element model can be applied. To determine a load case that exceeds the capabilities of surrogate elements, a global rotor star model was extended to include a contact simulation for locally detailed solid rolling elements to be set up at any arbitrary position. Thus, critical contacts can be analyzed considering the blade-hub joint structure and the composition of the load spectrum.

The degree of discretization of the two models corresponds to a trade-off between convergence and efficiency. Apart from a closer agreement between AST and FEM for the impairment-free contact regions, the pressure peaks at the raceway edges converge only for a discretization with very high resolution. This is especially difficult in a global FE approach regarding computational capacity. Therefore, it is recommended to derive a scaling factor from a mesh study of the raceway edge to subsequently scale the simulated pressure peak according to similar recommendations for the AST model by Houpert.

In addition to the high analysis efficiency, the AST model also allows for the investigation of interesting effects of damaged raceways, such as a magnified contact profile next to the formation of a pressure peak in case of damaged raceways. Since Hertz is not suitable for studying interrupted pressure curves, the model provides the fastest, but also conservative results. A load capacity potential is implied by using

AST and FEM against the permissible pressure directly.

For upcoming research it would be interesting, if a more detailed design criterion than a single value of a permissible pressure leads to a more accurate load capacity design, taking into account the local pressure distribution calculation.

Acknowledgment

The depicted investigation is part of the joint project HBDV analyzing the technical design of highly loaded slewing bearings. The project was funded by the Federal Ministry for Economics and Climate Action (BMWK).
Funding code: 0324303C

Supported by:

Federal Ministry
for Economic Affairs
and Climate Action

on the basis of a decision
by the German Bundestag

References

[1] DIN 26281:2010, Rolling bearings – Methods for calculating the modified reference rating life for universally loaded bearings (ISO/TS 16281:2008 + Cor. 1:2009)

[2] O. Menck, M. Stammler, F. Schleich, “Fatigue lifetime calculation of wind turbine blade bearings considering blade-dependent load distribution”, Wind Energy Science 26 (2020)

[3] DIN ISO 76:2006 + Amd.1:2017, Rolling bearings – Static load ratings, (2019)

[4] DIN ISO 76-1:1994, Rolling bearings – Static load ratings – Explanatory notes to ISO 76; identical with ISO/TR 10657:1991, (1994)

[5] Daidié, Z. Chaib, A. Ghosn, “3D Simplified Finite Elements Analysis of Load and Contact Angle in a Slewing Ball Bearing”, Journal of Mechanical Design 130 (2008) 082601-1

[6] L. Kania, “Modelling of rollers in the calculation of slewing bearing with the use of finite elements“, Mechanism and Machine Theory 41 (2006) 1359-1376

[7] S. Zupan, I. Prebil, “Carrying angle and carrying capacity of a large single-row ball bearing as a function of geometry parameters of the rolling contact and the supporting structure stiffness“, Mechanism and Machine Theory 36 (2001) 1087-1103

[8] Amasorrain, X. Sagartzazu, J. Damián, “Load distribution in four contact-point slewing bearing“, Mechanism and Machine Theory 38 (2003) 479-496

[9] T. Lazovic, M. Ristivojevic, R. Mitrovic, “Mathematical Model of Load Distribution in Rolling Bearing“, FME Transactions (2008) 36, 189-196

[10] M. Olave, X. Sagartzazu, J. Damián, A. Serna, “Design of Four Contact-Point Slewing Bearing With a New Load Distribution Procedure to Account for Structural Stiffness“, Journal of Mechanical Design 132 (2010) 021006-1

[11] G. Chen, J. Wen, “Load Performance of Large-Scale Rolling Bearings With Supporting Structure in Wind Turbines”, Journal of Tribology 134 (2012) 041105-1

[12] M. Krynke, L. Kania, E. Mazanek, “Modelling the contact between the rolling elements and the raceways of bulky slewing bearings”, Key Engineering Materials 490 (2012) 166-178

[13] J. Aguirrebeitia, M. Abasolo, R. Avilés, I. Fernandez de Bustos, “General static load-carrying capacity for the design and selection of four contact point slewing bearings: Finite element calculations and theoretical model validation.” Elsevier, Finite Elements in Analysis and Design 55 (2012) 23-30, doi: 10.1016/j.finel.2012.02.002

[14] H. Hertz, „Über die Berührung fester elastischer Körper“, Jounal für die reine und angewandte Mathematik 92 (1881) 56–171

[15] R. Teutsch, “Kontaktmodelle und Strategien zur Simulation von Wälzlagern und Wälzführungen“, Technische Universität Kaiserslautern, (2004)

[16] H. Reusner, „Druckflächenbelastung und Oberflächenverschiebung im Wälzkontakt von Rotationskörpern“, Karlsruher Institut für Technologie, (1977)

[17] J. Tripp, “Hertzian Contact in Two and Three Dimensions“, NASA Technical Paper Series, 2473 (1985)

[18] L. Houpert, “An Engineering Approach to Hertzian Contact Elasticity-Part I“, Journal of Tribology, 123 Nr. 3 (2000) 582–588, doi: 10.1115/1.1308043

[19] L. Houpert, “Novel analytical and numerical calculations in truncated contact“, Bearing World Journal 4 (2019) 39-58

[20] K. Kunert, „Spannungsverteilung im Halbraum bei elliptischer Flächenpressungsverteilung über einer rechteckigen Druckfläche”, Forschung auf dem Gebiete des Ingenieurwesens 27 Nr. 6 (1961) 165-174, doi: 10.1007/BF02561354

[21] IEC 61400-1:2005 + A1:2010, deutsche Fassung EN 61400-1:2005 + A1:2010 Design requirements (VDE-Bestimmung VDE 0127-1) Berlin, (2011)

[22] E. Paland, „Die Lastverteilung in einem auf der Ebene abgestützten Zylinderrollenlager”, Maschinentechnik (Schmierungstechnik), 8 Nr. 17 (1968)

Influence of surface mutation and parasitic current flow on the impedance measurement

Josephine Klingebiel[1], Simon Graf[2], Maik Schröder[1], Simon Hausner[1], Oliver Koch[2], Bernd Sauer[2],

[1] *flucon fluid control GmbH, info@flucon.de*

[2] *Chair of Machine Elements, Gears and Tribology (MEGT), Technische Universität Kaiserslautern*

Experimental results are presented showing the effects of surface changes due to parasitic bearing currents on the measured impedances of an axial bearing. Operating point-dependent impedance curves have proven useful for the electrical characterization of a mechanical machine element in order to estimate the current densities that occur. However, the changes in impedance as a result of surface changes caused by the electric current are largely unknown and will be examined in more detail in the present investigations. For this purpose, impedance curves on a 51208 axial rolling bearing are measured under defined operating conditions using the E-Lub Tester, a new test rig developed by flucon fluid control GmbH, and are defined as a reference. The E-Lub Tester is then used to selectively generate electrical breakdown currents that cause surface mutations (corrugations/discharge cra- ters/surface smoothing). These emerging surfaces are measured and documented using a confocal microscope at MEGT. In the following, the operating points of the bearing reference condition are applied again by means of the E-Lub Tester and the changes in impedance due to the surface modification are investigated. No further ex- amination of the lubricant is carried out. However, by changing the oil regularly, any influence on the results (as a consequence of electrical damage done to the lubricant) is excluded. Finally, the results are to be correlated to a simplified lubrication gap height calculation and tribologically equivalent conditions are to be compared.

Keywords – *bearing currents, bearing impedance, surface mutation, measuring system, breakdown voltage, EDM*

1. Introduction

The flow of parasitic electric currents in rolling bearings is a phenomenon caused by more common use of variable-speed drive trains with power inverters. This unintended current in the lubrication gap can damage and influence both the bearing and the bearing lubricant. [Koh43], [Mue04], [Fur17], [MG21], [GS21].

Typical damage patterns that can occur during this process and will be demonstrated in our experiments are shown in Figure 1. These patterns are: a) isolated craters as a result of discharges, b) ripples and c) so-called grayfrosting caused by ohmic current flow.

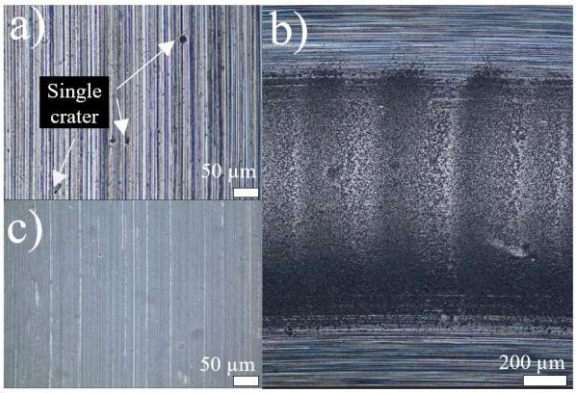

Figure 1: Microscopic images of damage caused by electrical breakthrough: a) discharging craters, b) fluting-caused ripples, c) grayfrosting

In addition, electric currents may change the lubricant properties [Mue04], [Jag05] [Bec20], which may lead to the occurance of white etching cracks (WECs) [LBG21], [HBM+23] and increased discharge-based grayfrosting. [Rad16], [Gem17]

For the prediction and determination of the parasitic currents, electrical impedance simulations [Pre02], [Gem16], [MG21] as well as the measurement of the bearing impedance [Pre02], [Bec20] have proven themselves.

The following investigations are to determine the in- fluence of surface changes caused by the passage of electric current on the impedance measurement. It has already been shown [MBK22] that it is possible to de- tect raceway damages in rolling bearings by means of the physical quantity of the impedance. Following this concept, rolling bearing raceways are first damaged electrically in a defined manner (cf. Figure 1). The change in impedance and its characteristics are then analyzed under various mechanical operating condi- tions. Furthermore, interactions between the measured bearing impedance and the electrical load are demon- strated within the scope of the series of tests presented here.

For our investigations we used a new thrust bearing tester designed by flucon fluid control GmbH which was based on the GESA adapter developed in FVA 650 II [BW20].

2. Methodology and experimental setup

The electrical damage of bearings is investigated by focussing on the surface mutation of the raceway. The test procedure is illustrated in the diagram below (Fig- ure 2).

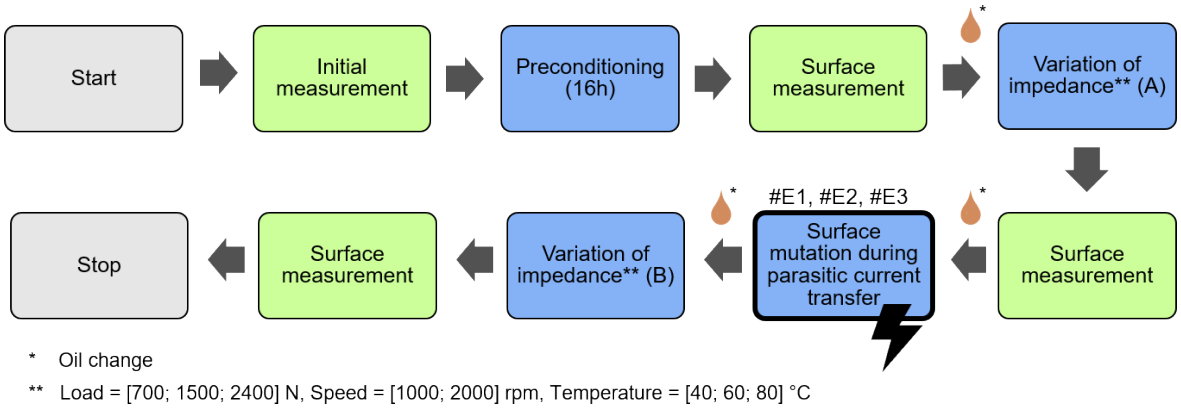

Figure 2: Test procedure

Before initial operation, the surface of the bearing raceway is measured by means of a *µsurf* confocal microscope. This is followed by a 16-hour running-in period based on the procedure of [Bec20], which is documented through an hourly impedance measurement. After this, the surface is measured again. The lubrication condition is then modified by variation of the mechanical boundary conditions. Following this, the different electrical boundary conditions according to Table 1 are applied.

Table 1: Electrical boundary conditions

Number of experiment	Operating point	Electr. load (type)	Running time
#E1	1,500 N 1,000 rpm 40°C 30 V (pk to pk)	hourly 60 ms pulse	10 h
#E2	1,500 N 1,000 rpm 40°C 3 A (constant)	permanent DC load	10 h
#E3	1,500 N 1,000 rpm 80°C 40 V (pk to pk)	permanent AC load	72 h

These conditions are based on flucon's experimental experience, supported by results from the research project [GS21] and [GCK23]. During experiment #E1 breakdown voltages are applied for a short exposure time (60 ms) to check if permanent effects of electrical discharge machining (EDM) currents can already be found through measurement of the impedance. In this case EDM craters are expected. In experiment #E2, the bearing is loaded permanently with a constant DC voltage. The aim here is to compare the results with respect to the signal shape for otherwise identical operating conditions. In this particular case, flutings are created.

Experiment #E3 is intended to investigate the influence of an increased temperature - and therefore of a thinner lubricant film - under electrical load.

The fundamental question behind this series of experiments is whether it is possible to give systematic diagnoses of surface damages through indication of the bearing impedance, and whether this can be achieved with a newly developed test rig which is introduced in the next chapter.

2.1. E-Lub Tester

Test bench description

Based on the device for extended lubricant analysis (*GESA*) designed during the *FVA 650 II* project [BW20], the *E-Lub Tester* was developed. This is a test adapter for the four-ball tester (*FBT*) which makes it possible to define mechanical boundary conditions for the rolling bearing system while applying an electrical load and monitoring the electrical properties of this system. The *FBT* is used to define the speed and axial force while the *E-Lub Tester* has a temperature control circuit with a heated and refrigerated circulator which allows to maintain a constant temperature during the variation of the boundary conditions. Furthermore, it is possible to define electrical boundary conditions, such as the applied voltage and the switching frequency, for the test device. This will lead to EDM events at which breakdown currents flow that are harmful to both bearing and bearing lubricant. Fluting is a typical form of damage that results from the electromechanical stress on axial bearings used in many electric drive applications.

For the presented experiments, an *E-Lub Tester* is equipped with an *SKF 51208* axial bearing. By means of a special centering pin and a driving shaft (Figure 3) the test cell is fitted into the *FBT*. Thanks to the two-piece design of the cell housing, the test bearings can be swapped easily. To protect the operator from the rotating parts of the measuring unit, a contact protection is mounted on top of the test cell.

The hoses for temperature control are integrated in the test cell handle to minimize the risk of burns and leakage. The temperature of the bearing lubricant can then

be controlled automatically by the connected circulator. The *E-Lub Tester* software offers various predefined measurement campaigns as well as a freely configurable analysis mode. A DIN standard for comprehensive testing by means of the *E-Lub Tester* is currently being developed.

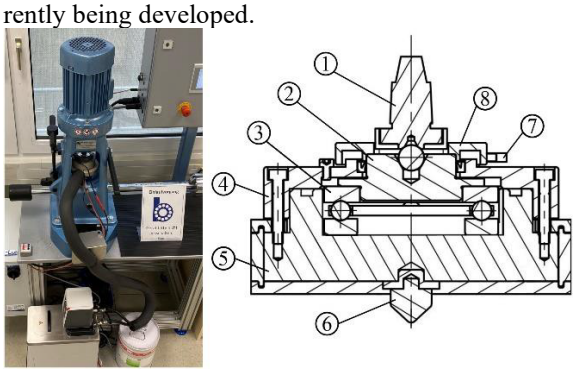

Figure 3: left: E-Lub Tester (PC not shown), right: Sectional view of E-Lub Tester test cell: 1- driving shaft; 2- shaft; 3- test bearing; 4- cell housing; 5- main cell body with inte- grated cooling ducts; 6- centering pin; 7- sliding contact; 8- sliding ring

Mechanical load

With the now modified *FBT* a mechanical load of 700 N, 1,500 N and 2,400 N respectively and a rotational speed of 1,000 rpm are applied to the axial bearing.

Table 1 presents the calculated values of both the Hertzian pressure and the Hertzian contact area on the raceway surface for each of the applied mechanical loads. In combination with the given speed, temperature and type of lubricant used for these specific experiments the different operating points will represent a wide range of lubrication forms, covering relatively large lubrication gap heights as well as the mixed friction area.

Table 2: Results for Hertzian pressure and area for one ball-raceway contact

Load [N]	max. Hertzian pressure [bar]	Hertzian area [mm²]
700	8,088	0.0577
1,500	10,428	0.0959
2,400	12,197	0.1312

Lubricant

LUBCON F56 base oil was chosen for all of the experiments as part of the intended standardization. This fluid is already known from *FVA 650 II [BW19]*. Its relevant electrochemical and physical properties were determined using flucon's *EPSILON+* Dielectricity Meter, *QVis* Viscometer and flucon's high-pressure fluid laboratory.

Table 3: Properties of LUBCON F56 base oil

		40°C	60°C	80°C
kinematic viscosity	ν [mm²/s]	130.4	47.5	21.95
dynamic viscosity	η [mPas] @ 1,000 barg	903.39	242.52	87.76
	η [mPas] @ 2,000 barg	5.78E+03	1.09E+03	3.11E+02
	η [mPas] @ 8,000 barg	N/A	1.22E+07	4.02E+05
	η [mPas] @ 10,000 barg	N/A	6.33E+08	6.27E+06
	η [mPas] @ 12,000 barg	N/A	N/A	1.41E+08
pressure viscosity coefficient	α_p [1/bar] @ 2,000 barg	0.0019326	0.0016024	0.0013784
specific electrical conductivity	κ [nS/m] @ 0 barg	0.101	0.400	1.214
relative permittivity	ε_r @ 0 barg	2.277	2.249	2.222
dielectric dissipation factor	tan δ @ 0 barg	0.016	0.064	0.196

2.2. Electrical system

The *E-Lub Tester* mainly consists of a control cabinet and a test cell (Figure 4) which includes the test bearing and which is mounted into the four-ball tester. An additional software for Windows PCs is available as a user interface. The test cell is connected to the control cabinet by means of three individual sensor cables (connecting the housing shell, shaft shell and PT100 temperature sensor). At the *Institute of Machine Ele- ments, Gears and Transmission* (*MEGT*) of the *Tech- nical University of Kaiserslautern* a series of synthetic frequency converters was developed and well-tried in the context of the research project *FVA 650 I* [GS21]. Based on the method used here the *E-Lub Tester* includes an arbitrary waveform generator (AWG) capable of generating different waveforms with individual switching frequencies (up to 500 kHz). For our experiments we chose a switching frequency of 10 kHz. The maximum electrical load is 40 V peak to peak (pk to pk). The measurement of both impedance and parasitic bearing currents is performed automatically. Before each test the operator sets the desired load and speed by means of the four-ball tester, which are then also defined as parameters in the software.

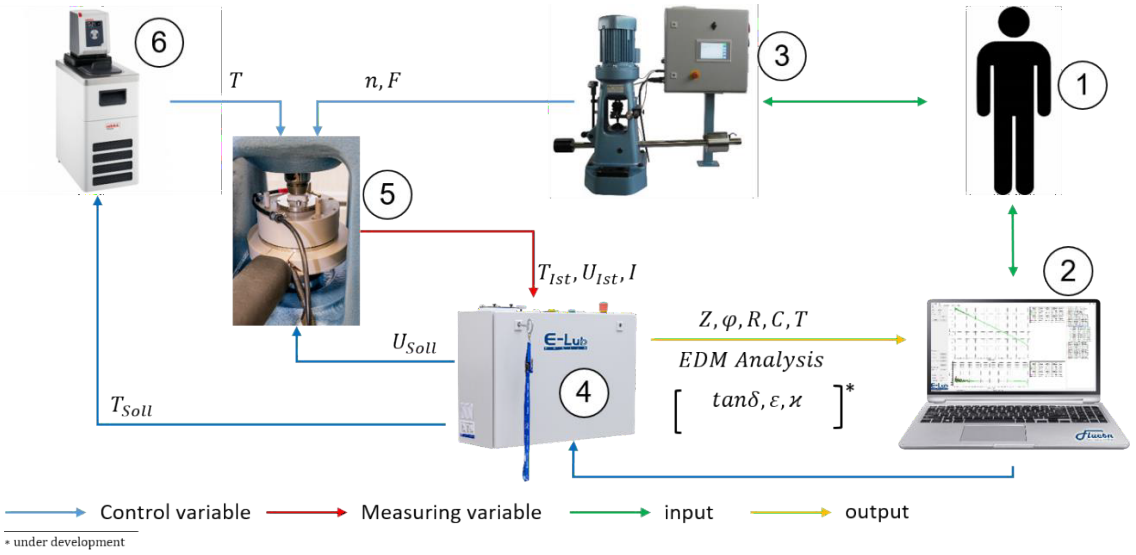

Figure 4: Components and workflow of the E-Lub Tester: 1- operator; 2- PC with E-Lub Tester software (Windows); 3- FBT Hansa VKA-110; 4- E-Lub Tester control cabinet; 5- E-Lub Tester test cell (FBT adapter); 6- circulator

Impedance measurement

Each lubricant has a specific electrical conductivity and a permittivity. Both are temperature-dependent values that can be calculated by determining the com- plex impedance of the medium. The equivalent circuit diagram shows an ohmic resistor and a capacitance, which are connected in parallel (Figure 5).

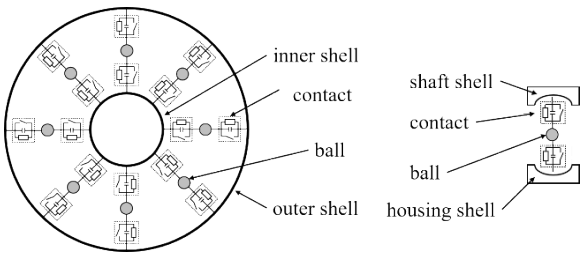

Figure 5: Circuit diagram of a radial bearing (left) and thrust bearing (right)

For our circuit the following equations were used for the resistance and the capacitance:

$$C \sim \varepsilon_0 * \varepsilon_r * A_{Hertz}/h_0 \qquad (Eq.\ 1)$$

$$R \sim 1/\kappa * h_0/A_{Hertz} \qquad (Eq.\ 2)$$

The impedance is measured by applying an AC voltage. In the process the current is measured according to magnitude and phase.

Therefore, the impedance can be described as:

$$1/\underline{Z} = 1/R + j * \omega * C \qquad (Eq.3)$$

For the measurement of the permittivity, the imaginary part is decisive. It is therefore favorable to choose a high frequency. For the measurement of the specific electrical conductivity, on the other hand, a low frequency is favorable because the imaginary part becomes small and thus the decisive real part predominates.

This of course applies to a fixed geometry, or to a defined operating condition, once that is constant. In the rolling bearing the relevant geometries (contact sur- face area and gap height) can vary greatly due to the wide range of applications. The test cell of the *E-Lub Tester* was therefore designed in such a way that the real-life operating range can be represented by varia- tion of the (bearing and lubricant) temperature, force and speed.

All of these parameters affect the lubricant film. This in turn influences the ohmic and capacitive behavior, which is shown in Figure 6.

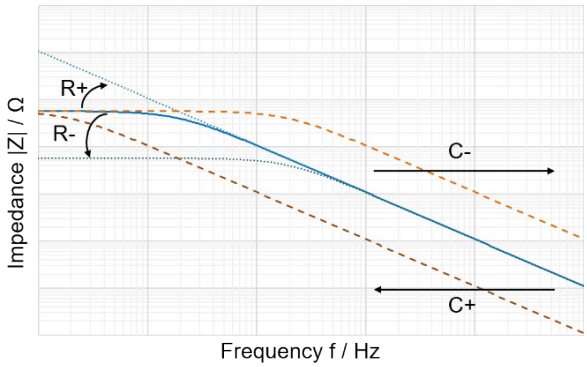

Figure 6: Change of bearing impedance

3. Results and discussion

Based on the presented test rig and measuring procedure, the results of the experiments are presented and discussed below.

3.1. Surface mutations

As a result of the mechanical and electrical loads applied to the test bearing, changes in its raceways occur. A confocal microscope is used for the three-dimen- sional measurement of the surface roughness of the bearing raceway. As shown in Figure 7, these meas- urements can be visualized through different tech- niques. Thus, the cumulative frequency functions of the profile heights (also referred to as the Abbott-Fire- stone curve [AF33]) are shown here. Furthermore, contour plots also visualize the individual surfaces. For the sake of comparability, the Abbott Firestone curves of the experiments #E1, #E2 and #E3 are shown for the fixed and for the rotating ring respectively. Through additional investigation of the microscopic pictures of the surface topography it can be found that c) #E2-fixed, d) #E2-rotating and f) #E3-rotating show stronger raceway surface mutations compared to the electrically less loaded experiment #E1. For #E1 there is only a minor change in the bearing raceway with in- dividual EDM craters on the fixed ring. The rotating ring of this test shows no abnormalities. In contrast, experiment #E2 creates a pronounced fluted structure on the fixed ring with a maximum ripple depth of ap- proximately 2,0 µm. On the rotating ring, individual craters and a strongly smoothed raceway are visible. In experiment #E3, a pronounced smoothing of the race- way occurs on the fixed ring. In consequence, the sur- face machining traces found for a) #E1-fixed are no longer present.

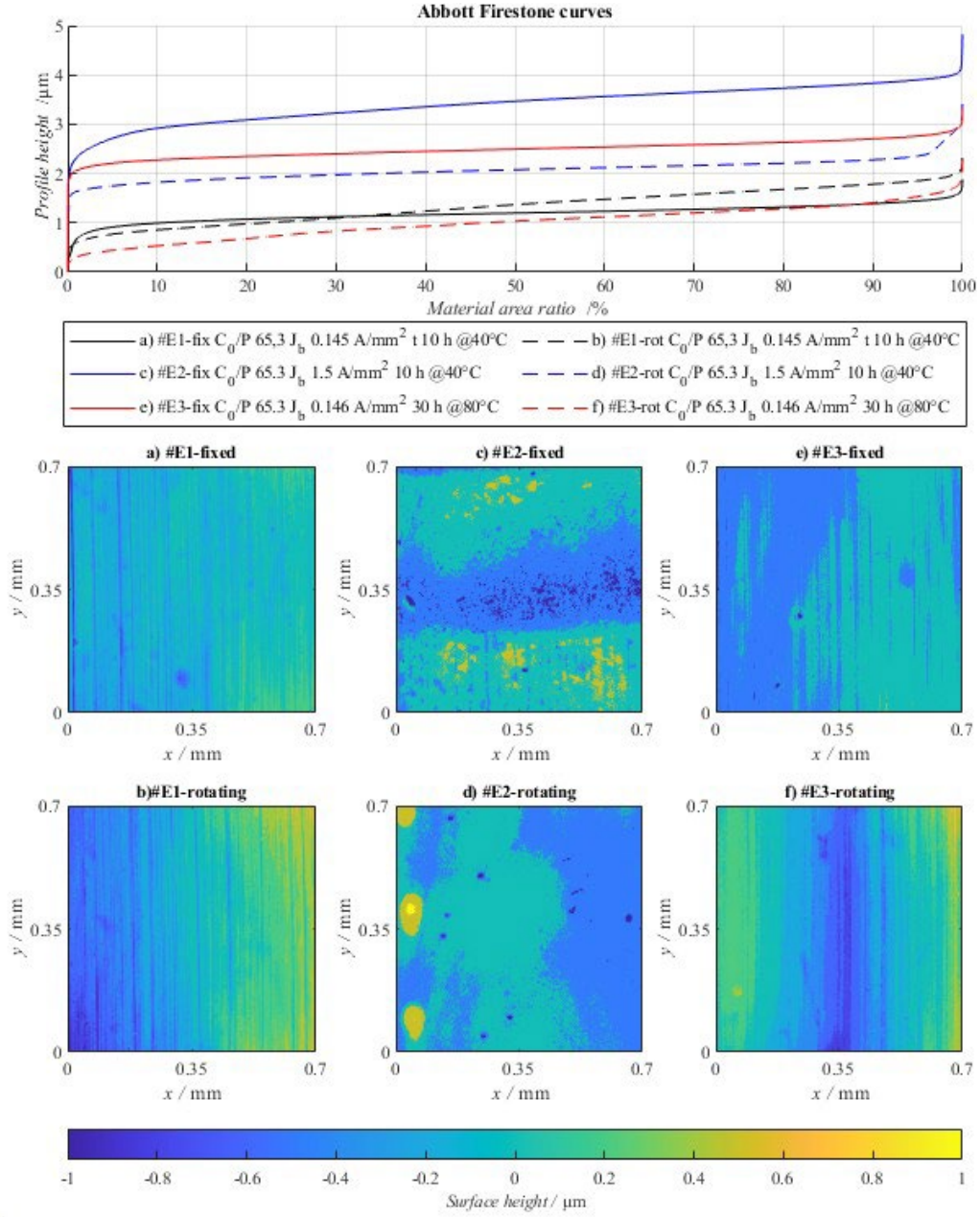

Figure 7: Visualization of the experimentally generated surface mutations with Abbott Firestone curves and contour plots. The surface measurements were taken from the middle of the raceway

3.2. Impedance change due to surface mutation

It can be found that while the microscopic analysis for #E1 shows only minor damages in the raceway surfaces of both rotating and fixed shells, there are significant deviations in the measured impedance before and after the experiment (Figure 8).

For instance, for #E1 at 40°C one can't observe a significant change in resistance when comparing the impedance before and after application of the electrical load. While at the beginning there is pure capacitive dissipation, due to the gradual surface damage, the bearing impedance changes to the extent that there is now an increased resistance in the system.

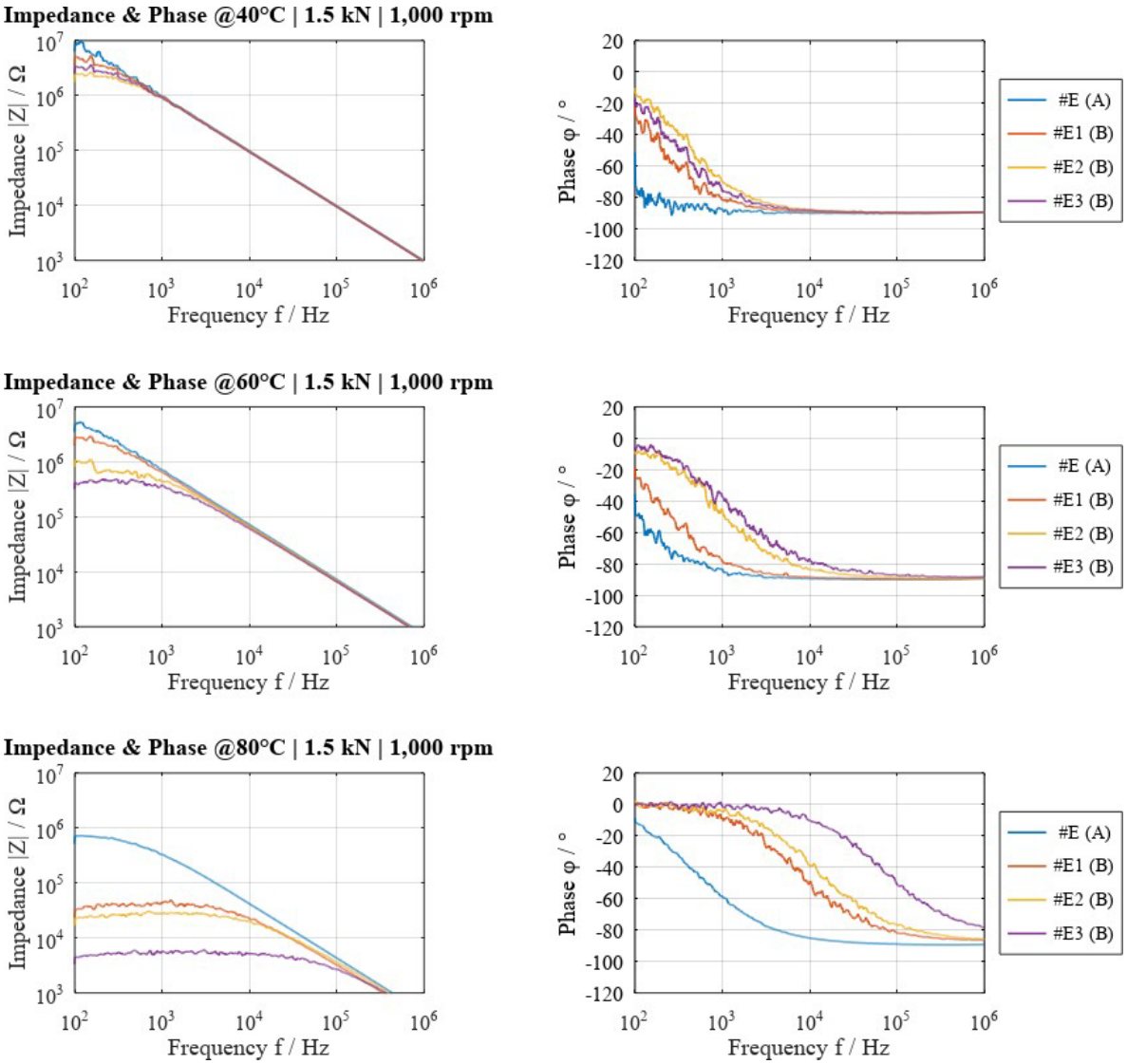

Figure 8: Comparison – Measurement of impedance and phase before (A) and after (B) application of electrical load

The deviation of the impedance then increases significantly with an increasing temperature and thus with a decreasing lubrication gap (80°C). Looking at the additional surface data (Figure 7), it becomes obvious that even a low running time under electrical load is sufficient to create multiple EDM craters. By adjusting the electrical load applied with the *E-Lub Tester*, it is possible to measure the equivalent changes in the impedance, too (Figure 9).

3.3. Impedance change due to electrical current flow

As a result of the experiments, a further influencing parameter to the bearing impedance was identified: a significant temporary change in the impedance and the phase angle occurred right after the application of the electrical load was stopped. This phenomenon could be identified in all of the experiments.

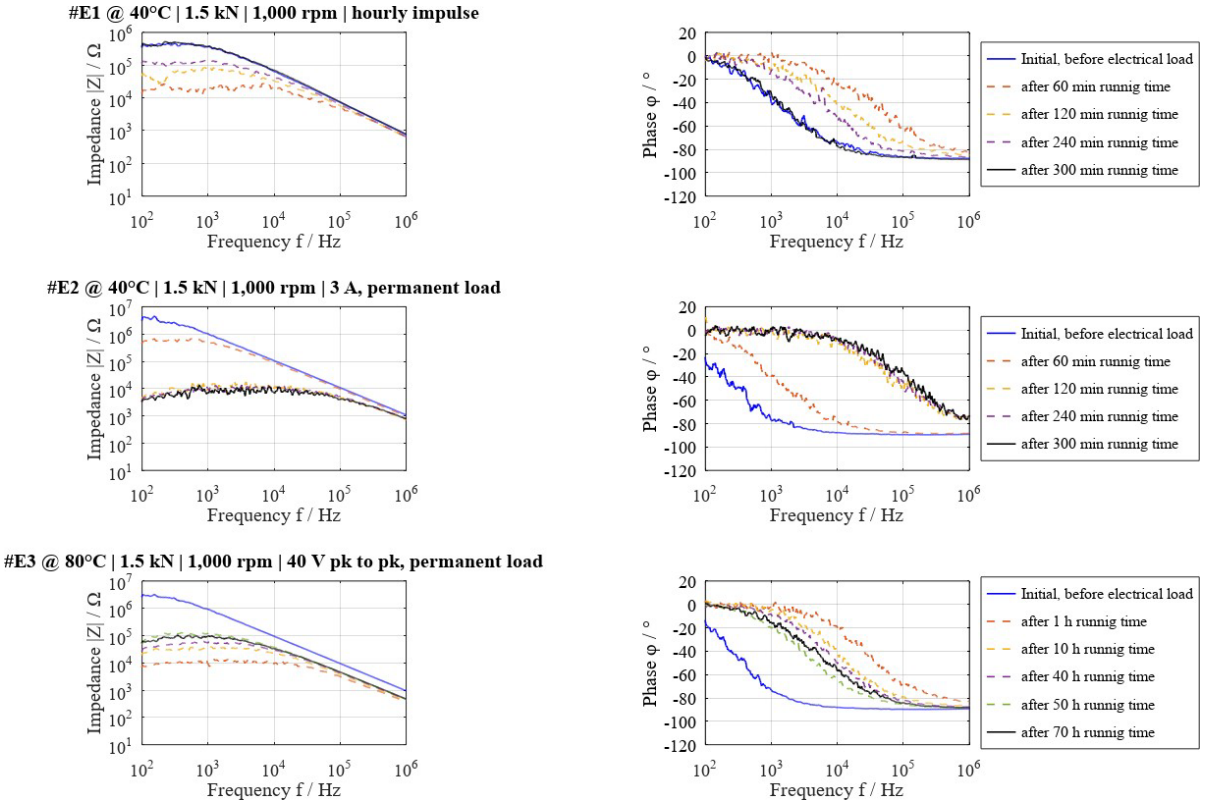

Figure 9: Bearing impedance over experiment running time

The impedance measurement was taken right after the electrical load was stopped. For #E1 the impedance was measured after the hourly impulse of 60 ms with a delay of two minutes. For #E2 the impedance was determined every hour. For this measurement the elec- trical load was stopped for only two minutes. For #E3 the electrical load was interrupted for two minutes as well to measure the impedance.

As the results for #E1 show, the impedance is decreased massively early on in the experiment. This effect may be caused by a conductive channel that is being built up in the lubrication gaps. As the application of the electrical load is continued, the impedance seems to return to its original magnitude.

Compared to #E3, this process happens rather quickly with #E1.

Apparently the observed effect of impedance change induced by parasitic current is a temporary effect and depends on the time of exposure to the electrical load.

In order to investigate this phenomenon more closely, further tests were carried out. Here it was found that at a voltage of 30 V pk to pk applied to bearing #E1 for 60 ms required 30 minutes before the initial impedance magnitude before energization was reached again.

Investigation of this effect of "impedance recovery" was carried out analogously on a new bearing (#E4). Since there was no surface mutation here, we see a dif- ferent impedance response. However, the impedance drift is equally pronounced (Figure 10). The first meas- urement after the electrical load was applied showed a significantly lower impedance magnitude than what was found in the following minutes; the phase angle also remained at 0° up to a higher frequency before dropping into the negative range. With increasing run- ning time without further electrical load these values will go back to their starting level, as the last two meas- urements show for each case.

The reason for the observed behavior is assumed to be an interaction between the current flow and the dielec- tric strength of the lubricant. The dielectric strength represents a critical field strength at which complete potential separation is no longer given. In general, the dielectric strength of liquid insulating materials de- creases due to ionization, i.e. due to freely moving pos- itive and negative ions, which can occur, for example, due to moisture absorption, dissolved gases or lubri- cant contamination [Küc09]. The behavior observed in the impedance measurement consequently suggests an interaction between free ions of the lubricant and the electric field. One possible reason could be gas mi- crobubbles, which are prevented from growing into larger bubbles and outgassing. Another possibility would be metallic wear particles, which are held in suspension by the electric field. In either case, dielec- tric strength would be degraded by conductive compo- nents in the lubricant until the recovery process is com- pleted. Regardless of the cause of the recovery phe- nomenon, it can be seen that stabilization of imped- ance magnitude and phase angle must be waited for even after electrical load was ceased before impedance measurements are a reliable parameter for the liquid dielectric in the lubrication gap.

This is especially true when comparing electrome- chanical tests and solely mechanical tests, since the ef- fect does not occur in the latter due to the lack of ener- gization.

It has to be said that these results represent a first study and therefore there is no claim to completeness yet. This will be the subject of further research conducted by *flucon* and *MEGT*.

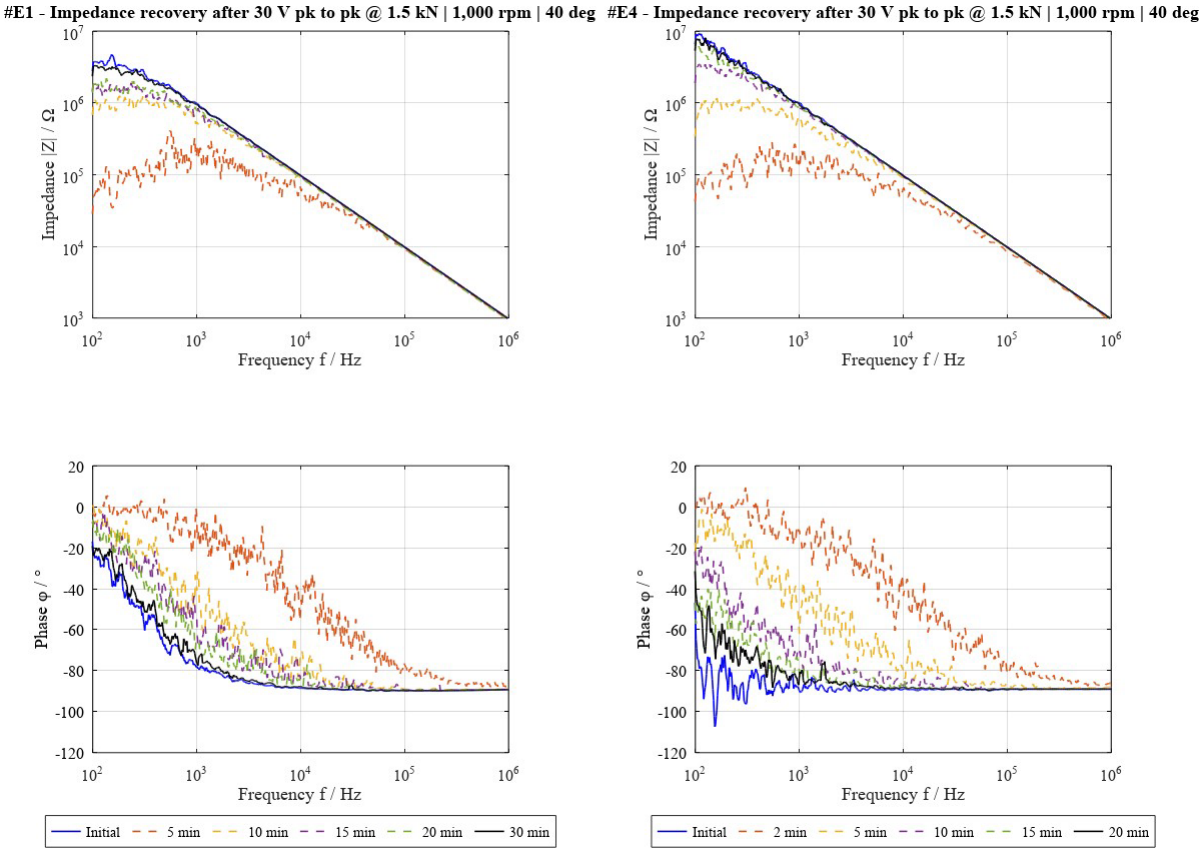

Figure 10: Bearing impedance recovery

4. Conclusions

The aim of this investigation was to test a measuring system that enables the setting of electromechanical operating points and the simultaneous measurement of the bearing impedance. Furthermore, the relationship between the impedance and the surface damage of the bearing raceways caused by parasitic currents was analyzed.

For this purpose, the bearing raceways were first predamaged in different ways by means of an electrical load. This resulted in the test bearings of #E1 to #E3, which were further analyzed by means of impedance measurement. The results from these investigations were then compared to the impedance of a solely mechanically loaded test bearing. This was done at three different mechanical operating points. In order to classify the surface mutations, they were measured and described using common methods.

In addition to comparing the change in impedance caused by mutations of bearing raceway surfaces, the change in impedance over time as a result of a permanent electrical load was investigated.

In summary, it can be seen that the electrically induced mutations also show up in the impedance measurement. The current flow through the lubricant results in a decrease of the impedance value as well as a shift of the phase angle towards 0°. This shift depends on the degree of surface change and the tribological condition of the rolling contact. In full lubrication the effect is rather small, whereas in mixed friction there is a more pronounced discrepancy of the impedance due to the surface change (compare to fig. 8).

In conclusion it can be said that through the tests #E1 to #E3 the bearing raceways were damaged in different ways and that the gradual modification of both the bearing components and the bearing lubricant can be tracked by means of impedance measurement. The bearing impedance very much correlates with the sur- face condition of the bearing raceway. Thus, *flucon's E-Lub Tester* is able to monitor and evaluate the per- formance of a lubricant that is exposed to various elec- tromechanical boundary conditions.

In addition to these investigations, it was found that there are temporary changes in impedance as a result of the electrical load (compare to Fig. 10). The gradual return to the initial magnitude is further referred to as *impedance recovery*. The effect of the temporary change in impedance as a result of parasitic current

flow through the tribological contact described here needs to be investigated more closely to clarify its causes. Clearly, the consequence of such an effect is that for the monitoring of endurance tests under com- bined electrical and mechanical load, changes in im- pedance can no longer be clearly attributed to only sur- face changes or electrical aging of the dielectric. Therefore, it is necessary to analyze the temporal con- text of each measurement. Furthermore, it must be checked if an actual impedance measurement triggers this effect and whether there is a possible mutual influ- ence.

The E-Lub Tester is currently being further-developed to determine the lubrication gap height on the basis of the impedance. Furthermore, an evaluation of the dif- ferent types of parasitic currents is in progress, so that an electromechanical characterization can be carried out for any type of lubricant.

Acknowledgment

This work was carried out within the framework of the project "Entwicklung eines Prüfstands zur Bestimmung der elektrischen und dielektrischen Eigenschaften von Schmierstoffen unter Prozessbedingungen" (Project No. KK5124301BD0), which was financially supported by *Bundesministerium für Wirtschaft und Klimaschutz (BMWK)* and Zentrales Innovationszent- rum Mittelstand (*ZIM)*. Special thanks to the Tribo- Electrical Contact *TEAM* at *MEGT, Technical Univer- sity Kaiserslautern* for providing the surface measure- ments for the shown experiments.

References

[AF33] Abbott, E.; Firestone, F.: Specifying Surface Quality - A Method Based on Accurate Measurement and Comparison. Mechanical Engineering 55, 1933.

[Bec20] Bechev, D.: „Prüfmethodik zur Charakterisierung der elektrischen Eigenschaften von Wälzlagerschmierstoffen“. Diss., Kaiserslautern: Technische Universität Kaiserslautern, 2020.

[BW20] Bechev, D.; Weicker, M.: Schädlicher Stromdurchgang II - Methodik zur praxisnahen Charakterisierung von elektrischen Schmierstoff-eigenschaften zur Verbesserung der rechnerischen Vorhersage von Lagerströmen: FVA-Forschungsvorhaben 650 II – Abschlussbericht, Heft 1387, Frankfurt am Main, Forschungsvereinigung Antriebstechnik e.V., 2020.

[Fur17] Furtmann, A.: „Elektrisches Verhalten von Maschinenelementen im Antriebsstrang“. Diss., Han- nover: Universität Hannover, 2017.

[Gem16] Gemeinder, Y.: „Lagerimpedanz und Lagerschädigung bei umrichtergespeisten Antrieben”. Diss., Darmstadt: Technische Universität Darmstadt, 2016.

[GCK22] Graf, S.; Capan, R.; Koch, O.: „Wechselwirkung von Tribologie und elektrisch induzierter Oberflächenmutation in Wälzlagern“. Aachen, 2022. 5. VDI-Fachkonferenz – Schadensmechanismen an Lagern.

[GS21] Graf, S.; Sauer, B.: „Surface mutation of the bearing raceway during electrical current passage in mixed friction operation“. Bearing World Journal, Volume 5, 2021, S. 137–147.

[HBM+23] Holweger, W.; Bobbio, L. Mo, Z.; Fliege, J.; Goerlach, B.; Simon, B.; „A Validated Computa- tional Study of Lubricants under White Etching Crack Conditions Exposed to Electrical Fields”. Lubricants, Volume 11(2):45, 2023.

[Koh43] Kohaut, A.: „Riffelbildung in Wälzlagern infolge elektrischer Korrosion“. Habilitationsschrift, Würzburg: Julius-Maximilians-Universität Würzburg, 1943.

[Küc09] Küchler, A.: „Hochspannungstechnik - Grundlagen - Technologie – Anwendungen“. Berlin Heidelberg: Springer Verlag, 2009.

[Mar21] Martin, G.: „Die Wälzlagerimpedanz als Werkzeug zur Untersuchung von Oberflächenabwei- chungen in Wälzlagern“. Diss., Darmstadt: Technische Universität Darmstadt, Institut für Produktentwick- lung und Maschinenelemente, 2021.

[MBK22] Martin, G.; Becker, F.; Kirchner, E.: “A novel method of diagnosing rolling bearing surface damage by electric impedance analysis”. Tribology In- ternational, Volume 170, 2022.

[Pre02] Preisinger, G.: „Cause and effect of bearing currents in frequency converter driven electrical mo- tors: Investigations of electrical properties of rolling bearings“. Diss., Wien: Technische Universität Wien, 2002.

[RG15] Radnai, B.; Gemeinder, G.: Schädlicher Stromdurchgang I - Untersuchung des Schädigungs- mechanismus und der zulässigen Lagerstrombelastung von Wälzlagern in E-Motoren und Generatoren, verur- sacht durch parasitäre hochfrequente Lagerströme: FVA-Forschungsvorhaben Nr. 650 I, FVA-Heft 1127, Frankfurt /Main, Forschungsvereinigung Antriebs- technik e.V., 2015.

Investigation of the electrical properties of lubricating greases with a di-electrorheological measuring device

Thomas Litters, Laurin Schmitt, John Burbank, Jürgen Rausch, Mathias Ronellenfitsch [1],

[1] *FUCHS LUBRICANTS GEMRANY GmbH, Germany*

Abstract– The combination of a rotational rheometer and an impedance spectrometer opens new possibilities for investigating lubricating greases and their base oils. Dielectric properties can be examined under a variety of shear stresses and temperature range. Measurands such as impedance, conductivity and dielectric constant or permittivity can be determined and provide additional information for the design of grease-lubricated tribological systems when an electrical field is present at the same time.

Keywords– Lubricating greases, dielectric rheology, impedance, permittivity

1. Introduction

The increased electrification of automobile drivetrains makes it necessary to better understand the electrophysical and -chemical properties of lubricants. Research projects such as FVA 650 I and II have already intensely investigated the influence of grease lubrication on the endurance of rolling bearings under electrical influence. In these projects the electrical conductivity, as well as impedance and permittivity of greases, was identified as an important parameter [1; 2; 3; 4]. Recommendations have been made on how these properties can be investigated, not just with specialty rolling bearing test rigs, but also with comparatively simple laboratory methods. In this case, a cylinder capacitor was employed to investigate grease as a dielectric. A corresponding standard method is being developed through the activities of the DIN committee NA 062-06-53 AA (project M DIN 51111).

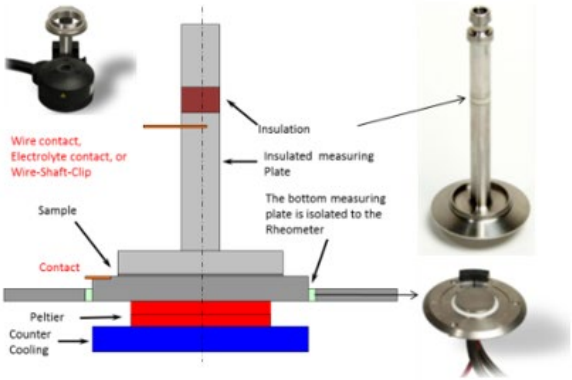

Figure 1: Setup of the DRD measurement system: electrifiable plate/plate measurement geometry[a]) and impedance spectrometer
(a) Copyright by Anton Paar Germany GmbH, reproduced by kind permission of Anton Paar Germany GmbH)

In addition, the dielectro-rheological device (DRD) offers another possibility for the investigation of lubricants, in particular greases. The DRD combines the measurement setup of a conventional rotational and oscillating rheometer with that of an impedance spectrometer and allows one to simultaneously collect rheological and dielectric measurement data. Therefore, greases can be characterized both with and without shearing in an electric field. Using the example of various oils and greases (model and fully formulated), experimental possibilities of the DRD are described. Partial comparison tests with conductive rolling bearings in the GESA test setup from FVA 650 II were also conductive to check validity of the methodology. These were limited primarily to impedance measurements, even though measurement of electrical conductivity and capacity is possible.

2. Experimental

A plate/plate measurement geometry (PP25) for the rheometer was employed in combination with an impedance spectrometer (LCR meter) for this DRD setup

(see figure 1). An electric potential is applied across a sliding contact on the shaft of the rotating plate as well as on the lower measurement plate to the lubricant being measured. AC and DC measurements can be done in a frequency range of 20Hz to 2MHz on current and voltage as well as phase angle. Measurements are possible in a temperature range of -40 to 200°C with variable shear stress. In addition to the DC resistance, measurement of the impedance $|\underline{Z}|$ (AC resistance) is possible due to the simultaneous measurement of the phase shift between current and voltage.

Most lubricating oils and greases yield a purely dipolar behaviour, i.e. show no ohmic conductivity. Therefore, they can be described in an AC circuit due to their purely capacitive conductivity as a simple capacitor:

$$|\underline{Z}| = \frac{1}{\omega C} = \frac{1}{2\pi f \varepsilon_r C_0} \qquad \varphi = -90° \qquad \textit{(Eq. 1)}$$

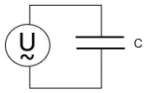

With a double logarithmic plot (Bode representation) of the impedance $|\underline{Z}|$ over the frequency f, a straight line is yielded. In the case of $|\underline{Z}|$ vs. 1/f vs. a straight line is also yielded, the slope of which can be used to determine the relative permittivity (dielectricity) ε_r (see figure 2).

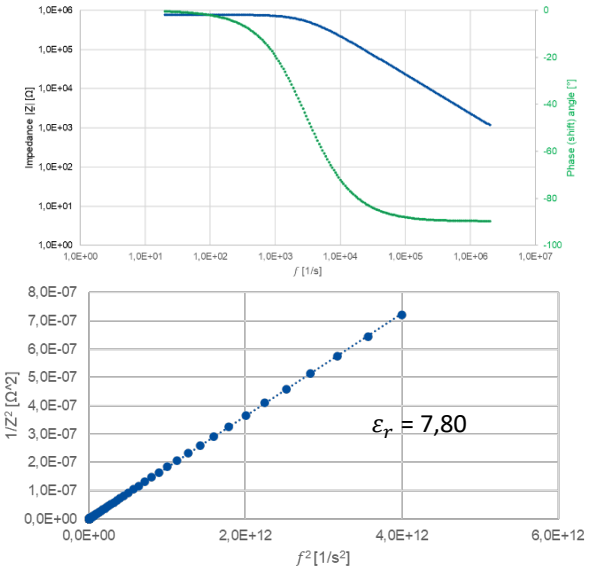

Figure 2: Impedance plots of a mineral oil (DRD without shearing, PP25 – 0,5mm, 1V AC, 25°C)

Some lubricants display ohmic conductivity via additional charge carrying (eg. via ionic components). One can describe this using an equivalent parallel circuit diagram of ohmic resistance and of the respective capacitor.

$$\frac{1}{|\underline{Z}|^2} = \frac{1}{\left(\frac{1}{\omega C}\right)^2} + \frac{1}{R^2} = (2\pi f \varepsilon_r C_0)^2 v + \frac{1}{R^2}$$

$$\varphi = -90 \; bis \; 0° \qquad \textit{(Eq. 2)}$$

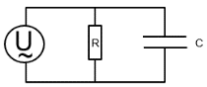

Using the form of 1/Z2 vs. f2, a straight-line result, from whose slope one can also determine ε_r (see figure 3). Additionally, the ohmic resistance R can be determined, either in relation to the Y-component of the line or over the impedance at phase angle = 0. At that point, $Z \approx R$. With respect to $Z = R+iX$, R is the real element (effective resistance) and X the reactance (capacitance).

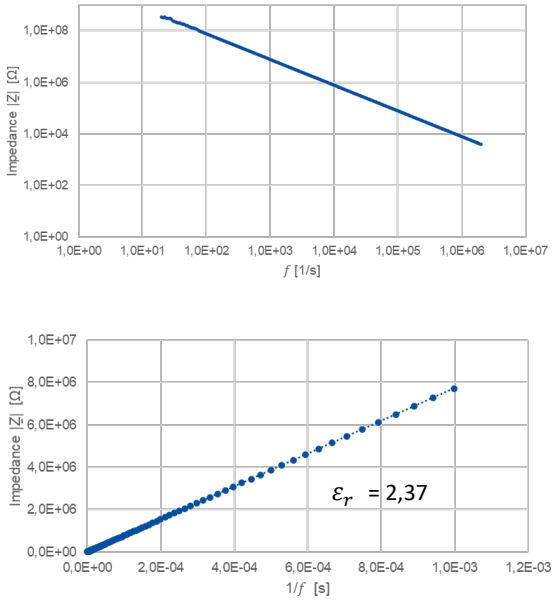

Figure 3: Impedance curves and phase angle of a polyglycol, (without shearing, PP25 - 0,5mm, 1V AC, 25°C)

3. Results and discussion

Similar to the case of oils, one can differentiate between capacitive and ohmic behaviour of greases. The measurement examples below show in the case of round robin test greases from DIN 51111 the difference between a non-conductive grease (F56) and a conductive polyglycol-grease (F55). Precision was verified at 3 different temperatures and comparative tests between laboratories at Robert Bosch and Fuchs Lubricants Germany, with comparison of impedance $|\underline{Z}|$ and phase angle φ (see figure 4).

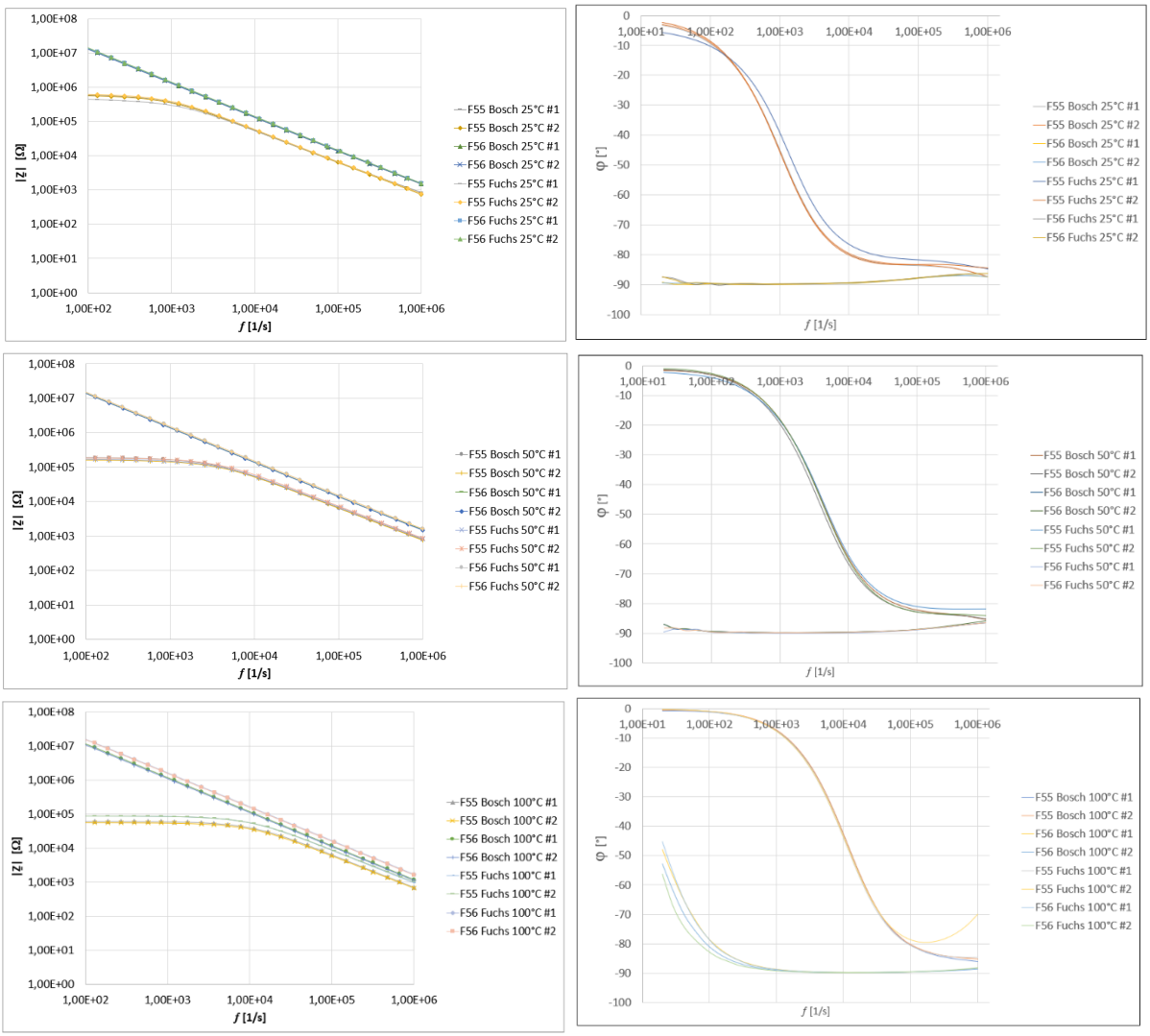

Figure 4: Impedance and phase angle curves of two laboratories (without shearing, PP25 - 0,1mm, 1V AC, 25 / 50 / 100°C); F55: Li-grease/mineral oil / F56: Li-complex grease/Polyglycol (Copyright by Lehrstuhl für Maschinenelemente, Getriebe und Tribologie (MEGT), University Kaiserslautern, reproduced by kind permission of Lehrstuhl für Maschinenelemente, Getriebe und Tribologie (MEGT))

The curves in figure 4 show that good to very good repeatability/comparability can be achieved with the DRD in two different laboratories with respect to the impedance and phase angle over a wide temperature range. This may be due to the fact that it is possible to control temperature to a fine degree with modern rotational rheometers, and in contrast to cylindrical capacitors, it is possible to eliminate virtually any air inclusions (see M DIN 51111). Only in the case of F55 Fuchs 100°C #2 was there a slight deviation in the phase angle at higher frequency, which may be due to inductive effects or feedback in the measurement system. In additional experiments, rotational tests at various temperatures were conducted to investigate the impedance behaviour of two greases, one with a powder additive (soot) and the other with ionic liquid (see figure 5). In the upper part of figure 5, measured shear viscosities are given at approximate shear rates of 100, 200 and 400s-1, determined over a period of 1 minute and temperature of 50°C. In contrast to usual measurement practices, eg. acc. to DIN 51810-1, only a planar measurement plate can be used, not conic or curved.

The shear rate can only be assumed to be an averaged value because the shear gradient is not constant over the entire span of the 25mm wide gap. Therefore, results are with respect to the maximum shear rate, which occurs at the very edge of the plate. As expected, both greases show structurally viscous behaviour at first, i.e. the viscosity decreases with increasing shear rate.

In the bottom diagrams, the impedance is given over the same test period at different shear rates. It is immediately recognizable that the levels of the measured impedances differ substantially. The grease with soot shows significantly higher conductivity, with an impedance that is less than that of the grease with ionic

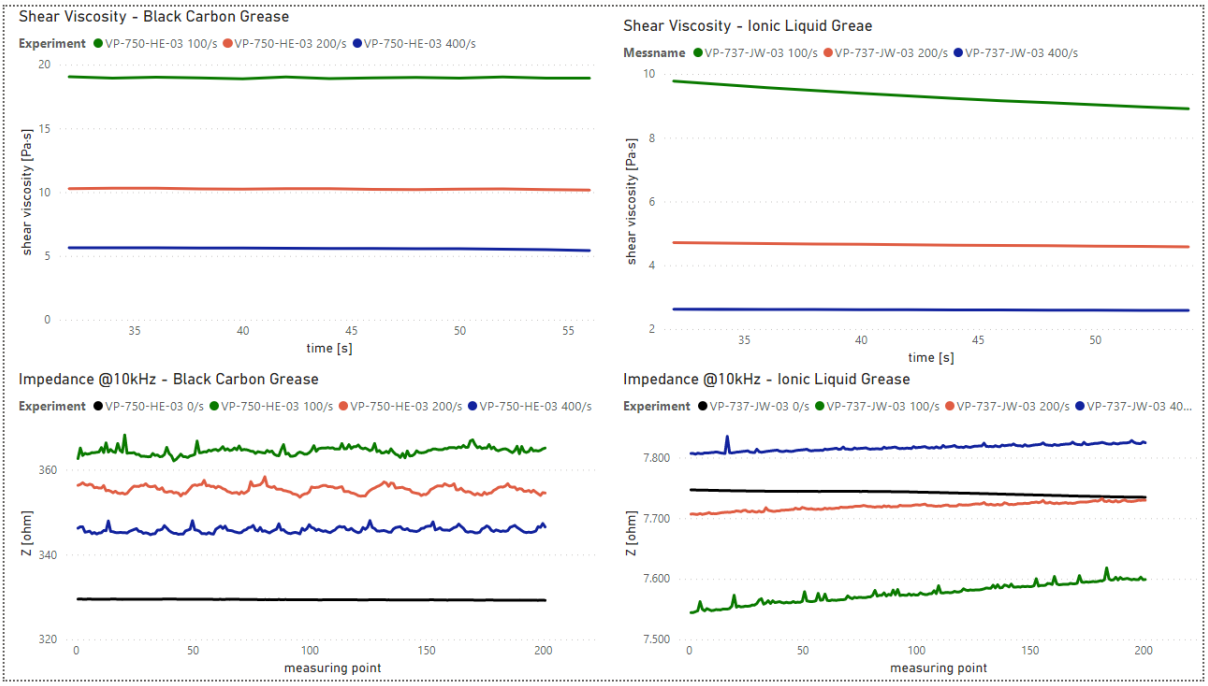

Figure 5: Impedance in dependence on shear rate (PP25 - 0,1mm, 1V AC, 50°C)

liquid by a factor of 20. Furthermore, approximately the same proportional deviation is observed for impedances over the range of 0 to 400s-1. This fluctuates in both cases by about 5% from 335 to 365Ohm in the grease with soot and 7500 to 7800Ohm in the grease with ionic liquid. An impedance maximum that is dependent on shear rate is also observed.

This occurs at 100s-1 for the grease with soot and 400s-1 for the grease with ionic liquid

Figure 6 shows an additional experimental possibility of the DRD: the time-dependent behaviour of impedance at a temperature of 80°C is presented. In an endurance test up to 960 minutes (16 hours), it was observed that the grease with ionic liquid yielded an even greater impedance, i.e. reduction of conductivity.

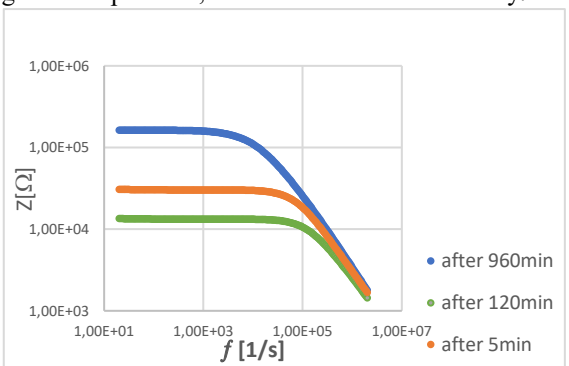

Figure 6: Dependence of the impedance on the tempering time in a grease with ionic liquid (Shear rate 50 s-1, PP25 - 0,1mm, 1V AC, 80°C)

One disadvantage of the DRD setup is that the plate gap of 0.1mm should not be reduced in order to avoid a short circuiting and to be able to maintain defined test parameters. Therefore, electrical behaviour of lubricants can only be observed in comparatively large lubricant films. As a result of these contact conditions, the influence of very thin lubricant films or tribofilms cannot be directly represented by this measurement system. Therefore, DRD impedance curves of oils and greases were compared to those from the GESA rolling bearing test setup at MEGT / University of Kaiserslautern (axial deep groove ball bearing 51208). An extensive description of the GESA rolling bearing test setup is given in the final report of FVA 650 II [2]. In figure 7, the most notable differences between the experimental setups of DRD and GESA are described. Subsequently, figures 8 to 10 describe experiments on various lubricating oils and greases with these test rigs. All DRD tests were carried out at 40°C, while GESA tests could only be controlled within a range of 38 to 47°C (steady state temperature in the bearing).

Figure 7: Comparison of DRD and GESA test parameters (b) Copyright by Lehrstuhl für Maschinenelemente, Getriebe und Tribologie (MEGT), University Kaiserslautern, reproduced by kind permission of Lehrstuhl für Maschinenelemente, Getriebe und Tribologie (MEGT)

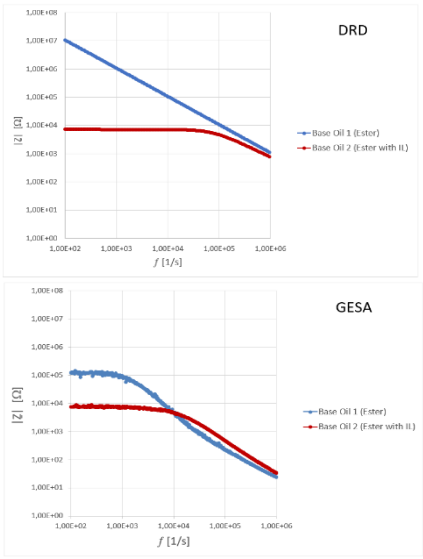

Figure 8: Comparison of the DRD (without shearing) and GESA impedance curves from two ester-based lubricating grease base oils with and without ionic liquid (IL)

Figure 8 describes the comparison between an ester-based grease base oil with and without ionic liquid (IL), both with the same additive formulations. In the DRD, only the fluid with IL showed a clear ohmic behaviour, while both showed this in the rolling bearing test at low frequencies, even when the impedance of the oil with IL was approximately 100000Ohm lower than the comparative oil without IL.

In figure 9, a comparison of DRD and GESA using easter-based polyurea greases (PU) is given in the form as they are implemented in electric motors. For these experiments, greases 1 and 2 have the same ester, additives and in the case of grease 2, same IL as in the previously described experiments from figure 7.

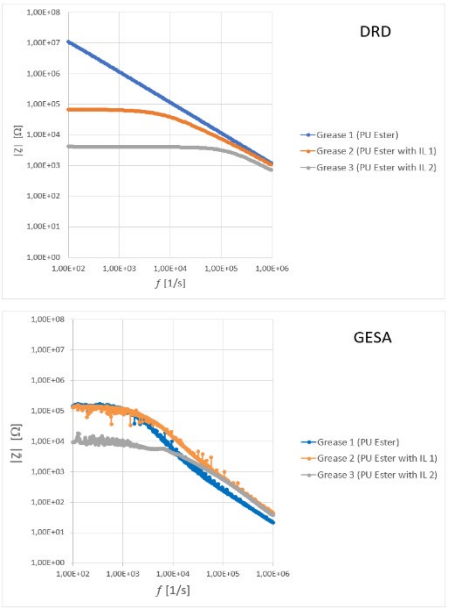

Figure 9: Comparison of DRD (without shearing) and GESA impedance curves from ester-based lubricating polyurea greases with 2 different ionic liquids and without ionic liquid.

Grease 3 is similar to grease 2 but contains a better, more conductive IL. Initially, DRD tests yielded impedances that could be very easily differentiated. However, in the GESA tests, only small differences were observed between greases 1 and 2, and a conductivity-

inducing effect of the IL was not observed in grease 2. In contrast, grease 3 showed a significantly lower impedance in the GESA test on the level observed in DRD testing.

In figure 10, additional DRD and GESA grease comparisons are given using PAO-based PU-greases. In the previous greases, ohmic partitions could be observed due to the polar character of the base oils and possibly residual moisture. The PAO-based greases, however, showed a purely capacitive behaviour. This was not the case in the GESA tests, which indicates that in contrast to the "thick lubricating films" in the DRD, other effects can occur in the rolling bearing. Not only could the conductivity of the triboreactive film play a significant role, but also how well the grease yields oil from its matrix and the distribution thereof in the raceway of the bearing. Temporary deficient lubrication could lead to an interruption of the lubricating film and solid-solid contact could occur, which could lead to partial occurrence of electrical short circuiting. This may explain the comparatively erratic GESA impedance curves for the PAO-based greases, as observed in figure 10.

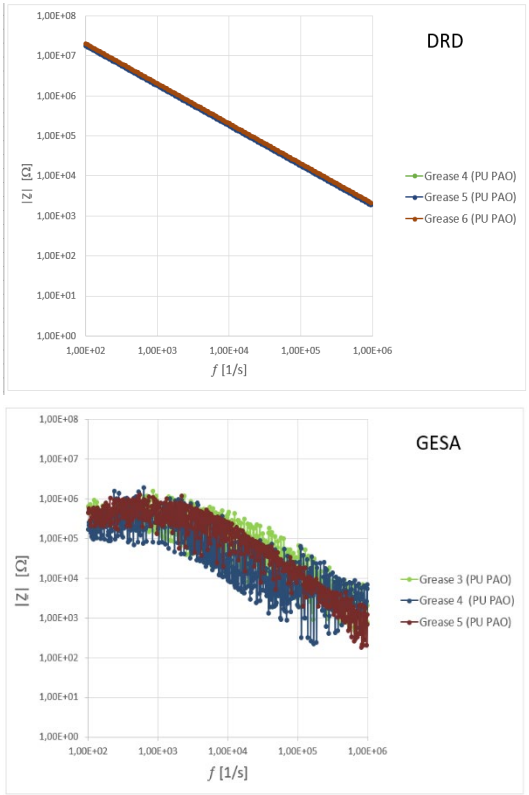

Figure 10: Comparison of the DRD (without shearing) and GESA impedance curves for different PAO-based greases

4. Conclusion

Similar to the case of oils, one can differentiate between The DRD offers researchers and developers of lubricating greases a multi-faceted measurement system that can be used to investigate the dielectric properties of lubricating oils and greases over a large temperature range. Moreover, this can be investigated at defined shear stresses or shear rates, or under time-dependent constraints, and deliver new findings on the effectiveness of conductivity-improving additives. A particular advantage in the testing of greases is that the plate geometry is very good at eliminating air inclusions in the measurement gap, and that the gap itself can be defined and tempered very precisely. This results in very reproducible and comparable measurement results. It would, therefore, be prudent to consider this measurement method for the development and quality control of lubricants as part of a wider standard, also because many lubricant manufacturers already work with modern rotational rheometers that could very easily be modified with the DRD setup. Due to the small sample requirement of approx. 0.5g, it is also possible to measure the electrical properties of many used lubricant samples that may be difficult to come by in great quantities in the field. This may help to draw conclusions on the operational behaviour of lubricants in electric motors or generators.

One disadvantage of the DRD is that a minimum plate gap of 0.1mm is required, which is a comparatively thick lubricant film. This makes it difficult to draw comparisons to electrical behaviour that is influence by reactive tribofilms from the lubricant chemistry. Such investigations can only be conducted in other tribometers or rolling bearing test rigs that allow for electrifiable rig components.

Acknowledgment

The authors thank Dr. Markus Matzke for comparison DRD measurements in the grease laboratory of Bosch GmbH in Renningen, Dr. Dani Bechev, Lubricant Consult GmbH for the provision of round robin test greases F55 and F56 from AA 653, as well as Resat Capan for tests on the GESA rig at the Lehrstuhl für Maschinenelemente und Getriebetechnik (MEGT) of the University of Kaiserslautern.

References

[1] [1]. Radnai, TU Kaiserslauterm, Gmeinder, TH Darmstadt. *Schädlicher Stromdurchgang.* 2013.

[2] [2]. Bechev, Weickert. *FVA 650 II Abschlussbericht.* 2020.

[3] [3]. Bechev. *Prüfmethodik zur Charakterisierung der elektrischen Eigenschaften von Wälzlagerschmierstoffen. Dissertation, Technische Universität Kaiserslautern.* 2020.

[4] [4]. Radnai, TU Kaiserslautern, Gmeinder, TH Darmstadt. *FVA 650 I Abschlussbericht. 2015.*

Application of the Generalized Bearing Life Model for Especial Surface Heat Treatment of Rolling Bearings – Case of Wind Turbine Gearbox

Liang GUO[1], Hugo BOFFY[2], David VAES[3], Guillermo E. Morales-Espejel[1,4]

[1] *SKF Research and Technology Development, liang.guo@skf.com*

[2] *KaM Performance Prediction, SKF Technology Development, hugo.boffy@skf.com*

[3] *SKF Wind Gearbox Competence Centre, david.vaes@skf.com*

[4] *Université de Lyon, INSA-Lyon CNRS, LaMCoS, guillermo.morales@skf.com*

Abstract– Wind gearbox manufacturers are maximising the torque density of new multi-megawatt gearboxes to support the wind industry to reduce the cost of energy. This requires for component suppliers, such as the bearing manufacturers, new solutions to allow the downsizing of the gearbox design. SKF, therefore, has developed the SKF DuraPro for wind turbine gearboxes in which a tailored steel and heat treatment is adopted resulting in a significant surface and subsurface life increase. The tailored steel and heat treatment results in a fine microstructure, increased surface hardness, tailored retained austenite level and compressive residual stresses. These add a higher strength to the material at the very surface to withstand marginal lubrication conditions or particle contaminations and also increase the subsurface fatigue strength. The generalized bearing life model (GBLM) developed before and up to now only applied to hybrid bearings is further developed to be applied in the calculation of the rating life of the new designed bearings due to its capability to separate surface and subsurface survival. Hence capable of capturing the added benefits to this bearing design, meant to survive successfully the tougher operating conditions in gearboxes of wind turbines. The GBLM life predictions are validated by comparison with the bearing endurance testing.

Keywords – Wind turbine gearbox, SKF DuraPro for wind turbine gearboxes, Bearing life, GBLM

1. Introduction

Wind power generation, which converts the wind's kinetic energy into electricity without causing serious environmental damage, is regarded as one of the most promising distributed energy sources. To stay competitive both onshore and offshore with traditional energy sources and other renewable energy such as solar PV systems, it is necessary to further reduce the Levelized Cost of Energy (LCoE) of wind turbines. The continuous market pressure on LCoE results in new design concepts at the wind turbine level and the design of the main components, such as gearboxes. Increasing gearbox torque density to 200 Nm/kg and beyond is required to limit the weight uptower and limit the size of the largest components for transportation. All components, including roller bearings, are therefore pushed to the limits and new solutions are required to further downsize without jeopardizing the field performance.

State-of-the-art gearboxes for larger wind turbines are designed with 3 or more planetary stages. Planetary stages are equipped with multiple planets to limit the size of ring gear as it influences the overall size and weight of the gearbox. These new design trends result in a significant reduction in gearbox size. However, it also results in smaller planetary gears and less space for the bearing supporting the planets. Therefore, new rolling bearing solutions are needed, capable of taking higher loads and contact pressures to support the downsizing and torque density increase. Another important driver to develop new roller bearing solutions for wind turbine gearboxes is the reliability in the field and robustness against typical failure modes in the field such as premature failures with White Etching Cracks [1] or micro pitting and wear [2], which are relevant to increasing the reliability of new gearbox designs as well as improving the robustness of turbines in the field.

To satisfy the requirement of the new wind turbine gearbox design, SKF has therefore developed the SKF DuraPro for wind turbine gearboxes resulting in a significant surface and subsurface life increase. A tailored steel and heat treatment is adopted in the design of the new gearbox bearings. The tailored steel and heat treatment results for example in a fine microstructure, increased surface hardness, tailored retained austenite level and compressive residual stresses which add a higher strength to the material, at the surface and below where the highest stresses are present, to withstand marginal lubrication conditions or indentations and to achieve a subsurface fatigue strength increase. At present time only one bearing life model (GBLM) [3] is known to be flexible enough to separate surface and subsurface survival. Thus, it can capture the added benefits to this bearing design, to survive successfully the tougher operating conditions in gearboxes of wind turbines. Therefore, the generalized bearing life model (GBLM) is now adapted and applied in the calculation of the rating life of the SKF DuraPro gearbox bearings.

In this paper, the proposed solution (SKF DuraPro for wind turbine gearboxes) will be briefly described. Then a short summary of the GBLM bearing life method will be discussed. The validation of the model requires endurance testing, thus the performed tests will be also described alongside the model predictions.

2. The SKF DuraPro for Wind Turbine Gearboxes

The performance of a rolling bearing is, besides the design and required tolerances, dependent on material parameters such as microstructure, residual stress and hardness. In turn, the selection of steel alloy and heat treatment process is heavily affecting all these parameters. SKF has developed a special steel and heat treatment process to meet the increased demands of rolling bearings in wind turbine gearboxes.

The material of the SKF DuraPro gearbox bearings is based on a selected carburising steel grade specified in ISO 683-17 in combination with a thermochemical heat treatment process enriching the surface layer of the bearing components. The enhancement of the surface layer leads to a refined microstructure, characterized by tiny precipitates and a carefully controlled amount of stable retained austenite. These attributes are widely acknowledged for their beneficial impact on the fatigue endurance of bearing steel, encompassing resistance against failure originating from the surface as well as its subsequent propagation. The surface enrichment additionally induces significant compressive stresses within the surface layer and a higher surface hardness compared to the bearings currently employed in wind turbine gearboxes. This further enhances the resistance of the SKF DuraPro gearbox bearings to fatigue caused by rolling contact. Moreover, the combination of increased hardness, compressive residual stresses, fine microstructure increases the robustness against premature failures as seen in wind turbine gearboxes.

Figure 1 shows the hardness profile of the SKF DuraPro gearbox bearings. After the special heat treatment, the hardness in the surface layer is improved significantly and it decreases to the hardness of the base material into the depth.

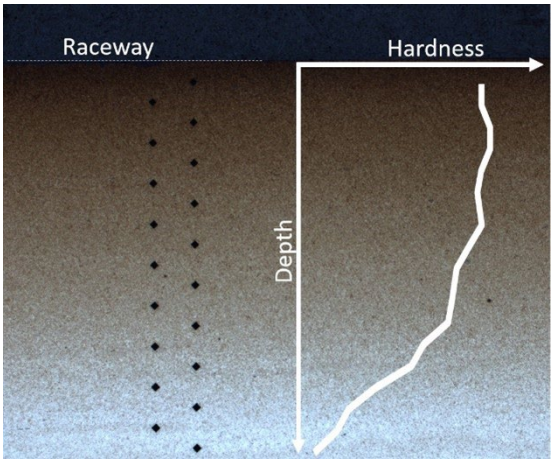

Figure 1: Change of the hardness of the studied bearing from raceway to subsurface, the black points on the left are the location of hardness measurement

3. Generalized Bearing Life Model (GBLM)

As discussed, the new steel and heat treatment technology improves the bearings‘ surface and subsurface fatigue simultaneously. To describe their contribution to the enhancement of bearing life, the GBLM model which can consider the surface and subsurface fatigue separately is adopted to predict such bearing life. Up to now the estimation of rolling bearing life has been based on engineering models that consider equivalent stress, originating beneath the contact surface which is applied to the stressed volume of the rolling contact. The surface-initiated failures, resulting from contamination or poor lubrication, have been included in the bearing life estimation by applying a penalty factor to the overall equivalent stress of the rolling contact [4]. In the GBLM, however, this issue is addressed in a general approach in which the surface-originated damages are explicitly formulated into the basic fatigue equations of rolling contact. Depending on the working conditions and surface damage modes, different physical surface damage models can be integrated into the bearing life formulation. This new formulation gives the power to better represent the tribology of rolling bearings in rating life calculations. Besides, it also gives a better knowledge of the surface endurance that dominates the field performance of rolling bearings. The schematic view of the GBLM idea is represented in Fig. 2.

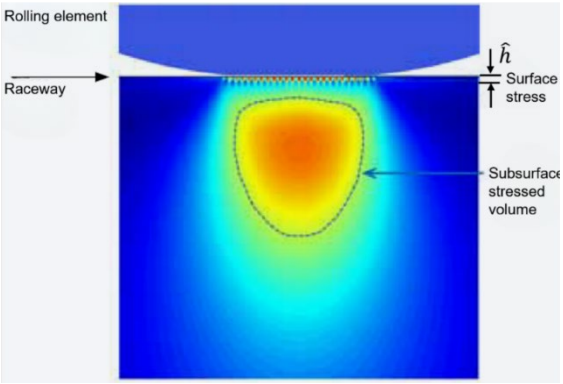

Figure 2: Separation of surface and subsurface as proposed by the GBLM

The Generalized Bearing Life Model (GBLM) was first communicated to the public in a scientific paper where the fundamental theory is described [3]. Later the model was applied to hybrid bearings in [5]. From [3] the basic bearing GBLM life equation in its integral form and with a general stress criterion σ is:

$$L_{10} = \frac{\left[\ln\left(\frac{1}{0.9}\right)\right]^{\frac{1}{e}}}{u}\left[\underbrace{\bar{A}\int_{V_v}\frac{\langle\sigma_v - \sigma_{u.v}\rangle^c}{z^h}dV_v}_{Subsurface} + \underbrace{\bar{B}\int_{A}\langle\sigma_s - \sigma_{u.s}\rangle^c dA}_{Surface}\right]^{-\frac{1}{e}} \quad (1)$$

where L_{10} is bearing life rating with 90% reliability, u is the number of stress cycles per revolution, $\bar{A}$ and $\bar{B}$ are damage integral constant for the volume and the surface, V_v and A are the integration volume and surface integration area, σ_v and σ_s are the fatigue generating stress in the volume and on the surface, $\sigma_{u.v}$ and $\sigma_{u.s}$ are the fatigue limit in the calculation of subsurface and surface life.

As shown in equation (1), the subsurface rolling contact fatigue is treated following the classic model of Ioannides and Harris [6], the surface damage function can be obtained [7] and the surface fatigue can be included in the integral form, as shown in equation (1). But also in a fast calculation manner using curve-fitted function as described in [3, 5] for which the constants $c_1 \ldots . c_5$ (equation (2)) of this integral depend on the load and the environmental factor $\eta_{env} = \eta_{lub}\eta_{cont}$, with $0 \leq \eta_{env} \leq 1$. For which 0 means very poor lubrication and contamination conditions and 1 means good lubrication quality and clean conditions. As indicated in the schematic Fig. 3.

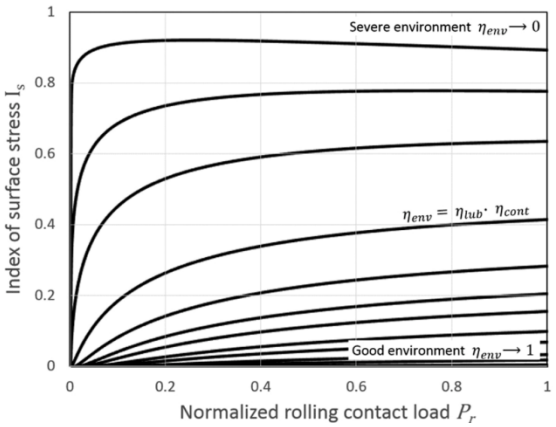

Figure 3: Normalized index of surface stress for surface performance, derived from equation (2)

$$I_s^* = \bar{B}\int_A \langle\sigma_s - \sigma_{u.s}\rangle^c dA \approx c_1 \exp\left[\frac{c_2}{\left(\frac{P}{P_u}\right)^{c_3}} + \frac{c_4}{\left(\frac{P}{P_u}\right)^{c_5}}\right] \quad (2)$$

The treatment of the surface life needs advanced tribological models [8] to assess the surface integral and derive the missing constants, in which the physical interactions that occur in Hertzian contacts, such as friction, wear, fatigue, lubrication and running-in can be addressed. Therefore, the tailored steel and heat treatment which modifies the performance of the SKF DuraPro for wind gearboxes can be reflected in the bearing life predictions. Furthermore, when needed, the surface and subsurface parameters are adjusted via results from endurance testing. Another advantage of separating surface from subsurface is that it is possible to compare the damage integrals, producing a measure of the stress on the surface in comparison with the subsurface [3]. A new parameter RSF is defined, as shown in Equation (3) shown.

RSF (relative surface fatigue indicator), is a parameter that is defined either in the whole contact or using slices or lamina. This parameter can vary as $0 \leq RSF \leq 1$. When $RSF \rightarrow 1$ most of the accumulated fatigue is taken by the surface (low environmental factor). On the contrary, when $RSF \rightarrow 0$ is the subsurface that takes most of the fatigue (high environmental factor). This factor gives engineers a good indication of where to increase or reduce safety.

$$RSF = \frac{\bar{B}\int_A \langle \sigma_s - \sigma_{u.s}\rangle^c dA}{\bar{A}\int_{V_v} \frac{\langle \sigma_v - \sigma_{u.v}\rangle^c}{z^h} dV_v + \bar{B}\int_A \langle \sigma_s - \sigma_{u.s}\rangle^c dA} \quad (3)$$

4. Bearing Life Tests and Model Validation

The validation of performance factors for the new bearing solution requires enough tests to ensure enough accuracy. To obtain those data, an endurance testing campaign has been executed focusing on both surface and subsurface performances. Very high load, pre-dented raceway (inner ring), full-film and reduced lubrication conditions have been addressed to cover a wide range of application conditions. In the surface performance tests, all inner rings (IR) of the bearings were pre-dented with 8 indents, which are evenly distributed on the inner ring raceway. In the preparation of the dents, a tungsten carbide ball is used as the indenter and the same indenter load is applied to all test variants. Figure 4 shows a typical dent and a measured dent profile. The pre-dents are acting like local stress raisers draining away the lubricant from the local contact. As a result, metal-to-metal contact occurs at the border of the indents. The corresponding testing parameters are addressed in Table 1.

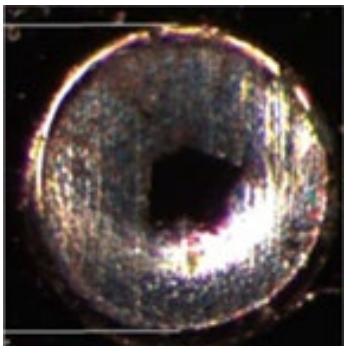

(a) One pre-dent

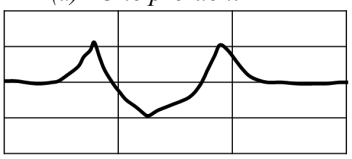

(b) Pre-dent profile

Figure 4: One typical pre-dent on inner ring raceway (a) and a typical measured pre-dent profile (b)

Table 1 Testing conditions in terms of load (C/P) and lubrication (kappa) conditions

	Reduced lubrication	Full film
C/P	1.3	1.0
Kappa	1.7	3.1
Other	Pre-dented raceway	-

The tests have been performed with medium size tapered roller bearings (150 mm bore diameter) as used today on the high-speed shaft of wind turbine gearboxes of the 2 and 3 MW range to make the endurance tests as representative as possible. Two bearing variants have been tested under the same conditions: the baseline is a state-of-the-art high carbon through-hardened bearing, including Explorer [9] features and black oxide coating as used today in wind gearboxes. This baseline is compared with a variant which has the inner ring with the tailored steel and heat treatment of the SKF DuraPro for wind turbine gearboxes. This allows a fair comparison between them and the possibility to provide the customer with a clear picture of the enhanced performance provided by the new technique. The endurance tests have been performed on self-developed bearing life test rigs, as shown in Fig. 5. Figure 6 illustrates the schematic setup of one test head of the test rig. There are two test bearings in one test head and they are mounted in an X-arrangement, as the red line shown in Fig. 6. The axial load can be applied on the two bearings by a hydraulic cylinder. The lubricant is injected from both sides of the bearings and exits the test head between the bearings. During the test, the temperature is controlled to achieve a defined lubrication process. The test rig is shut down when a bearing failure is detected by a vibration, friction torque or temperature sensor. After the test, the failed bearings are inspected carefully.

All endurance testing results have been pooled following [10] on a single normalized Weibull chart presented in Fig. 7. The pooling is done here to improve the statistics and the full-film results have been scaled down to the reduced lubrication conditions. This figure highlights the significant performance increase of the new solution versus the existing one with strong statistical significance. In specific, the L_{10} life of the SKF DuraPro gearbox bearings is around 4.5 times longer than current wind turbine gearbox bearings. Moreover, investigation of the failed bearings after the test has shown that the failure has moved from the inner ring, which failed most in the baseline tests due to the higher contact stresses at the position of the pre-dents, to the outer ring and rollers in the tests using the improved inner ring. The outer ring and rollers in the tests were still through hardened high-carbon steels. Figure 8 illustrates some failure examples of the test bearings, none of the improved inner rings failed in the tests. This indicates that there is even further potential to increase the endurance life by applying this tailored steel and heat treatment to all components. The “star” in Fig.7 shows the GBLM predicted life of the SKF DuraPro gearbox bearings. The model predicted life value is close to the lower limit of the confidence interval of the L_{10} of the test, indicating the validity and safety of the developed calculation [10].

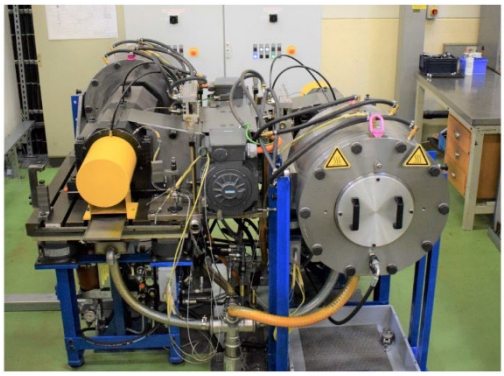

Figure 5: The bearing life test rig used in this study

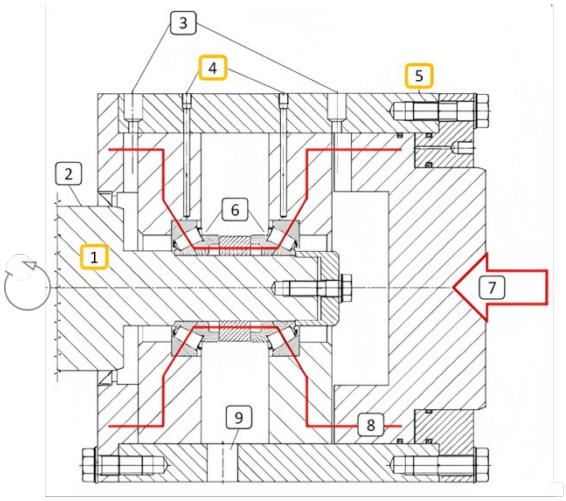

1-Torque Measurement. 2-Speed Measurement. 3-Oil Inlet.
4-Temperature Sensors. 5-Vibration Sensor. 6-Test Bearings.
7-Axial Load. 8-Load Line. 9-Oil Outlet. ☐-Failure Detection.

Figure 6: Schematic setup of the test head

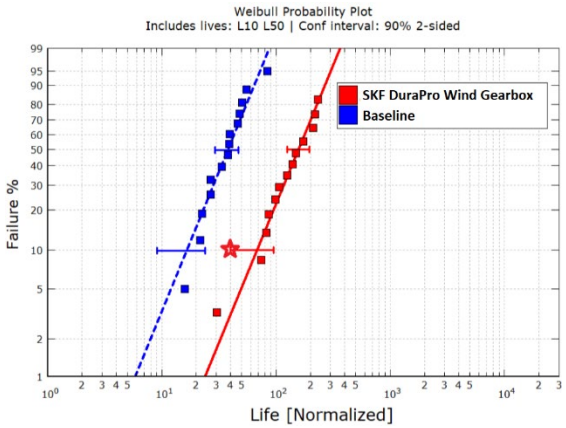

Figure 7: Pooled and normalized test results alongside the model predictions

To further investigate the performance of the new bearing design, parameter studies were conducted using the developed GBLM model and some results are shown in Figure 9. The same bearing adopted in the life test was studied here (150 mm bore diameter). Under the two contamination conditions (*etaC*=0.3 and *etaC* =0.5), the life ratio (the ratio of the GBLM life of the new bearing to the life of bearings used today in wind turbine gearboxes) is equal to or higher than 4 in the whole kappa range. Especially the bearing performance is increased more significantly under poor lubrication conditions (kappa <1), indicating the tailored steel and heat treatment adopted here can improve the bearing performance under severe working conditions. Besides, the failures should mainly be surface-initiated driven (RSF>0.5) under the current working conditions. Furthermore, compared with the relative mild contamination condition (*etaC* =0.5, Fig. 9(a)), more surface-initiated failures should appear when *etaC* is reduced to 0.3 since its RSF is higher in the whole kappa range (Fig. 9(b)). With the increase of film thickness or kappa, the possibility for more subsurface fatigue failures to appear increases, as the RSF is reduced, see the red curve in Fig. 9. This behaviour is reasonable to expect since the higher film thickness decreases the stresses at the surface, leading the drop of surface-initiated fatigue or damage.

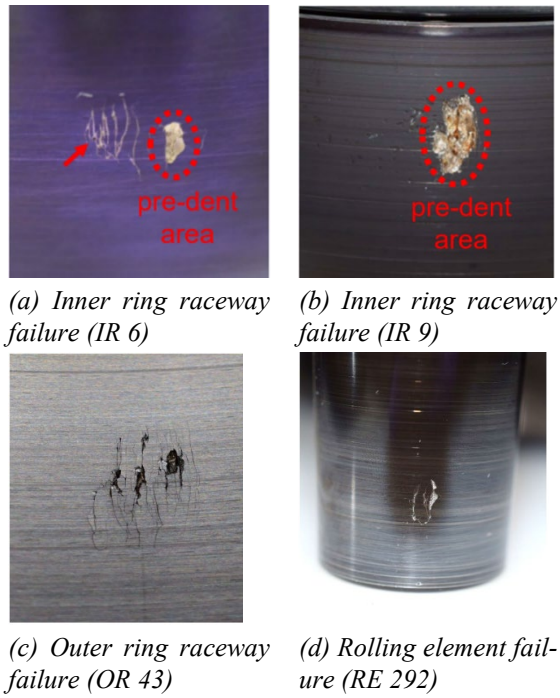

(a) Inner ring raceway failure (IR 6)

(b) Inner ring raceway failure (IR 9)

(c) Outer ring raceway failure (OR 43)

(d) Rolling element failure (RE 292)

Figure 8: Damage examples of the test bearings, (a) and (b) are baseline bearing failures, (c) and (d) are failures of the standard outer ring and roller in the SKF DuraPro gearbox bearings

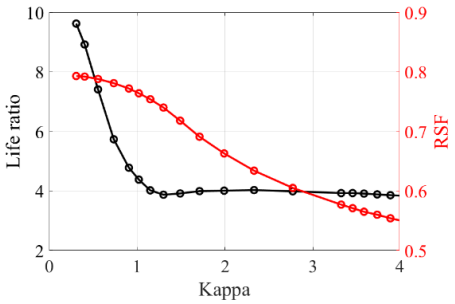

(a) etaC=0.5

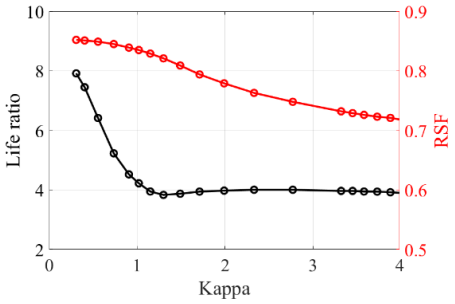

(b) etaC=0.3

Figure 9: Change of life ratio and RSF with Kappa (tapered roller bearings with 150 mm bore diameter, axial load=494 kN)

5. Conclusions

In this work the SKF DuraPro for wind turbine gearboxes, including a tailored steel and heat treatment, is proposed for high torque density wind turbine gearboxes. Bearings made with this design have been endurance tested alongside state-of-the-art baseline design. The results show the superior surface and subsurface performance of the new bearing design. This improvement can better be reflected with the GBLM life model which properly separates the surface from the subsurface survival. The model has been verified to correctly predict the testing results. From this the following conclusions can be drawn:

1. The new bearing design indeed reflects substantially better performance from harsh operating conditions as demonstrated by the endurance test results.
2. The SKF GBLM model can capture these added benefits in the bearing life prediction with calculated life that corresponds well with the bearing life test data.
3. The proposed solution package of new bearing design and calculation method is likely to become an answer for the increasing demand in torque density experienced in modern wind turbine gearbox applications.

Acknowledgment

The authors thank SKF for the permission to publish this paper.

Reference

[1] Stadler K, Vegter RH, Vaes D. White etching cracks - a consequence, not a root cause of bearing failure. SKF Evolution; 2018.

[2] Morales G, Brizmer V. Understanding and preventing surface distress. SKF Evolution; 2011.

[3] Morales-Espejel GE, Gabelli A, de Vries AJC. A model for rolling bearing life with surface and subsurface survival—tribological effects. Tribol Trans 2015;58:894–906.

[4] Ioannides E, Bergling G, Gabelli A. An analytical formulation for the life of rolling bearings. Finnish Acad. of Technology; 1999.

[5] Gabelli A, Morales-Espejel GE. A model for hybrid bearing life with surface and subsurface survival. Wear 2019;422–423:223–34.

[6] Ioannides E, Harris TA. A new fatigue life model for rolling bearings. J Tribol 1985;107:367–77.

[7] Lubrecht AA, Jacobson BO, Ioannides E. Lundberg Palmgren revisited, Japan: Proc. Japan International Tribology Conference; 1990, p. 185–90.

[8] Morales-Espejel GE, Brizmer V. Micropitting modelling in rolling–sliding contacts: application to rolling bearings. Tribol Trans 2011;54:625–43.

[9] SKF Rolling Bearing Catalogue. 2018.

[10] Morales-Espejel GE, Gabelli A. Rolling bearing performance rating parameters: Review and engineering assessment. Proc Inst Mech Eng Part C J Mech Eng Sci 2020;234:3064–77.

Finite Elements modelling of edge imperfections in ceramic rollers for assessing the risk of fatigue failure

Yuri Kadin[1], Charlotte Vieillard[1], Jeroen Wensing[1], Anand Theerthan[1] and Manlio Becchetti[1]

[1] *SKF Research & Technology Development, Houten, The Netherlands*

Abstract – To ensure reliability of hybrid cylindrical roller bearings each ceramic roller is optically inspected, and scrapped if a surface imperfection above the critical size is detected. By this, the potential root cause of Rolling Contact Fatigue (RCF) failure is reduced. The rejection criterion is based on experimental and theoretical knowledge, which in the case of edge imperfection (at the roller chamfer) is currently missing. A special type of material imperfection, termed as Missing Material (appearing as result of imperfect sintering and/or surface machining), is studied in the current work. Based on the optical inspection of scrapped rollers (containing imperfections of relatively large size at chamfer) the morphology and the range of imperfection dimensions was identified, and transferred to Finite Elements model for the stress analysis. The criticality of imperfection was assessed by implementing the maximum tensile stress criterion, relating the size and the location of imperfection to the risk of RCF. In order to stay "on the safe side", extreme contact conditions (very high contact load and enormously high misalignment) were assumed for the current analysis, and even under these challenging consideration limited risk of fatigue failure was predicted.

Keywords – Ceramic rollers, Material imperfections, Rolling contact fatigue, Stress analysis

Introduction

Hybrid bearings overperform the regular (full steel) ones in multiple aspects, thanks to superior properties of silicon nitride (Si3N4) – the ceramic material used for rolling elements in hybrid bearings. Compared to the traditional bearing material – steel, Si3N4 is lighter (which is important in aerospace applications), has higher hardness (providing high wear resistance) and higher stiffness (beneficial in high precision bearings). Other properties of Si3N4 [1], like good resistance to corrosion, low thermal expansion and high electrical insulation make hybrid bearings attractive for many demanding applications. Ceramic components are not exposed to hydrogen embrittlement, while in steel components of bearings (see e.g. [2]) it can be a case. Finally, it was found that hybrid bearings perform better in contamination conditions [3], compared to the full steel bearings.

Nevertheless, Si3N4 ceramics are still less resistant to crack initiation and propagation, compared to steels. Pre-existing material imperfections can be present on surfaces of ceramic rolling elements, being the result of manufacturing (by sintering) and/or surface finishing processes. Since the reliable operation of hybrid bearings is strongly linked to the material quality of rolling elements, each ball or roller is inspected. This inspection aims to reject components, containing relatively large surface imperfections (features) which during bearing operation can lead to the progression of fatigue damage. Recent experimental and theoretical research conducted in SKF aimed to develop engineering criteria for the acceptance or rejection of imperfect rolling elements, based on the size and type of imperfection, material characteristics and bearing loading conditions. This research covered different types of imperfections, varying in terms of their morphology: C-cracks [4], Missing Material [5], Star [6], etc.

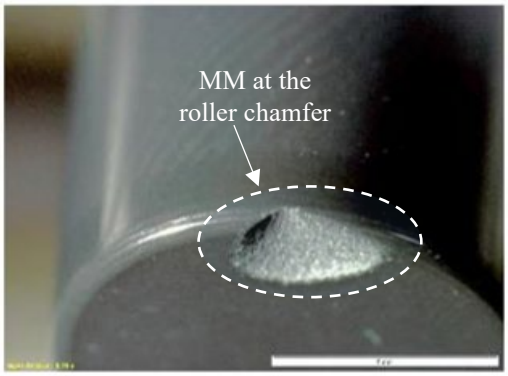

Figure 1: An example of scrapped roller.

It is important to note, that for ceramic rollers, the situation is more complex compared to balls, because in rollers the imperfection criticality is also dependent on its location. The imperfections located on the roller raceway are subjected to different loading conditions compared to ones at the edge (chamfer) or at the end face. Previous research (see [4-6]) was focused on the raceway, while less attention was given to the imperfections appearing beyond this zone. Nevertheless, the inspection criteria for the latter imperfections can be rather different than the one needed for the imperfections on the raceway.

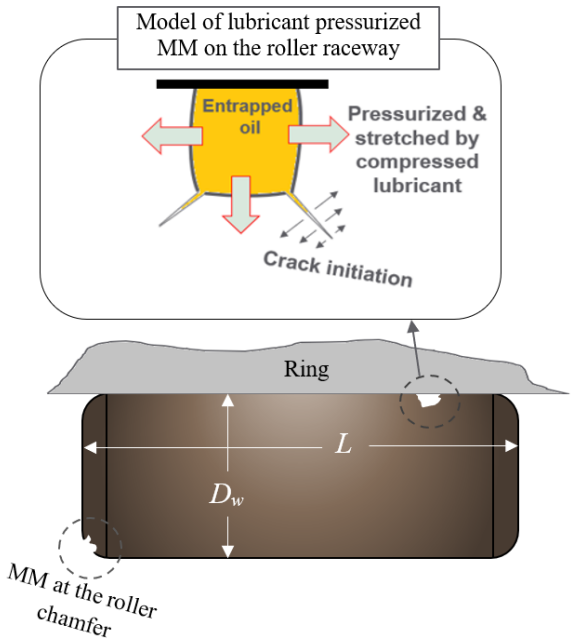

Figure 2: Failure mechanism associated with oil pressurization (originally proposed in [5]). Corresponds to the MMs located on raceway.

The current study is focused on a specific type of surface feature – the Missing Material (MM), appearing on balls and rollers as result of imperfect sintering and/or surface machining. This feature can appear either on the raceway (of a ceramic ball or roller) or at the roller edge, and the example for the MM at the chamfer zone is given in Fig. 1 (note, that due to relatively large size of imperfection, this roller was scrapped). The feature termed as MM, was previously studied experimentally and by Finite Element (FE) modelling [5], assuming that the main failure mechanism associated with MM is the entrapped and pressurized oil (see Fig. 2). According to [5], this mechanism is active when MM enters into the contact zone and the oil inside the MM gets pressurized. Eventually, this leads to tensile stresses around the defect and crack initiation. However, when MM is located out of the raceway (and is out of the contact) this mechanism can hardly be active. Hence it is reasonable to assume, that MMs located at the edge zones are less prone to fatigue failure. The current study aims to quantify these risks by means of FE modelling, which is probably the most suitable approach for this problem. Indeed, an experimental study in this case is challenging, because it requires producing artificial features of accurate preassigned geometry at the roller edge, assuring roller orientation versus load and controlling accurate bearing misalignment. On the other hand FE, allows to simulate numerically any contact conditions (accounting for the roller geometry and misalignment) and MMs of various morphologies.

Experimental study

To make FE modelling reasonable the MM dimensions (to be used as the input parameters for the model) have to be identified. Using stereo microscopy, the morphology of MMs in scrapped rollers was visualized to obtain their size and shape. Some images from this inspection are presented in Figs. 3 and 4.

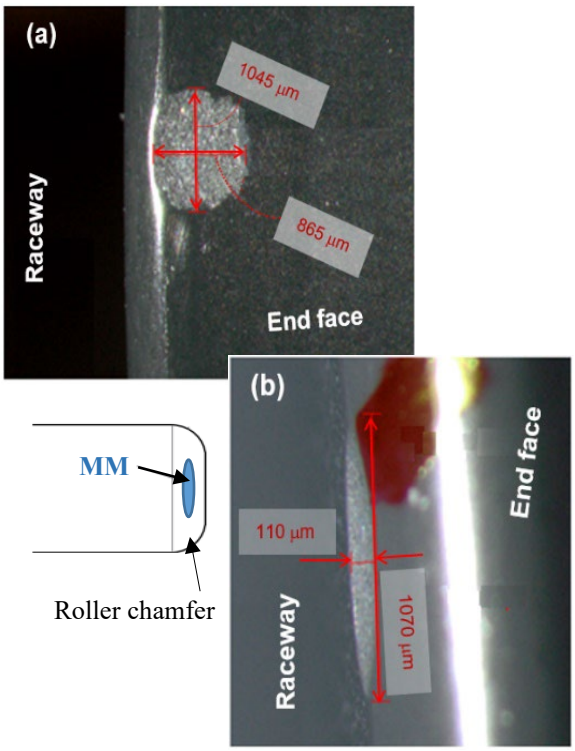

Figure 3: Morphology of approximately circular (a) and elongated (b) MMs, obtained by stereo microscopy.

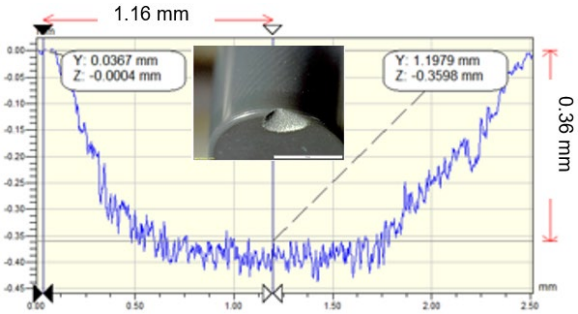

Figure 4: Profilometry for the identification of the MM depth.

The dimensions presented on the images of Fig. 3 indicate the length and the width of MM; the MM locations relative to the end face were also measured. As shown in Figs. 3 and 1, the features can reach large size (in some cases length exceeds 1 mm), and even though the oil pressurization effect is not active, the risk of fatigue failure can be rather high and should be assessed.

It is believed that as certain "idealization", an ellipsoidal shape can be assumed for the adequate FE modelling of MM geometry. Using white light interferometry, the profiles of the features were characterized (see Fig. 4), which is needed to identify the MM depth.

Modelling

The FE modelling in the current work, aims to evaluate the stress field in the vicinity of MM and by this to assess the risk of Rolling Contact Fatigue (RCF). In reality, a cylindrical roller has crowned geometry (see Fig. 5), thus the solution of "full" problem (intending to get proper numerical solution both at the contact zone and in the vicinity of imperfection) can become too expensive in terms of computational time. Hence, the contact problem and the stress field analysis (within reasonable accuracy) are split from each other, and treated separately. The contact pressure is evaluated semi-analytically, and is applied as the stress boundary conditions to the FE domain, which models the part of the roller containing an imperfection. In order to simulate over-rolling, the statically evaluated contact pressure is "animated". This is done by varying the contact zone position relatively to the domain origin in the FE pre-processor. It is important to note, that the current approach is based on the two assumptions:

i) The detailed geometry description of contacting bodies and their positioning relative to each other (radii of curvature, roller geometry, misalignment, etc.) are included only in the contact analysis, while the roller raceway in the FE model (stress filed analysis) is assumed flat.

ii) The semi-analytical solution of the contact problem is based on the half-space assumption, meaning that the details at the contact zone edge (chamfer, imperfection, etc.) have no influence on the pressure distribution.

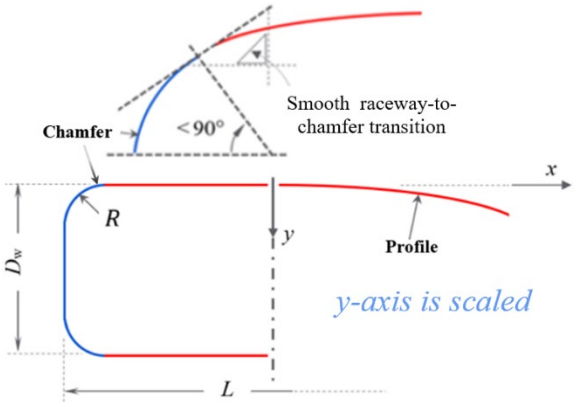

Figure 5: Schematic of a ceramic roller of the dimensions $D_w \times L$; R defines the chamfer curvature. The smooth transition (continuous first derivative) from raceway to the chamfer is assumed in the current contact pressure analysis.

The validity of the latter assumption was explored in [7], comparing the pressure distributions predicted by semi-analytical and FE solution. It should be noted, that MM of considerable size can cause some shock loads when it enters the contact, however this is out of the current work scope.

Contact pressure evaluation

The pressure formed at the contact between an inner ring and a roller is governed by the crowned geometry of the ceramic roller and the ring, which raceway length slightly exceeds the roller raceway. The contact pressure is evaluated semi-analytically by using the Green functions and the conjugate gradient method. The Green functions method is used to predict the stress and deformation state due to a concentrated force acting on an elastic half-space [8]. By integrating the Green functions, the surface deformation due to any contact pressure distribution can be evaluated, and this distribution is predicted by the numerical solution of an integral equation. Since the current contact problem is non-conformal, this integral equation is non-linear and is solved by using the conjugate gradient method [9].

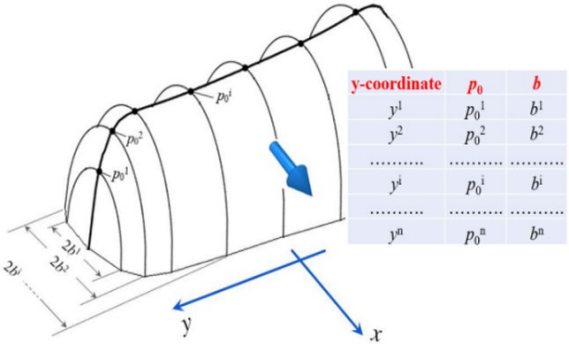

Figure 6: Schematic of the pressure distribution formed at the contact between a bearing ring and a roller, and discretised using the so-called slicing method. Note, that the current distribution is not symmetric with respect to the x-coordinate demonstrating the effect of misalignment.

The semi-analytical tool is developed in MATLAB; the solution (or the contact zone) domain was discretised with 85 elements in the *y*-direction (transverse direction) and with 35 elements in the *x*-direction (rolling direction). The validity of the current semi-analytical approach was verified against the so-called slicing method, which is implemented in SKF software. Due to the slicing method the three-dimensional contact problem is reduced to one dimension: the contact pressure distribution is discretised (sliced) along the *y*-coordinate and at each *i*-slice the Hertzian pressure distribution is defined in terms of the maximum contact pressure p_0^i and the contact zone length, b^i (see Fig. 6). The comparison between the slicing method and the current one is presented in Figs. 7, for a fully aligned and a slightly misaligned (0.4 minutes) contacts. As is shown in Figs. 7, both methods provide almost the same solutions, meaning that the currently implemented one can be safely used for the contact pressure analysis.

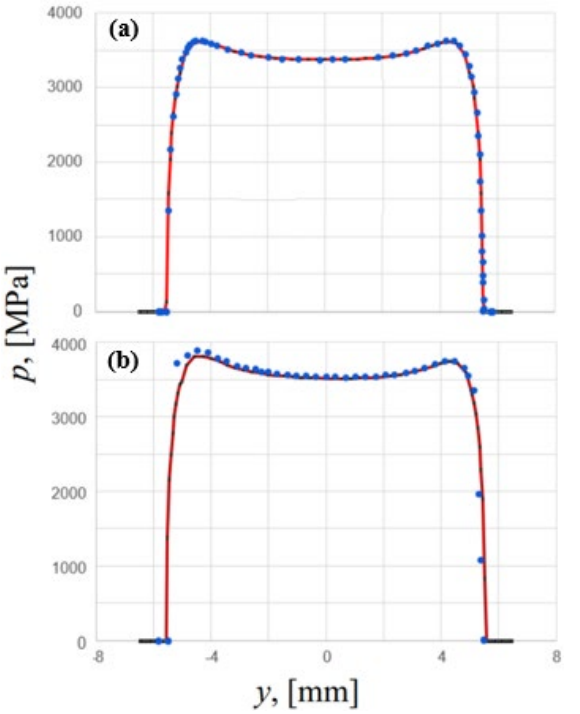

Figure 7: Comparison of the current semi-analytical method (for the contact pressure evaluation) with the slicing method (implemented in SKF software). The continuous curves correspond to the current solution and the symbols to the solution by the slicing method; the contact pressure distribution without misalignment (a) and with misalignment of 0.4 minutes (b).

FE modelling of imperfection

The FE domain containing imperfection is created with the technique schematically presented in Fig. 8. By using this technique, the geometry of MM can be easily modified at the pre-processing stage, which is essential for the parametric study aiming to cover wide range of imperfection dimensions. A segment of an ellipse is revolved around the axis of revolution located at the distance s from the ellipse axis, and by this the material is "carved" out of the roller chamfer. The long axis of the ellipse is constrained to remain tangent to the arc of the chamfer, while the revolution axis (of the imperfection) can move by varying the distance s. The geometrical configuration of MM is defined here by the four parameters: the dimensions l, w and d correspond to the MM size, and the angle α to its position (the distance r). The MM length, l, is changed by varying the distance s; by varying the angle α the imperfection position is changed and can partially protrude to the raceway zone (meaning that r gets negative).

The material domain presented in Fig. 9, mimics the portion of a ceramic roller located close to the chamfer, where the imperfection of ellipsoidal shape is located. The commercial package ABAQUS is used here for the FE analysis. The FE model comprises around 120,000 linear (8-nodes brick) elements, and the mesh density is not uniform through the domain (see Fig. 3): it increases in the vicinity of the imperfection while the rest of the domain is roughly meshed. Finally, based on the precision analysis the current FE discretisation was proven being sufficiently fine.

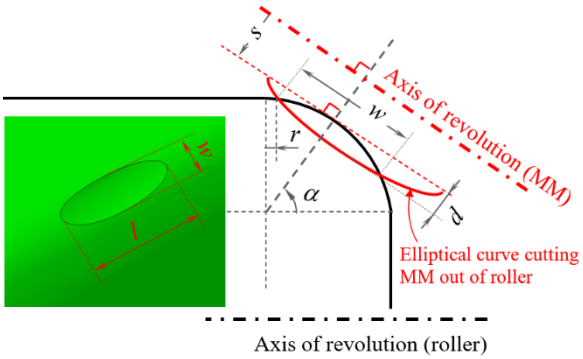

Figure 8: Creating the FE model at the pre-processor stage. The MM of the prescribed ellipsoidal geometry is "carved" out of the roller by revolving the elliptical segment.

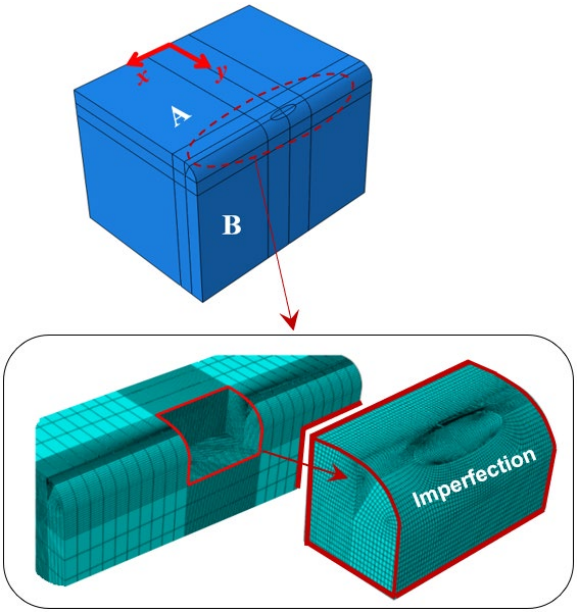

Figure 9: FE model of a ceramic roller with MM imperfection at the chamfer. The mesh density increases towards the imperfection zone.

The stress boundary conditions, associated with the moving contact pressure, are applied on the upper face of the domain, denoted by "A" (see Figs. 9). The face denoted by "B" corresponds to the roller end face, and is free of any boundary condition. All other faces of the FE domain are clamped: each node located on these faces is constrained to move in all three directions. The semi-analytically evaluated contact pressure is applied on the FE domain (face "A") and is "animated" by using the standard ABAQUS subroutine UTRACLOAD. In addition to the contact pressure a traction in x-direction is applied, by multiplying the pressure by the Coulomb friction coefficient (equals to 0.05 in the current analysis, since good lubrication is considered).

Results

Typically, stresses due to contact loads are compressive which is favourable for ceramics, because these materials usually have higher strength under compression compared to tension. Nevertheless, in some cases local tension is present which can trigger initiation and propagation of cracks. As follows from FE simulations (see Fig. 10), some localised tension can be present in the vicinity of the chamfer zone, while the rest of the domain is subjected to compression. The stresses in Fig. 10 are computed for the roller with perfect chamfer, while in the case it is damaged by MM, the tensile stress can get even higher (which is the main focus of the current study) as result of the stress concentration effect. Note, that the distribution of tensile stress σ_{xx} (see Fig. 10) is not symmetric, but gets higher behind the contact zone which is associated with the surface friction.

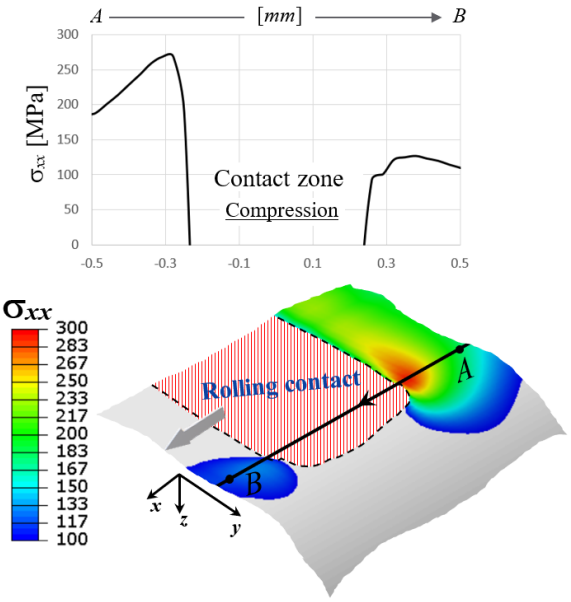

Figure 10: Local tension at the roller chamfer; no imperfection is present.

It should be noted, that the stresses presented in Fig. 10 correspond to the extreme loading conditions (see Fig. 11b): due to high contact load and misalignment, the pressure penetrates out of the raceway and gets locally extremely high. In the other words, the raceway to chamfer transition acts as a stress raiser and the pressure peak is the result of the contact zone truncation. It is important to note, that the contact pressure in Fig. 11b is over-estimated at the peak due to assuming purely elastic behaviour of the counter-face (bearing ring). In reality, however, this high pressure is supposed to mitigate due to local plastic flow at the steel ring surface.

Imperfections of four different types are considered in the current work for the FE stress analysis (see Figs. 12). All imperfections have ellipsoidal shapes and differ from each other due to their dimensions (defined by *l, w* and *d*) and the position relatively to the raceway (defined by *r*). The imperfections MM-A and MM-C can reasonably mimic the elongated MMs (see Fig. 3b), while MM-B is more suitable for the MMs of circular shape (see Fig. 3a). The imperfection MM-C partially penetrates into the raceway, which is a possible scenario, too, as was identified during the morphology characterisation. The shape of the imperfection MM-D is not typical for MMs, however it is included into the current parametric analysis in order to cover the wide range of MM geometries. The MMs dimensions in Figs. 12 covers the worst cases of the imperfection sizes identified in the experimental part.

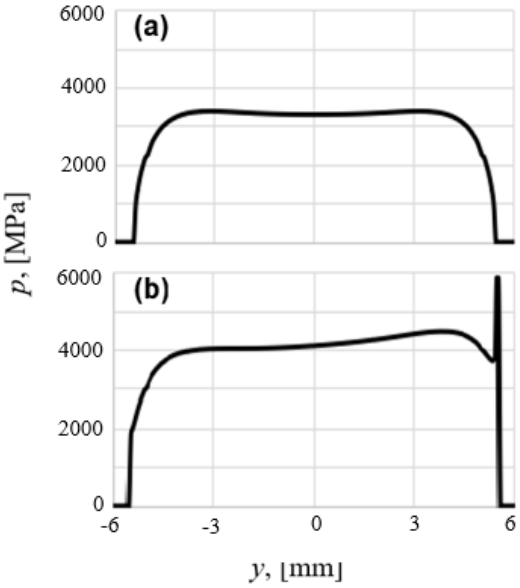

Figure 11: Pressure distribution along the y-coordinate (at x=0) for the roller of 11x12 mm (load F is applied along the z-direction, see Fig. 6). Normal conditions (a): F=1150 kgf (no misalignment); contact pressure occupies 100% of the raceway. Extreme loading conditions (b): F=1870 kgf + misalignment of 3 min; contact load occupies 102% of the raceway.

Maximum tensile stress criterion (known as the Rankine criterion) is used in the current work to assess the risk of RCF failure. The maximum tension occurring at certain position of contact load during the over-rolling is presented in Figs. 13, for the four different types of imperfection considered here. As can be seen from the normalized stress fields, the localized tensions in the vicinity of MMs are of moderate values, compared to the fatigue strength, σ_f, of Si3N4. The only exigent case is MM-C, where the imperfection slightly protrudes into the raceway (see again Figs. 12). This results in rather high local tension, slightly exceeding the σ_f value.

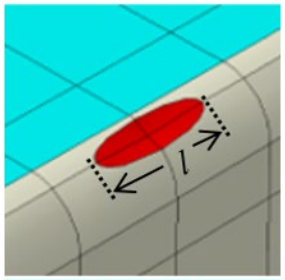

MM-A	µm
Length, *l*	1100
Width, *w*	310
Depth, *d*	50
Position, *r*	72

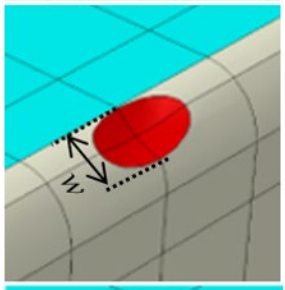

MM-B	µm
Length, *l*	920
Width, *w*	490
Depth, *d*	100
Position, *r*	23

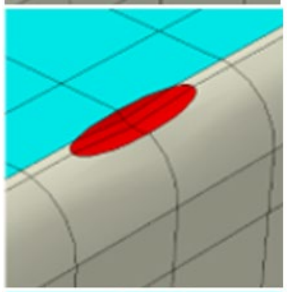

MM-C	µm
Length, *l*	1200
Width, *w*	290
Depth, *d*	50
Position, *r*	---

Partially penetrates to the raceway zone

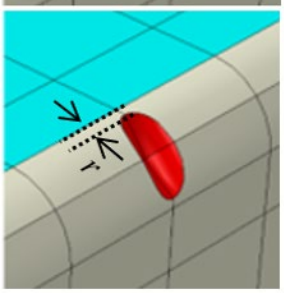

MM-D	µm
Length, *l*	320
Width, *w*	630
Depth, *d*	150
Position, *r*	72

Figure 12: MMs of four different configuration are considered in the current FE analysis (the MM depth is not shown on the figure).

Recall, that for the sake of being on the safe side, the loading conditions were exaggerated (see again Fig. 11b): high contact load + enormously high misalignment (3 min!). Nevertheless, assuming that such conditions are plausible, the risk of failure is estimated by comparing the tensile stress (corresponding to MM-C – the most critical case) to the tensile fatigue strength of Si3N4. According to 4-points bending test the strength of engineered Si3N4 under tension is in the range 1.075 – 1.2 GPa, within the 90% confidence interval [10], while under cyclic conditions, it is supposed to be lower. Based on our experience, the tensile fatigue strength, σ_f, was roughly estimated and used to normalize the results in Figs. 13. Again, in the case of MM penetrating into the raceway (MM-C) the local tension at the imperfection is comparable to the fatigue limit, meaning that in such case precaution should be taken to ensure reliable roller performance.

Finally, it is important to note that the strength indicated by the 4-points bending test [10] corresponds to rather large stress volume, estimated in the range of 2–3.5 mm^3 [11]. In the current case, however, it is much smaller: according to FE analysis high tensile stress in the vicinity of MM-C occupies around 1.2×10^{-5} mm^3, meaning that the strength within such micro-volume is supposed to be higher. How to relate the tensile micro-strength of ceramics to the stress volume size, was proposed in [11]:

$$\frac{\sigma_t^1}{\sigma_t^2} = \left(\frac{V^2}{V^1}\right)^{1/m} \quad (1)$$

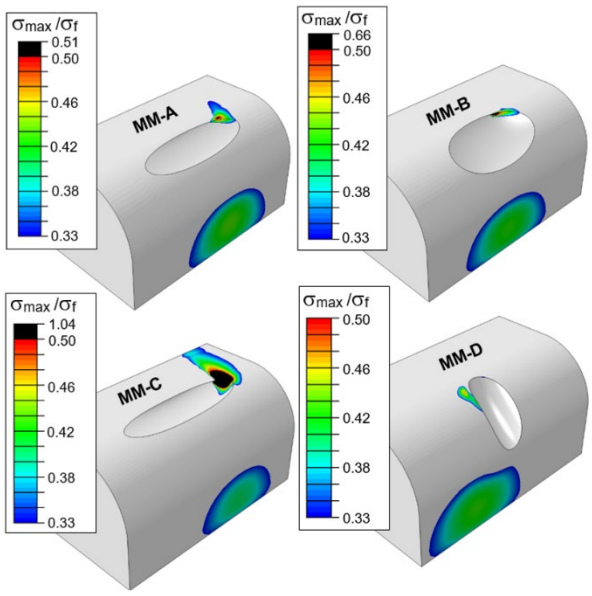

Figure 13: Maximum tension (in terms of principle stress normalized by the fatigue strength) occurring at certain position of contact load (under the extreme loading conditions, see Fig. 11b).

In Eq. (1) $\sigma_t{}^i$ denotes the tensile strength inherent to the material at volume V^i , and m is the Weibull modulus. For the Weibull modulus, of 16 (corresponding the 90% confidence interval), the micro-strength according to Eq. (1) exceeds 2 GPa. This extends the safety margin, meaning eventually, that the risk associated with the edge imperfection of the type Missing Material is low.

Finally, it should be mentioned that MM partially penetrating to raceway can cause the reduction of kappa (defining the thickness of lubrication film), because lubricant can escape from the contact. The reduction of film thickness due to the presence of surface dent was studied in [12], and this phenomenon is certainly critical in a full steel bearing and less in a hybrid [3].

Conclusions

According to the current analysis, MMs at the roller edges represent a minor risk of fatigue failure. It is concluded by the evaluation of maximum tensile stresses in the imperfection vicinity and comparing it to the fatigue strength of Si3N4. Nevertheless it was found, that the imperfection partially penetrating to the raceway can lead to the stress level that is comparable to the fatigue strength. However, this was estimated based on the 4-points bending test data, which corresponds to rather large stress volume (estimated in the range of 2–3.5 mm^3). In the current case, however, the volume subjected to high stress (slightly exceeding the fatigue strength) is much smaller, meaning that the strength within such micro-volume is supposed to be higher. Finally recall, that in order to stay "on the safe side", extreme contact conditions (very high contact load and enormously high misalignment) were selected for the current analysis. This further boost our confidence in the proposed model. Finally note, that edge imperfections of other types can be investigated in future, by applying either tensile stress or fracture mechanics based criteria and using the similar modelling technique.

References

[1] Wang, L., Snidle, R.W., Gu, L., Rolling contact silicon nitride bearing technology: a review of recent research, Wear 246 (2000), 159–173.
[2] Kadin Y., Modeling of hydrogen transport in static and rolling contact, Trib. Trans. 58 (2015), 260–273.
[3] Vieillard, C., Kadin, Y., Morales-Espejel, G.E., Gabelli, A., An experimental and theoretical study of surface rolling contact fatigue damage progression in hybrid bearings with artificial dents, Wear, 364-365 (2016), 211-223.
[4] Kadin, Y., Rychahivskyy, A., Modeling of surface cracks in rolling contact", Mater. Science & Eng. A, 541 (2012), 143-151.
[5] Lai, J., Kadin, Y., Vieillard, C., Characterization and modelling of the degradation of silicon nitride balls with surface missing-material defects under lubricated rolling contact conditions, Wear, 398-399 (2018), 146-157.
[6] Zolotarevskiy, V., Kadin, Y., Vieillard, C., Hadfield, M., Modeling the criticality of surface imperfections in silicon nitride balls under rolling and sliding contact, Tribology International, 148 (2020), 106317.
[7] De Mul, J.M., Kalker, J.J., Fredriksson, B., The contact between arbitrary curved bodies of finite dimensions, J. Trib., 108 (1986), 140-148.
[8] Hamrock, B.J., Schmid, S.R., Jacobson, B.O., 2004, Fundamentals of Fluid Film Lubrication, Second edition, Marcel Dekker, Inc.
[9] Jin, X., Keer, L., Wang, Q., Chez, E., Conjugate gradient method for contact analysis, Encyclopedia of tribology (2013), Springer, 447-501.
[10] Supancic, P., Danzer, R., Harrer, W., Wang, Z., Witschnig, S., Schöppl, O., Strength tests on silicon nitride balls, Key Eng. Mater., 409 (2009), 193-200.
[11] Quinn, G.D., Weibull strength scaling for standardized rectangular flexure specimens, J. Am. Ceram. Soc., 86 (2003), 508-510.
[12] Morales-Espejel, G.E., Gabelli, A., A model for rolling bearing life with surface and subsurface survival: sporadic surface damage from deterministic indentations, Tribol. Int., 96 (2016), 279-288.

Transient Thermal Analysis of the Contact in Bearings Exposed to Electrical Currents

Omid Safdarzadeh, Martin Weicker, Andreas Binder

Technical University of Darmstadt / Institute for Electrical Energy Conversion

Abstract– Electrical bearing currents, e.g. in inverted-fed electrical machines, may disturb the performance of the bearings via damaging the raceway surfaces (mainly fluting). In this paper the steady-state and transient temperature of the bearing surface at the electrical contact points between the balls and the raceway (the so-called *a*-spots) is derived in the mixed lubrication state, where metallic contacts are possible. The thermal analysis is based on the electric contact model of *Holm*. First, the contact temperature is analytically calculated. Then, the finite element simulations are performed to calculate the contact temperature. Temperature-dependency of the metal electrical resistivity ρ is considered based on *Wiedemann-Franz-Lorenz* law. The sensitivity analyses for the contact parameters are presented. The simulation results are compared to the findings of *Holm*, *Andreason*, *Slade* and *Carslaw* on the temperature rise in the contact at the electric current flow. The model can be utilized to predict the instantaneous contact temperature at a given *a*-spot for any given bearing from the measured bearing voltage. The bearing voltage and the bearing current are measured at dc and at ac (50 Hz, 10 kHz, 100 kHz, 500 kHz, 1 MHz) from the experimental setup, designed for the axial ball bearing, type 51208. The electric contact temperature on the bearing surface is then interpreted from the measured bearing voltage. The photos from the bearing surface showing the melted a-spots and black-color burned oil validate the existence of the high temperatures.

Keywords – Electrical machines, bearing damage, bearing current, bearing voltage, thermal analysis, bearing surface temperature, lubrication degradation.

List of parameters

Parameter	Symbol	Unit	Parameter	Symbol	Unit
Thermal conductivity of steel	λ	$\mathrm{W/(m \cdot K)}$	Contact voltage	U_c	V
Electrical resistivity	ρ	$\Omega \cdot \mathrm{m}$	Contact current	I_c	A
Absolute ambient temperature	T_amb	K	*a*-spot radius	a	µm
Absolute contact temperature	T_c	K	Model radius	b	µm
Wiedemann-Franz-Lorenz constant	L	$2.445 \cdot 10^{-8}$ $\mathrm{V^2/K^2}$	Model voltage	U	V
Contact temperature rise	ΔT_c	K	Mass density of steel	γ	$\mathrm{kg/m^3}$
Radius in spherical coordinates	r	m	Heat power density	p	$\mathrm{W/m^3}$
Specific heat capacity	c	$\mathrm{J/(kg \cdot K)}$	*Young*'s modulus	E	GPa

1. Introduction

Bearing currents may occur in mechanical roller bearings of e.g. inverted-fed electrical machines. The performance of these bearings may suffer from the bearing currents. The bearing current can degrade the properties of the lubricant and/or may damage the bearing raceway surface and the roller elements. Observations show plastic material deformations on the bearing surface such as fluting, leading to bearing vibration and gradually bearing failure, caused by increased friction [1].

Although the electrical bearing current and its effects in the electrical machine have been investigated for a long time and the critical operating conditions have been well identified [2], [3], a clear physical description of the damaging process is still under research.

In this paper, the contact theory of mechanical switches, [4], [5], [6], is employed for the bearing's electric contact to calculate the temperature on the bearing surface at the contact points between the balls and the raceway. The thermal damage happens in microscopic scale at the presence of a bearing current. Here, the thermal analysis is developed for the bearing in mixed lubrication state, where the metal-metal contacts occur, hence in a rather low speed range between $100\,\mathrm{min^{-1}}$ and $800\,\mathrm{min^{-1}}$ for small and medium sized roller bearings. At full lubrication e.g. at higher speeds, where there is no metallic contact between the ball and raceway, the findings here may not be applicable.

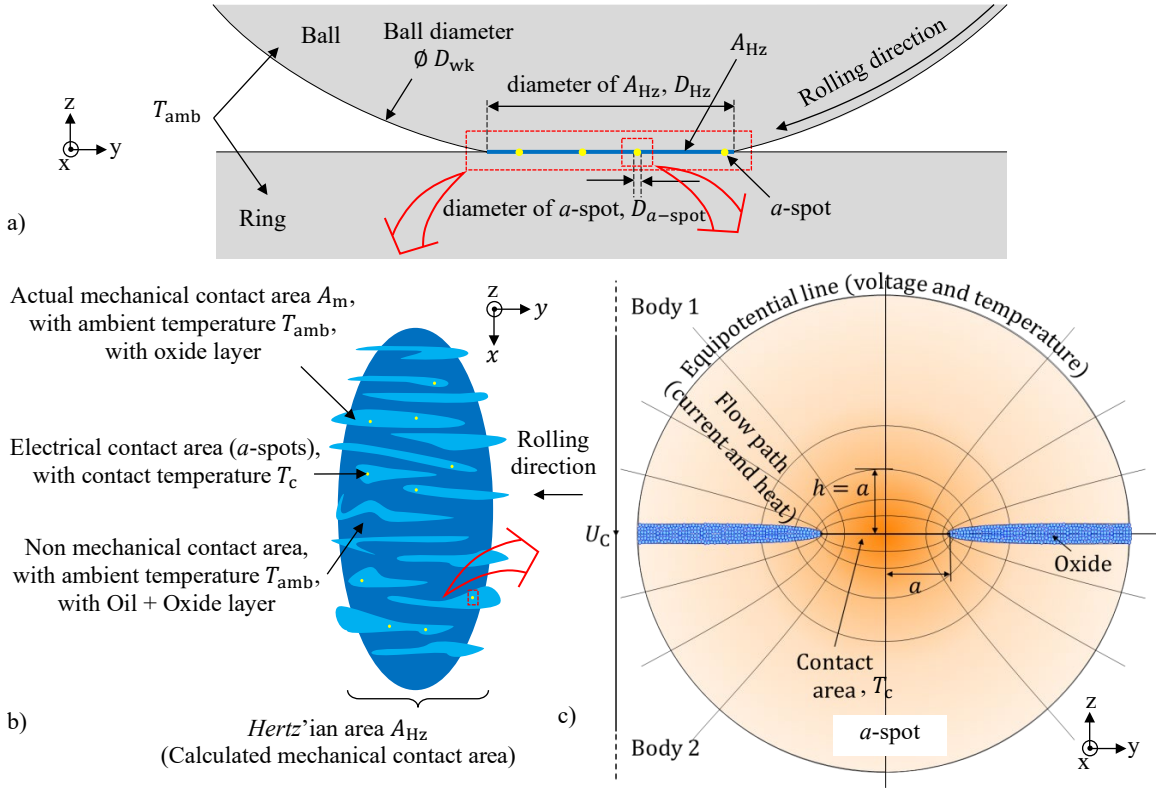

Fig. 1. *Holm*'s contact model. Schematic picture a) of the contact between the ring and the rolling ball in a roller bearing b) of the calculated mechanical contact area $A_{Hz} = \pi \cdot {D_{Hz}}^2/4$ (*Hertz*'ian area), actual mechanical contact area A_m, and electrical contact area $A_e = n \cdot \pi a^2$. (n is the number of the a-spots). c) A symmetric electrothermal contact between two contact bodies: body 1 (e.g. ball) and body 2 (e.g. ring). Electric equipotential and isothermal surfaces are concentric semi-ellipsoids. The electric contact area in the a-spot is circular. The contact voltage U_c is the voltage between an infinite far point from contact area in body 1 and an infinite far point from contact area in body 2. The contact current I_c passes the contact area (a-spot). The flow paths of electrical current and heat are shown. An oxide film fills the interspace between the contact bodies outside the a-spot.

Imaging the ball rolling on the ring as shown in Fig. 1 a), there are metallic contact points (a-spots) between the balls and the ring in the mixed lubrication state. The actual mechanical contact area A_m, depending on the contact force and the material properties, is smaller than the *Hertz*'ian area A_{Hz} [7]. The electrical contact area A_e is much smaller than the mechanical area A_m, by roughly 1000 times, Fig. 1 b) [8]. The contact areas generally have arbitrary shape. *Holm* has indicated that considering a circular area with radius a for the contact spot facilitates the analytical calculation and gives acceptable results in general [4].

2. Contact at steady state

Based on *Holm* [4], the contact voltage U_c, applied between the two contact bodies, forms equipotential concentric semi-ellipsoid surfaces around the contact area, Fig. 1 c). The voltage gradient is much bigger in the vicinity of the contact area than at distant surfaces. Half of the contact voltage is concentrated within the space at vertical distance $h = a$ from the contact area, Fig. 1 c). Hence, the contact body around the a-spot determines the contact characteristics, and the rest of the body can be neglected.

In a symmetric contact, the electrical and thermal fields are symmetric in both of the contact bodies. Thermal conductivity λ and electrical conductivity $1/\rho$ in metals are originated from the same physical mechanism [9], so electrical current flow and heat flow, respectively described by *Fourier*'s and *Ohm*'s law, behave in a similar way [9]. Hence, a simple relation connects the "thermal resistance" R_{th} and the "electrical resistance" R_{el} between two points. The contact temperature rises due to the ohmic loss of the electric current. Due to the similarity of *Fourier*'s law and *Ohm*'s law, the same isothermal and equipotential surfaces are formed around the contact areas, Fig. 1 c). For the heat flow calculation *Fourier*'s law is valid. The very small thermal relaxation time $\tau_0 = 1.6 \cdot 10^{-12}$ s for carbon steels [16] and for the micro-meter scale of the a-spot model, results in a negligible heat propagation time. Hence the *Cattaneo*-extension for the relativistic heat conduction can be neglected [17].

The electrical resistivity ρ is much more dependent on temperature than the thermal conductivity λ [10]. Among the material properties, the electrical resistivity ρ is almost linearly dependent on absolute temperature T. The dependency of the thermal conductivity λ, of the specific heat capacity c and of the mass density γ on the temperature T is much smaller than ρ, so that they are considered constant

[15]. The *Wiedemann-Franz-Lorenz* (WFL) law for metals

$$\rho(T) \cdot \lambda(T) = L \cdot T \qquad (1)$$

depends on $L \approx 2.445 \cdot 10^{-8}\ \mathrm{V^2/K^2}$, which is almost independent of the type of metal and of the absolute temperature T of the material [9]. Using (1), *Holm* has derived [4]

$$L \cdot ({T_\mathrm{c}}^2 - {T_\mathrm{amb}}^2) = \frac{{U_\mathrm{c}}^2}{4} \quad , \qquad (2)$$

with the absolute temperature of the contact T_c and of the ambient T_amb. From (2), the steady state contact temperature T_c at thermal equilibrium is calculated. In a ball bearing, the contact voltage between the rotating ring and the balls equals the contact voltage between the stationary ring and the balls, $U_\mathrm{b} = 2 \cdot U_\mathrm{c}$. The contact temperature rise $\Delta T_\mathrm{c} = T_\mathrm{c} - T_\mathrm{amb}$ is derived from the given bearing voltage U_b (Fig. 2). For simplicity, the ambient temperature $T_\mathrm{amb} = 273.15$ K, or $\vartheta_\mathrm{amb} = 0$ °C. Hence $\Delta T_\mathrm{c} = \Delta\vartheta_\mathrm{c} = \vartheta_\mathrm{c}$.

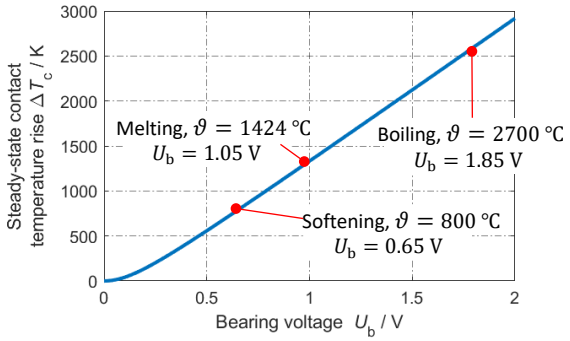

Fig. 2. Steady state contact temperature rise ΔT_c for a given bearing voltage U_b (2). The softening, melting and boiling temperature for steel material 100Cr6 [18] are indicated. $\vartheta_\mathrm{amb} = 0$ °C is assumed.

Fig. 2 shows, that in the bearing at the local electric contact points the local contact temperature can reach the boiling temperature, if a bearing voltage $U_\mathrm{b} \approx 1$ V is provided and if the contact has enough time to reach the steady state temperature.

3. Contact at transient

3.1. Analytical calculations

Andreason has suggested a simplified contact model using a spherical contact surface with radius a instead of the elliptical surfaces of *Holm* in Fig. 1 c) [11]. *Andreason*'s model has therefore spherical symmetry for the electric potential and for the temperature field, which makes the analytical study much easier. The temperature equation in time t for spherical coordinates is

$$\gamma \cdot c \cdot \frac{\partial \Delta T}{\partial t} = \frac{1}{r^2} \cdot \frac{\partial}{\partial r}\left(\lambda \cdot r^2 \cdot \frac{\partial \Delta T}{\partial r}\right) + p(r) \quad , \qquad (3)$$

where r is the radius in spherical coordinates, and $p(r)$ is the ohmic loss power density due to the contact current I_c at the radius r,

$$p(r) = \rho \cdot \left(\frac{I_\mathrm{c}}{2\pi \cdot r^2}\right)^2 , \qquad a \le r \qquad . \qquad (4)$$

For the transient solution of (3), *Andreason* proposed to linearize the temperature rise using $\partial T/\partial t$ to estimate the temperature rise time, which leads to only rough approximations. *Carslaw* and *Jaeger* have shown [12], that the transient solution of (3) has a dominating time constant

$$\tau = \frac{\gamma \cdot c \cdot a^2}{4 \cdot \lambda} \qquad . \qquad (5)$$

Their solution is combined with the steady-state solution of (3) as

$$\Delta T_\mathrm{c}(t) = \Delta T_\mathrm{c} \cdot (1 - e^{-\frac{t}{\tau}}) \qquad . \qquad (6)$$

We call this calculation "Method 1".

Holm has presented diagrams in [4] for the numerically calculated contact temperature rise over time $\Delta T_\mathrm{c}(t)$, which we call "Method 2". Our own numerical simulation model, according to Section 3.2, we call "Method 3".

According to *Slade* [6], in mechanical switches the transient of temperature rise is so short, that one can assume the steady state temperature for the contact as soon as the contact is made. Due to the relatively short mechanical contact time between the ball and the ring, this transient state is of interest for the study of the bearing current in the bearings. We will show in the following with the example in Table II, that even for the short living mechanical contact between the ball and the ring, the local contact temperature may reach the steady-state value very likely.

3.2. Simulation results

Holm's contact model is simulated via finite element analysis in *COMSOL* Multiphysics® with the boundary and initial conditions shown in Fig. 3 a). The voltage drop on the upper half of the symmetric model is $U = 0.2$ V, which represents a contact voltage of $U_\mathrm{c} = 0.4$ V in Fig. 1 c). We use n as normal vector on the boundary surface. Due to the oxide layer, the model is insulated electrically from below, $\mathrm{d}U/\mathrm{d}n = 0$, except at the contact area of the a-spot, with radius a, where the electric potential is assumed to be $\varphi = 0$ V. The model is, due to symmetry, insulated thermally from below, $\mathrm{d}\vartheta/\mathrm{d}n = 0$. The initial voltage and the initial temperature rise $\Delta T(0)$ overall is zero. Due to the very big scale of the model radius b, comparing with the small a-spot radius a, the mesh is refined close to the a-spot as shown in Fig. 3 b), to achieve an accurate solution for the contact region.

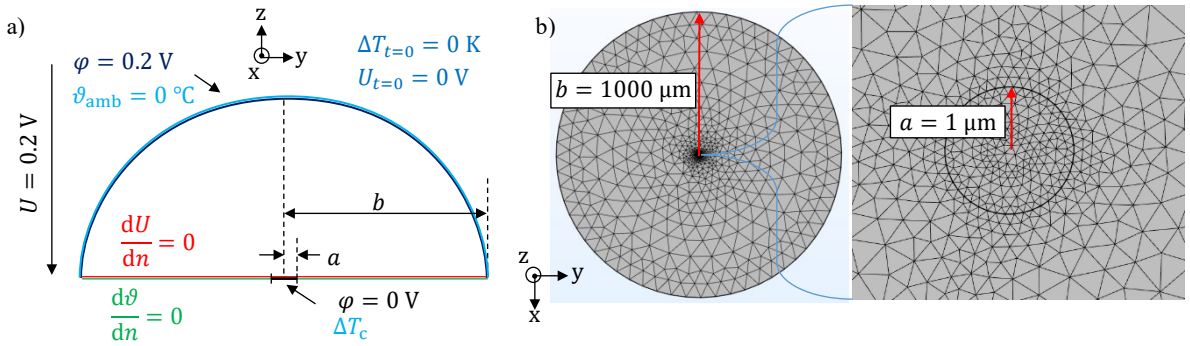

Fig. 3. Simulation of contact temperature rise ΔT_c in *Holm*'s contact model in *COMSOL* Multiphysics®. a) The electrical and thermal boundary and initial conditions. b) Meshing of the *Holm* model, a-spot radius = 1 µm, model radius $b = 1000$ µm.

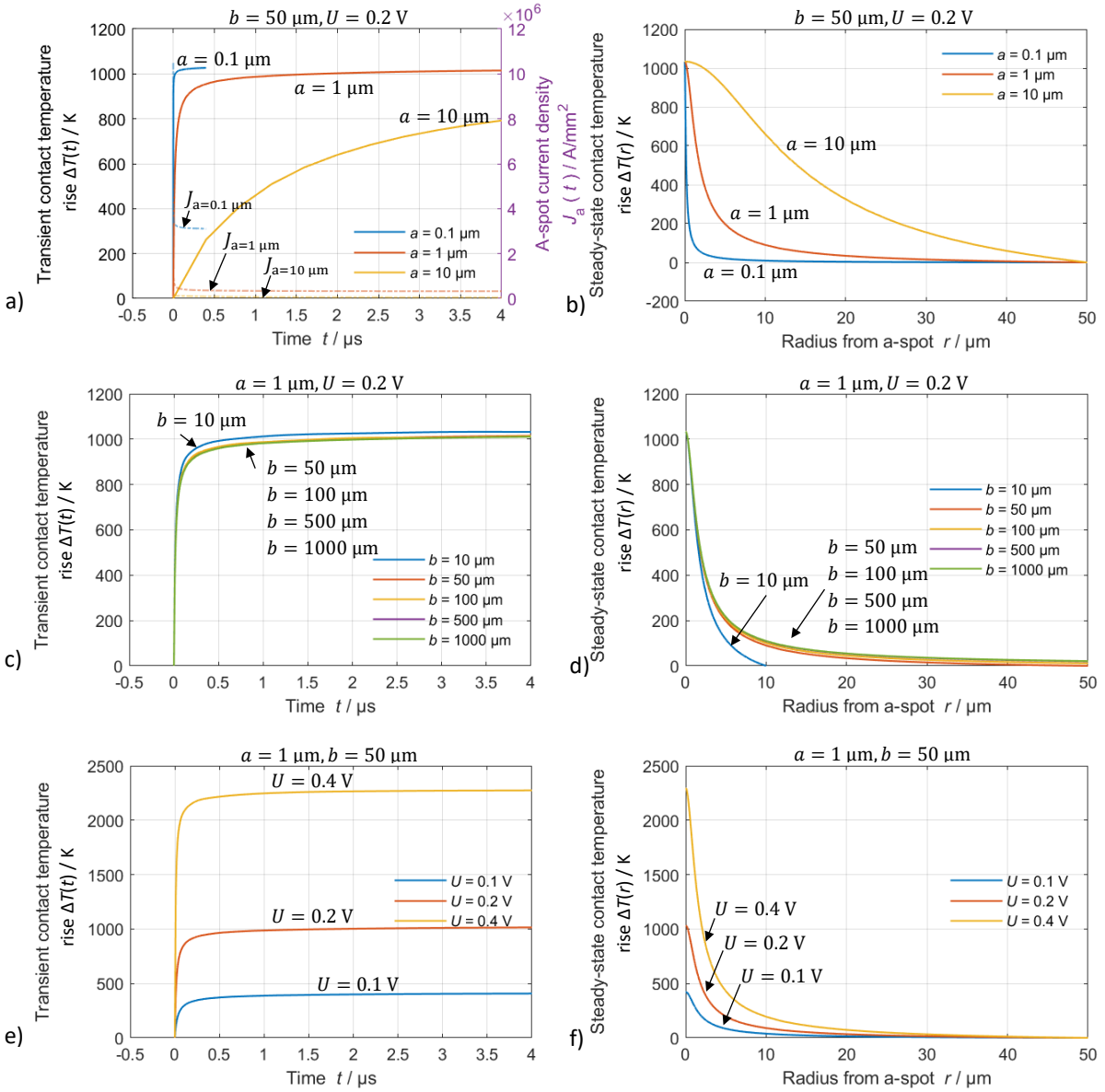

Fig. 4. Parameter study (Table I) for the contact transient and steady-state temperature rise ΔT_c of *Holm*'s model (Fig. 3). a), b): Sensitivity analysis for the a-spot radius a. c), d): Sensitivity analysis for the model radius b. e), f): Sensitivity analysis for the model voltage U. Simulation in *COMSOL* Multiphysics®. Constant thermal conductivity $\lambda_{100Cr6} = 33$ in W/(m · K). Temperature-dependent electric resistivity $\rho(T) = (L \cdot T)/\lambda = 7.41 \cdot 10^{-10} \cdot T$ (in Ω · m). From (2), analytically, if $U = U_c/2 = 0.2$, then $\Delta T_c = 1034.8$ K

Table I. Simulation results of the contact temperature rise ΔT_c and the *a*-spot current density J_a, based on the results in Fig. 4.

Variables			Transient				Steady state	
a / µm	b / µm	U / V	Fig. 4	t / µs	ΔT_c / K	$J_a / \frac{A}{\mu m^2}$	Fig. 4	ΔT_c / K
0.1	50	0.2	a)	0	0	10.5	b)	1033.5
				0.4	1026.9	3.11		
1				0	0	1		1033.5
				4	1015.0	0.322		
10				0	0	0.12		1033.5
				40	1011.5	0.037		
1	10	0.2	c)	4	1032.0	not assigned	d)	1031.5
	50				1015.0			1033.5
	100				1013.5			1033.5
	500				1010.8			1033.5
	1000				1010.5			1033.5
1	50	0.1	e)	4	407.5	not assigned	f)	421.8
		0.2			1015.0			1033.5
		0.4			2274.3			2296.6

The transient and steady-state solutions of the contact temperature rise, respectively $\Delta T_c(t)$ and $\Delta T_c(r)$, in the *a*-spot are given in Fig. 4. As well as the current densities in the *a*-spot J_a in Fig. 4 a).

A parametric study (Table I) is done using the model by varying the *a*-spot radius a, the model radius b, and the model voltage U.

In Fig. 4 a), increasing the *a*-spot radius a, results in longer temperature rise time τ, shown also by (5). This is due to the lower current density J_a at the *a*-spot region, which generates the ohmic-loss power density $p = \rho \cdot {J_a}^2$. The rise time for the *a*-spot with a radius of $a = 1$ µm is, due to numerical simulation in Fig. 4 a), c), e) and (5), less than 1 µs, implying the short temperature rise time τ. The temperature rises close to the *a*-spot region so much, that the rest of body mass can be neglected (Fig. 4 b)). The *a*-spot current density J_a has a much faster rise time than the contact temperature rise ΔT_c, as shown in Fig. 4 a) with the fast-decaying dashed lines.

Enlarging the model radius for values $b \geq 50 \cdot a$ has a negligible effect on the calculated temperature distribution in the *a*-spot Fig. 4 d). Hence selecting a model radius 50 times bigger than the *a*-spot radius $b \geq 50 \cdot a$ is sufficient to have an accurate simulation for the *a*-spot temperatures (Fig. 4 c)). Hence model radius b has for $b \geq 50 \cdot a$ no influence on the temperature rise time ΔT_c.

The model voltage U directly determines the contact steady-state temperature rise ΔT_c (Fig. 4 f)), which has been indicated also in (2). The model voltage U has no influence on the temperature rise time Fig. 4 e).

A comparison study between the three methods "Method 1", "Method 2" and "Method 3" is performed in Fig. 5 on the transient contact temperature rise $\Delta T_c(t)$: "Method 1" determines $\Delta T_c(t)$ from the analytical approximation in (6) via the exponential function, where the steady-state temperature $\Delta T_c = 1034.8$ K is calculated from (2) and the temperature rise time $\tau = 27.18$ ns is calculated from (5). "Method 2" uses the transient data calculated by *Holm* in [4]. "Method 3" shows the simulation results in *COMSOL* (Fig. 4 c), $b = 1000$ µm).

The exponential function of "Method 1" with one time constant τ (6) cannot fit the contact temperature rise $\Delta T_c(t)$ of the simulation. However, the presented exponential function may be used to make an approximation of the transient contact temperature. The data of "Method 2", presented by *Holm*, show a longer rise time. The contact temperature rise $\Delta T_c(t)$ reaches 63 % of its final values in "Method 1", "Method 2" and "Method 3", respectively after 0.027 µs, 0.272 µs and 0.030 µs and reach 95 % of its final values respectively after 0.081 µs, 0.960 µs and 21.744 µs.

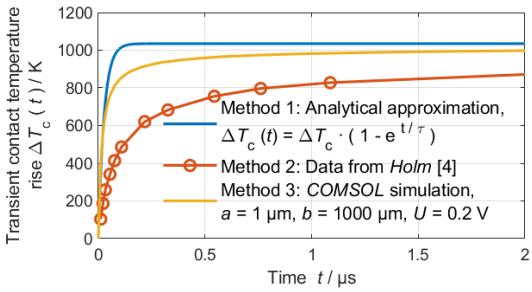

Fig. 5. Comparison study for the transient contact temperature rise $\Delta T_c(t)$ of the *Holm*'s model for *a*-spot radius $a = 1$ µm, thermal conductivity $\lambda = 33$ W/(m · K), specific heat capacity $c = 460$ J/(kg · K), mass density $\gamma = 7800$ kg/m^3.

In Fig. 5, the simulation result ("Method 3") should be the most accurate one, since no considerable simplification for the *a*-spot contact model is used. The analytical exponential function ("Method 1") represents the simulation results very well, within the time $t \leq \tau = 0.027$ µs.

3.3. Case study

Here an example is calculated for the rolling time of *a*-spot on the *Hertz*'ian area in the roller bearing, illustrated in Fig. 1 a). We want to check if the *a*-spot has mechanically enough time to reach the high temperatures, due to the electrical current flow. Assumed is an axial ball bearing, type 51208, with a bearing force $F_\mathrm{b} = 800\ \mathrm{N}$ and bearing speed $n = 500\ \mathrm{min}^{-1}$. The *Hertz*'ian contact area for one ball contact $A_\mathrm{Hz} = 0.11\ \mathrm{mm}^2$ is calculated. Assuming a circular *Hertz*'ian area, a *Hertz*'ian contact diameter $D_\mathrm{Hz} = \sqrt{A_\mathrm{Hz}/4 \cdot \pi} = 374\ \mu\mathrm{m}$ is calculated. For the given speed n, the frequency of the ball about its axis is $f_\mathrm{r} = 21.8\ \mathrm{Hz}$. The ball has the diameter $D_\mathrm{wk} = 10.55\ \mathrm{mm}$, hence the linear velocity of the ball at the contact point is $v = 2\pi \cdot \mathrm{f_r} \cdot D_\mathrm{wk}/2 = 722.7\ \mathrm{mm/s}$. For the *a*-spot radius $a = 1\ \mu\mathrm{m}$, the rolling time of the *a*-spot is calculated in Table II for two cases: 1) With elasticity $E = 210\ \mathrm{GPa}$ and 2) with elasticity $E \gg 210\ \mathrm{GPa}$.

Table II. Rolling time of the *a*-spot.

Case	Rolled diameter	*a*-spot rolling time	Ratio to the contact time constant (5)
1) $E = 210\ \mathrm{GPa}$	$D_\mathrm{Hz} = 374\ \mu\mathrm{m}$	$\Delta t_1 = \frac{D_\mathrm{Hz}}{v} = 517.5\ \mu\mathrm{s}$	$\frac{\Delta t_1}{\tau} = 17250$
2) $E \gg 210\ \mathrm{GPa}$	$D_\mathrm{a-spot} = 2 \cdot \mathrm{a} = 2\ \mu\mathrm{m}$	$\Delta t_2 = \frac{D_\mathrm{a-spot}}{v} = 2.77\ \mu\mathrm{s}$	$\frac{\Delta t_2}{\tau} = 92.3$

The shortest rolling time of the *a*-spot would be the case, where the *Hertz*'ian area would have a minimum value, we say $A_\mathrm{Hz} \to \pi \cdot a^2$, hence the elasticity of the contact body would be very big $E \gg 210\ \mathrm{Gpa}$. In this case, the ball only rolls over the *a*-spot and hence a short *a*-spot rolling time $\Delta t_2 = 2.77\ \mu\mathrm{s}$ is calculated. For a common elasticity, $E = 210\ \mathrm{Gpa}$, the *a*-spot remains on the *Hertz*'ian area, as it enters the *Hertz*'ian area (see Fig. 1 a)) and is mechanically separated, as it exits the *Hertz*'ian area, hence an *a*-spot rolling time of $\Delta t_1 = 517.5\ \mu\mathrm{s}$ is calculated. For the given *a*-spot radius $a = 1\ \mu\mathrm{m}$, the contact temperature time constant $\tau \cong 0.03\ \mu\mathrm{s}$ is calculated from (5). The contact time constant τ is so short, that even for the short *a*-spot rolling time Δt_2, the *a*-spot has enough time to reach the high temperatures $\Delta t_2/\tau = 92.3$, let alone for case 1), where $\Delta t_1/\tau = 17250$.

4. Experiments

4.1. Setup

To measure the bearing voltage u_b and bearing current i_b under controlled bearing speed n and bearing force F_b, the test rig in Fig. 6, was built. Each bearing has 15 balls. The bearings are electrically connected in series. The used equipment is listed in Table III.

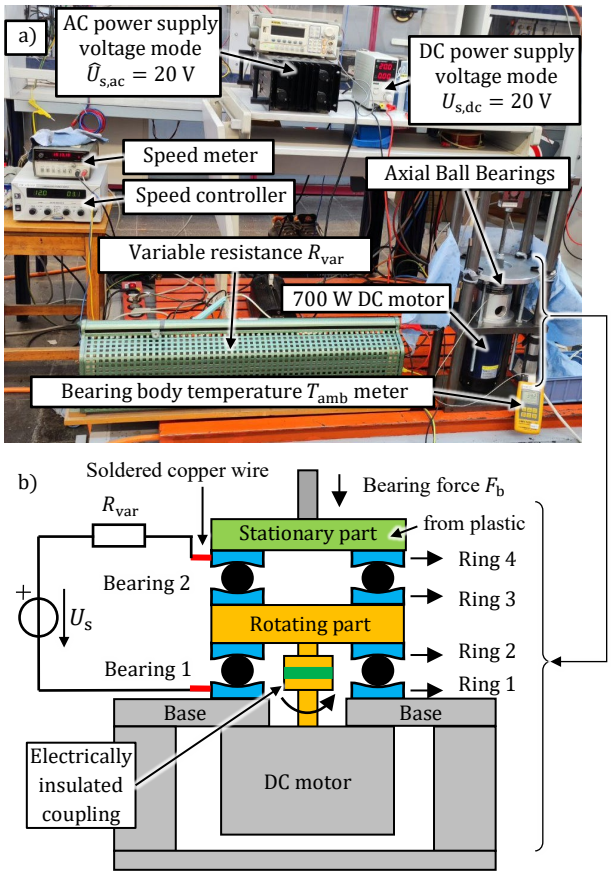

Fig. 6. The experimental setup. a) the used equipment b) the test rig structure. The test rig structure uses no mechanical brushes to measure the bearing voltage at rotation.

Table III. Used equipment and lubrication

Equipment	Description
Axial bearing	Type 51208, $z = 15$ balls, inner diameter $d = 40\ \mathrm{mm}$, outer diameter $D = 68\ \mathrm{mm}$, width $B = 19\ \mathrm{mm}$, company FAG
Oscilloscope	Waverunner LT364L, 500 MHz, accuracy 2 mV, vertical resolution 8 bits, capture memory 500 k samples
Current clamp	IWATSU SS-250, 100 MHz, max. 30 A, accuracy ±1.0% or ±10 mA
Voltage probe	TT-SI200, 200 MHz, ±60 V, accuracy ±1.0% or ±20 mV
DC power supply	Model K3010D, 30V, 10A, company LANG WEI
AC amplifier	Model Prefer point five, M.F. amplifier, company UMMELS Geleen
DC motor	Model 110ZYT, 24V, 700W, 3000 min^{-1}, company Lanjui
Lubrication	Mineral oil, with lithium thickener, water content 200 ppm, specific electrical resistivity $\rho \approx 10^{14}\ \Omega \cdot \mathrm{cm}$

The bearing voltage u_b is lower than 1.5 V and the source voltage u_s is 20 V. So, the variable resistance R_{var} between the voltage source U_s and the bearings (see Fig. 6 b)) can regulate the bearing current i_b. For DC measurements, the source voltage $U_{s,dc} = 20$ V is supplied from the DC power supply. For AC measurements $\hat{U}_{s,ac} = 20$ V is supplied from the AC amplifier at frequency up to 10 kHz. At higher frequencies, the output voltage of the AC amplifier decreases. Two copper wires are soldered on ring 1 and ring 4 to connect the bearings to the electric circuit. The voltage probes are connected close to the bearing rings to avoid measuring the voltage drop on the connecting cables.

To apply a bearing force F_b, a screw structure with a spring ring is used. The bearing force is measured via the load cell. Ring 1 and ring 4 are fixed. Ring 2 and ring 3 rotate. The rotation is provided by the shaft of the driving DC motor. The motor shaft is electrically insulated from the bearings via the insulated coupling. Temperatures of ring 1 and of ring 4 are monitored via the thermo-couple elements soldered on the rings.

Ring 1 is located on the metallic base, which has the room temperature 28 °C. Ring 4 can thermally conducts heat only via the balls. Therefore ring 1 is cooler than ring 4.

4.2. Measurements

The bearing voltage u_b and the bearing current i_b are measured at bearing speed $n = 1500\ \mathrm{min}^{-1}$, bearing force $F_b = 800$ N from the test ring in Fig. 6. For the given bearing force F_b, the *Hertz*'ian area $A_{Hz} = 1.648\ \mathrm{mm}^2$ is calculated. Before measuring the signals, the test rig is run without electrical current for 1 hour to settle the temperature and the lubrication state in the bearings. During the measurements, the temperature of ring 1 $\vartheta_{ring1} = 40$ °C and of ring 4 $\vartheta_{ring4} = 53$ °C are measured.

The measured bearing voltage u_b and the bearing current i_b at DC and at AC (50 Hz, 10 kHz, 1 MHz) are shown in Fig. 7. For dc, 50 Hz and 10 kHz, the source voltage amplitude $\hat{U}_s = 20$ V. At dc, 50 Hz and 10 kHz, the bearing voltage U_b is limited to $U_b \approx 1$ V. Based on Fig. 2, bearing voltage $U_b \approx 1$ V corresponds to the melting point of the bearing steel. So, one can interpret that at this voltage the electric contact asperities are melt down and create electric conductive channels. These channels are available, as long as the bearing voltage is kept. If the external electric circuit injects more current, these channels enlarge. The channels are extinguished, when, due to mechanical rotation, the contact bodies apart, or when no current is supplied externally, so the oxidation recovers the metallic surfaces.

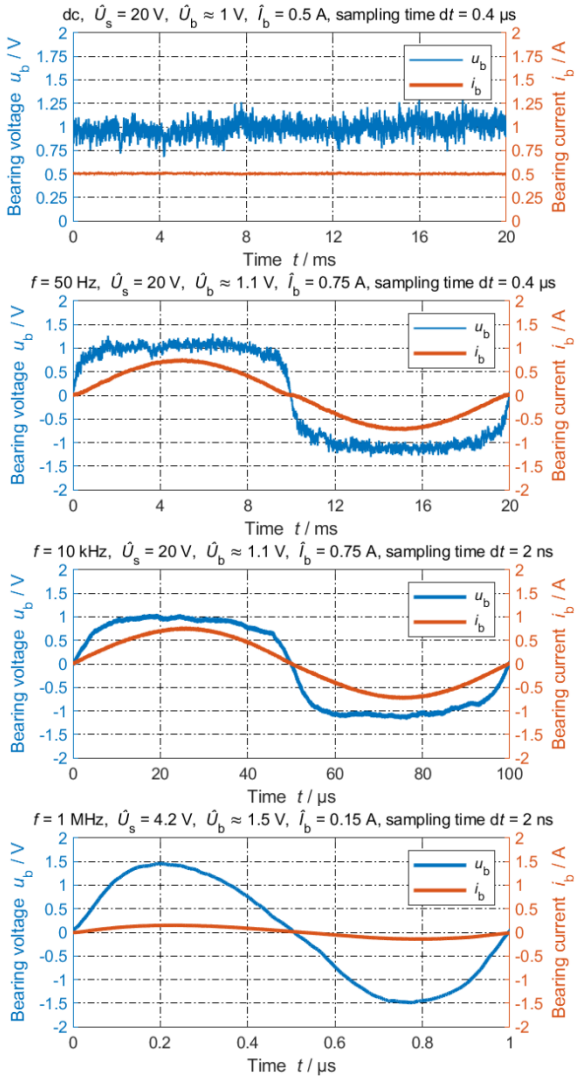

Fig. 7. Measured bearing voltage u_b and bearing current i_b for the test rig in Fig. 6. Bearing speed $n = 1500\ \mathrm{min}^{-1}$, bearing force $F_b = 800$ N, lubrication mineral oil, $\vartheta_{ring1} = 40$ °C, $\vartheta_{ring4} = 53$ °C, *Hertz*'ian area $A_{Hz} = 1.648\ \mathrm{mm}^2$. Measurements after a mechanical run of 1 hour.

For AC, at 1 MHz, the bearing voltage reaches $U_b \approx 1.5$ V at $t = 0.2$ µs. At 1 MHz, the amplifier can supply a voltage amplitude up to $\hat{U}_s = 4.2$ V. At $t \approx 0.1$ µs the bearing voltage reaches $U_b \approx 1$ V, afterward $U_b > 1$ V is available for $\Delta t \approx 0.25$ µs. Based on Fig. 5, this time span is in the range of times, calculated to reach the high contact temperatures ϑ_c for an a-spot with radius $a = 1$ µm. Therefore, it seems reasonable to explain the bearing "fritting" voltage of $U_b \approx 1$ V with the transient behavior of the a-spot.

An overview on the amplitude of the measured bearing voltage $\hat{U}_b$ for the bearing current amplitude $\hat{I}_b = 0.1 \ldots 3$ A at signal frequencies $f = 0 \ldots 1$ MHz are presented in Fig. 8.

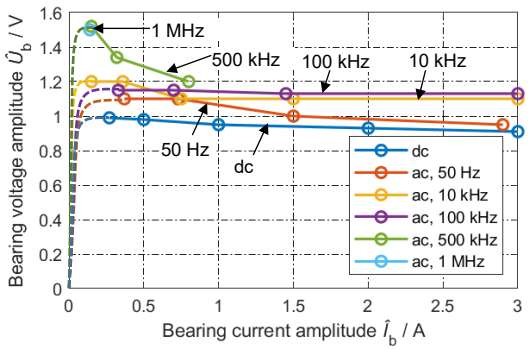

Fig. 8. Average amplitude of the measured bearing voltage $\hat{U}_b$ against the bearing current amplitude $\hat{I}_b = 0.1 \ldots 3$ A at signal frequencies $f = 0 \ldots 1$ MHz from the test rig in Fig. 6. Bearing speed $n = 1500\ \mathrm{min}^{-1}$, bearing force $F_b = 800$ N, lubrication mineral oil, $\vartheta_{ring1} = 40$ °C, $\vartheta_{ring4} = 53$ °C, *Hertz*'ian area $A_{Hz} = 1.648\ \mathrm{mm}^2$. Measurements after a mechanical run of 1 hour.

Fig. 8. shows, that the bearing voltage is almost independent from the bearing current. The bearing voltage amplitude $\hat{U}_b$ is around the melting voltage of the steel, 1.05 V (see Fig. 2), except at high frequencies, here 500 kHz and 1 MHz, where the dynamic of the contact temperature allows higher bearing voltages. The slight differences in the bearing voltage at dc, 50 Hz, 10 kHz and 100 kHz refers to the dynamic of the fritting, i.e. the creation of conductive metal channels between two metal bodies and their enlargement. Similar investigations on the bearing voltage U_b against the bearing current I_b were carried out by *Prashad* and *Pittroff* [13], [14], where bearing voltages around $U_b \approx 0.8$ V are reported.

4.3. Photos

The bearing surface, exposed to electric bearing current, shows micro changes on the surface. Based on our records, the changes may develop to fluting after a while or may remain not developing to fluting. The difference between a bearing exposed to bearing currents and a bearing with the same mechanical operating conditions but not exposed to bearing currents are shown in Fig. 9 and Fig. 10.

Fig. 9 a) shows parts of the ring 1a, the ring 2a and the cage for the bearing, exposed to dc bearing current $I_{dc} = 4$ A, via the setup shown in Fig. 6, where $U_s = 20$ V. The bearing in Fig. 9 b) have seen no bearing current. The micro changes on the surface of ring 1a and ring 2a are obvious. The lubrication exposed to the bearing current becomes dark in the first hours of operation. The lubrication without the bearing current keeps its original color. The fluting width is about $w \approx 300$ µm (Fig. 9 a)).

The micro changes, interpreted as the print of the melted a-spot, have a diameter between $D_{a-spot} \approx 0.3 \ldots 3$ µm.

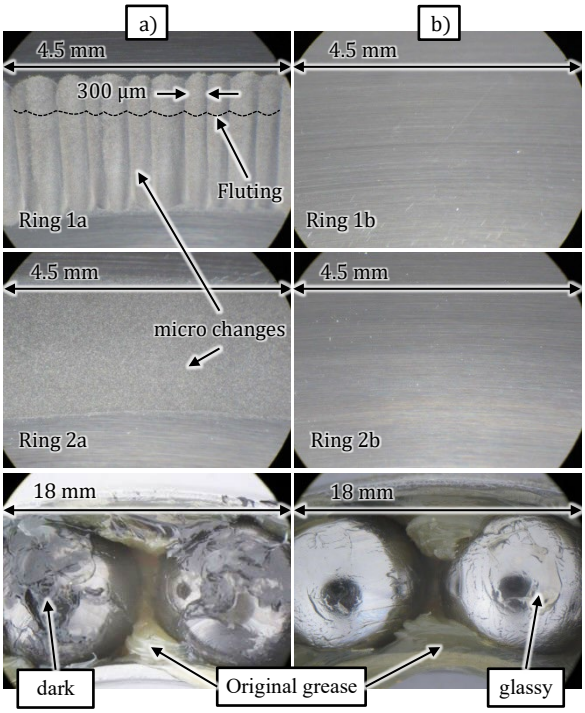

Fig. 9. Bearing surface and lubrication after 24 h operation. Axial ball bearing type 51208. Bearing speed $n = 1500\ \mathrm{min}^{-1}$, bearing force $F_b = 200$ N, lubrication *Arcanol Multi 3*.
a) With DC bearing current. Bearing voltage $U_b \approx 1$ V, bearing current $I_b = 4$ A, apparent bearing current density $J_{dc} = 6\ \mathrm{A/mm}^2$, Ring 1a temperature $\vartheta_{1a} = 44.4$ °C
b) Without bearing current. Ring 1b temperature $\vartheta_{1b} = 37.5$ °C.

Fig. 10 a) shows part of a raceway surface of a bearing, exposed to Electric Discharge Machining (EDM) bearing currents [1]. The high resolution photo of the bearing surface reveals the impact of melting temperatures on the *a*-spot. With the same mechanical operating conditions the bearing in Fig. 10 b), exposed to no bearing currents, does not have such impacts.

5. Conclusion

The findings propose an accurate contact model to study the temperature of the *a*-spots in bearings. The temperature at the *a*-spots ϑ_c can be calculated simply from the bearing voltage $U_b = 2 \cdot U_c$. The derived equations are based on the findings of *Holm*, *Wiedemann-Franz-Lorenz, Andreason* and *Slade* for the electric contact. The *a*-spot area comprises a very small portion of the mechanical contact area. Simulation of the *a*-spot was achieved via the finite element analysis in *COMSOL* Multiphysics®, using the constant thermal conductivity λ and the temperature-dependent electric resistivity $\rho(T)$. Simulations showed that the temperature decreases sharply within a short distance from the *a*-spots. A contact model, with an outer radius 50 times bigger than the *a*-spot radius $b \geq 50 \cdot a$, can represent very well the temperature distribution for an infinite big model $b = \infty$.

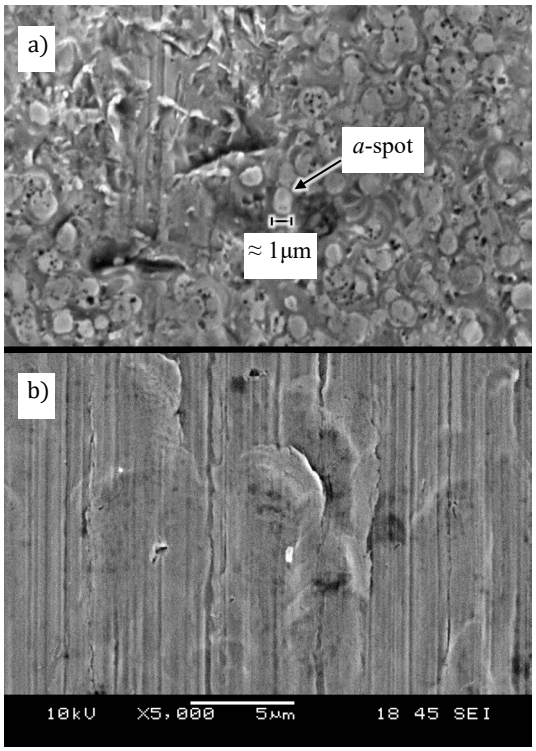

Fig. 10. Electron microscopy of the bearing raceway surface. Radial ball bearing type 7305, bearing speed $n = 1000\ \mathrm{min}^{-1}$, bearing axial force $F_{\mathrm{b,a}} = 3$ kN, bearing inner ring temperature $\vartheta_{\mathrm{ir}} = 30$ °C, bearing outer ring temperature $\vartheta_{\mathrm{or}} = 52.5$ °C, results after 500 h. [1]
a) With EDM bearing current. Average of the bearing voltage amplitude $\bar{U}_{\mathrm{EDM}} = 15$ V, average of the bearing current amplitude $\bar{I}_{\mathrm{EDM}} = 0.4$ A, average of the apparent bearing current density $\bar{J}_{\mathrm{EDM}} = 0.09\ \mathrm{A/mm^2}$, switching frequency $f_{\mathrm{s}} = 10$ kHz.
b) Without bearing current

The temperature rise time is highly dependent on the a-spot radius a. For an a-spot radius of $a = 1$ µm, the temperature reaches at 95% of its final value after 0.96 µs. The contact steady-state temperature $\vartheta_{\mathrm{c,ss}}$ is directly dependent on the bearing voltage U_{b}. The melting point 1424 °C of the contacting asperities at the a-spots are reached for a bearing voltage $U_{\mathrm{b}} = 1.05$ V. The measured bearing voltage is around $U_{\mathrm{b}} \approx 1$V. The bearing surface at the electric contact point is melted. The prints of the melted a-spot are observed on the raceway surface of a bearing exposed to bearing current, where the burned lubrication has a dark color. This may give a clue for the investigation of the damage, e.g. fluting, in the bearings exposed to electrical currents.

Acknowledgment

The Graduate School of Energy Science and Engineering of the Technical University of Darmstadt financed the funding for this research. This Project is also funded by the Deutsche Forschungsgemeinschaft (DFG, German Research Foundation) - DFG project Nr. 407468812.

References

[1] Radnai B., Gemeinder Y., Sauer B., Binder A., “Schädlicher Stromdurchgang (Harmful bearing currents)”, Part I, Research Report (in German), Report no. 1127, Forschungsvereinigung Antriebstechnik e.V., (FVA), Frankfurt am Main, Germany, 2015.

[2] Muetze A., “Bearing Currents in Inverter-Fed AC-Motors,” Ph.D. thesis, TU Darmstadt, Germany 2004.

[3] He F., Xie G., Luo J., “Electrical bearing failures in electric vehicles”. Friction journal, vol. 8, no. 1, pp. 4 – 28, 2020.

[4] Holm R., “Elektrische Kontakte (Electric Contacts Handbook)”, 3rd. Edition, Springer-Verlag, Berlin – Heidelberg, 1958.

[5] Braunovic M., Konchits V., Myshkin N., “Electrical Contacts – Fundamentals, applications and technology”, Boca Raton: CRC Press, Taylor & Francis Group, 2006.

[6] Slade P., “Electrical Contacts – Principles and Applications”, Boca Raton: CRC Press, Taylor & Francis Group, 2nd edition, 2014.

[7] Graf S., Sauer B., Safdarzadeh O., Weicker M., Binder A., “Model to estimate the thermal stress of the lubrication due to the mechanical and electrical loading in the rolling contact”, Research Report no. SA 898/25-1 & BI 701/20-1, Deutsche Forschungsgemeinschaft (DFG), Darmstadt, Germany, 2021.

[8] Safdarzadeh O., Weicker M., and Binder A., “Measuring of electrical currents, voltage and resistance of an axial bearing”, 2021 International Aegean Conference on Electrical Machines and Power Electronics (ACEMP) & 2021 International Conference on Optimization of Electrical and Electronic Equipment (OPTIM) IEEE, online, pp. 376-382, Sep. 2021.

[9] Franz W., “Dielektrischer Durchschlag (Dielectric breakdown)”, in Encyclopedia of Physics (Flügge S.), vol. 4/17, Springer-Verlag, Berlin – Heidelberg, pp. 155-263, 1956.

[10] Safdarzadeh, O., Weicker, M., Binder, A., “Steady-state Thermal analysis of the contact in bearings exposed to electrical currents”, 47th Conference of the IEEE Industrial Electronics Society, IECON, online, pp. 1-6, 2021.

[11] Andreason S., “Stromdurchgang durch Wälzlager (Passage of electric current through rolling bearings)”,

Die Kugellagerzeitschrift von SKF (Ball bearing journal from SKF), vol. 153, pp. 6-12, 1968.

[12] Carslaw H. S., Jaeger J. C., “Conduction of heat in solids”, Clarendon press, Oxford, no. 536.23, 2nd edition, 1959.

[13] Prashad H., “Effect of operating parameters on the threshold voltages and impedance response of non-insulated rolling element bearings under the action of electrical currents”, Wear journal, vol. 117, no. 2, pp. 223-240, 1987.

[14] Pittroff H., “Waelzlager im elektrischen Stromkreis”, Elektrische Bahnen, vol. 39, no. 3, pp. 54-61, 1968.

[15] Tran X.T., Vu T.D., Dang K.Q., “Numerical simulation of the heat treatment process for 100Cr6 steel”, Journal Acta Metallurgica Slovaca, vol. 23, no. 3, pp. 236-243, 2017.

[16] Francis P. H., "Thermo-mechanical effects in elastic wave propagation: a survey.", Journal of Sound and Vibration, vol. 21, no. 2, pp 181-192, 1972.

[17] Schwarzwälder M. C., "Non-Fourier Heat Conduction: The Maxwell-Cattaneo Equations.", Master of Science Thesis in Advanced Mathematics and Mathematical Engineering, Universitat Politècnica de Catalunya, Departament de Matemàtica Aplicada, 2015.

[18] Standard DIN EN ISO 683-17, “Heat-treated steels, alloy steels and free-cutting steels, Part 17: Ball and roller bearing steels”, 2015.